STUDY OF THE POLYMERIZATION DYNAMICS OF ASC AND ITS DOMAINS

by

Hulusi Onur KUZUCU

B.S., Molecular Biology and Genetics, Boğaziçi University, 2011

Submitted to the Institute for Graduate Studies in
Science and Engineering in partial fulfillment of
the requirements for the degree of
Master of Science

Graduate Program in Molecular Biology and Genetics
Boğaziçi University

2017

STUDY OF THE POLYMERIZATION DYNAMICS OF ASC AND ITS DOMAINS

APPROVED BY:

Prof. Nesrin ÖZÖREN (Thesis Supervisor)	.....
Assist. Prof. Nurhan ÖZLÜ	.....
Assist. Prof. Umut ŞAHİN	.....

DATE OF APPROVAL: 16.03.2017

ACKNOWLEDGEMENTS

I'd like to offer my gratitude to Prof. Nesrin Özören for having me as a graduate student and I appreciate the effort and patience she has put forward regarding my laboratory and thesis work. I would also like to thank Assist. Prof. Umut Şahin and Assist. Prof. Nurhan Özlü for sparing the time to evaluate this thesis.

I'd like to thank Prof. Amitav Sanyal for allowing me to use their spectrofluorometer, and I'd like to thank Prof. Türkan Haliloğlu and Assist. Prof. Hamdi Torun for allowing me to use their atomic force microscope. I'd additionally like to thank Fly Lab for allowing me to use their mounting medium, as well as Cancer Signaling Lab (CSL) and Molecular Toxicology and Cancer Research Lab (MTCRL) for allowing me to use their chemicals and facilities. Shout-out to all past and present Apoptosis and Cancer Immunology Lab (AKİL) members, including Aybüke Garipcan, M.Sc., Açelya Yılmazer, B.S., Mustafa Yalçınkaya, M.Sc., Elif Eren, Ph.D., Seda Yaşa, M.Sc., Ceren Saygı, M.Sc. and Mesut Berber, B.S.. They always offered their help and friendship when I asked for it.

This thesis wouldn't be possible without the priceless contributions of Yiğit Kocagöz, M.Sc., who offered his time to aid me in confocal microscopy, and Fidan Sümbül, Ph.D., who helped immensely in atomic force microscopy and data analysis.

Lastly, I'd like to thank my father, Prof. Ahmet Kuzucu, who has been extremely supportive regarding my work as well as my personal life. I have known no other person that went beyond duty and helped me when I needed it the most, and for that, I am, and will be, eternally grateful. I am glad to have come to this world as your son, and I dedicate this thesis to the support you've given me over the years.

This project was supported by Boğaziçi University Intramural Funds via Project BAP-TUG 8400.

What has been will be again, what
has been done will be done again;
there is nothing new under the sun.

Ecclesiastes 1:9

ABSTRACT

STUDY OF THE POLYMERIZATION DYNAMICS OF ASC AND ITS DOMAINS

Apoptosis-associated speck-like protein containing a CARD (ASC) is a 22 kDa protein composed of two conserved death-fold domains, PYD and CARD, that act as an adaptor protein in inflammasomes, multimolecular complexes that promote the maturation of pro-inflammatory cytokines IL-1β and IL-18. Death-fold domains are known to mediate the formation of higher order complexes through three distinct type of interactions. The importance of these interaction types are distinguished through ASC's ability to form a high molecular globular complex called the ASC speck. It has been shown that PYD-PYD and CARD-CARD homotypic interactions between ASC molecules is necessary to form this structure. Our group has reported the significance of homotypic PYD interactions, as well as of the residues on interaction surfaces. In this study, we have revisited the dynamics of homotypic PYD interactions by observing the formation of filamentous structures between mutant and wildtype variants. It was observed that PYD mutant variants previously known to disrupt homooligomerization such as E13A, K21A, K26A and D51A, were still able to contribute to multimeric structures along with their wildtype counterparts. Then, we have focused on the importance of homotypic CARD interactions, and investigated the significance of certain residues in CARD homooligomerization through Förster Resonance Energy Transfer (FRET) analysis. We have observed that the stability of interaction surfaces is more important in CARD, and mutant variants D134A, M159A and R160A showed a complete lack of filament formation. Lastly, we have selected wildtype CARD and CARD E130A mutant variant and done Single Molecule Force Spectroscopy (SMFS) to measure the physical strength of homotypic CARD interactions, and how disruption of interaction surfaces affect said strength.

ÖZET

ASC PROTEİNİ VE BÖLGELERİNİN POLİMERİZASYON DİNAMİKLERİNİN İNCELENMESİ

Apoptoz-ilişkili zerrecik-benzeri CARD içeren protein (ASC), 22 kDa büyüklüğünde, PYD ve CARD isimli korunulmuş iki ölüm bölgesi içeren bir proteindir. IL-1β ve IL-18 gibi enflamasyon destekleyici sitokinlerin salınımında aktif rol oynayan, enflamazom adı verilen çok moleküllü komplekste adaptör protein olarak görev alır. Ölüm bölgelerinin birbirinden farklı üç tip etkileşim ile yüksek mertebe komplekslerin oluşumuna ortam sağladığı bilinmektedir. Bu etkileşim tiplerinin önemi, ASC'ın "ASC zerresi" adı verilen, yüksek düzenli küresel bir yapı oluşturabilme yeteneğine bağlıdır. Bu yapıyı oluşturabilmesi için ASC molekülleri arasında PYD-PYD ve CARD-CARD homotipik etkileşimlere gerek olduğu çalışmalarla gösterilmiştir. Etkileşim yüzeylerindeki rezidüler yanında PYD'ler arası homotipik etkileşimlerin önemi araştırma grubumuz tarafından rapor edilmiştir. Bu çalışmada, ilk olarak, mutant ve vahşi tip PYD çeşitlerinin oluşturdukları filaman yapıları gözlemleyerek homotipik PYD etkileşimlerinin dinamiğini yeniden inceledik. Daha önceden oligomerizasyonu engellediği bilinen E13A, K21A, K26A ve D51A gibi PYD mutant çeşitlerinin, vahşi tip eşleriyle birlikte oligomerik yapıların oluşumunda katkıları olabildiğini gözlemledik. Sonra, homotipik CARD etkileşimlerinin önemi üzerine yoğunlaşarak Förster Rezonans Enerji Transferi (FRET) analizleri ile belirli rezidülerin CARD homooligomerizasyonundaki önemlerini inceledik. CARD oligomerizasyonunda etkileşim yüzeylerinin kararlı kalmasının daha önemli olduğunu, ve D134A, M159A ve R160A mutant CARD çeşitlerinin ikincil yapı oluşturamadıklarını gözlemledik. Son olarak, vahşi tip CARD ve CARD E130A mutant çeşidi üstünde Tek Molekül Kuvvet Spektroskopisi (SMFS) ile homotipik CARD etkileşimlerinin fiziksel kuvvetlerini ve etkileşim yüzeylerinin bozulmasının bu kuvveti nasıl etkilediğini ölçtük.

TABLE OF CONTENTS

LIST OF FIGURES

LIST OF TABLES

LIST OF SYMBOLS

A.U.	Arbitrary Units
B_n	Intensity of blank samples at n wavelength.
bp	Base Pairs
°C	Centigrade / Degree Celcius
g	Grams
G	Gravity
I_A	Intensity of acceptor fluorescence at acceptor excitation.
I_D	Intensity of donor fluorescence at donor excitation.
I_F	Intensity of acceptor fluorescence at donor excitation.
I_n	Intensity of sample at n wavelength.
IR_n	Intensity of sample at n wavelength, corrected for total protein.
kDa	Kilodaltons
L	Liters
m	Meters
M	Molars
min(s)	Minutes
ml	Milliliters
mm	Millimeters
mM	Millimolars
N	Newtons
N_{FRET}	Calculated FRET efficiency.
ng	Nanograms
nm	Nanometers
pH	Power of Hydrogen
pmoles	Picomoles
pN	Piconewtons
Q	Protein quantity of sample measured in $\mu g/ml$.
rpm	Revolutions per Minute

sec(s)	Seconds
V	Volts
α	Proportionality constant relating acceptor fluorescence at the acceptor excitation to the donor excitation.
β	Proportionality constant relating donor fluorescence at the acceptor emission to that detected at donor emission.
μg	Micrograms
μl	Microliters
μm	Micrometers

LIST OF ACRONYMS/ABBREVIATIONS

aa	Amino Acid(s)
Abs	Absolute
AFM	Atomic Force Microscopy
AIM2	Absent In Melanoma 2
ALR	AIM2-Like Receptors
ANOVA	ANalysis Of VAriance
apFRET	Acceptor Photobleaching FRET
APS	Ammonium PerSulfate
Ar	Argon
ASC	Apoptosis-associated Speck-like protein containing a CARD
ATP	Adenosine TriPhosphate
bb	Backbone
BCA	BiCinchoninic Acid
BSA	Bovine Serum Albumin
CARD	Caspase Activation and Recruitment Domain
CFP	Cyan Fluorescent Protein
DAMP	Danger-Associated Molecular Patterns
DD	Death Domain
ddH_2O	Double Distilled Water
DED	Death Effector Domain
DISC	Death-Inducing Signaling Complex
DMEM	Dulbecco's Modified Eagle Medium
DNA	DeoxyriboNucleic Acid
dsDNA	Double-Stranded DeoxyriboNucleic Acid
E.coli	*Escherichia coli*
EB	Elution Buffer
EDTA	EthyleneDiamineTetraacetic Acid
EF	Endotoxin Free

ECFP	Enhanced CFP
EGFP	Enhanced GFP
EtOH	Ethanol
EYFP	Enhanced YFP
FADD	Fas-Associated Death Domain protein
FBS	Fetal Bovine Serum
FP	Fluorescent Proteins
FRET E	FRET Efficiency
FRET	Förster Resonance Energy Transfer
GFP	Green Fluorescent Protein
HBS	HEPES Buffered Saline
HEK	Human Embryonic Kidney
HeNe	Helium Neon
HEPES	4-(2-HydroxyEthyl)-1-PiperazineEthaneSulfonic acid
HI	Heat Inactivated
HP	High Performance
IgG	ImmunoGlobulin G
IL	InterLeukin
IPTG	IsoPropyl β-D-1-ThioGalactopyranoside
LB	Lysogeny Broth
MEM NEAA	Minimum Essential Medium Non-Essential Amino Acids
MHC	Major Histocompatibility Complex
MWCO	Molecular Weight Cut-Off
NF-κB	Nuclear Factor Kappa-light-chain-enhancer of activated B cells
NLR	Nod-Like Receptors
NLRP3	NACHT, LRR and PYD domains-containing Protein 3
NMR	Nuclear Magnetic Resonance
NTA	NitriloTriacetic Acid
OD	Optical Density
OVA	OVAlbumin
PAGE	PolyAcrylamide Gel Electrophoresis

PAMP	Pathogen-Associated Molecular Patterns
PBS	Phosphate Buffered Saline
PCR	Polymerase Chain Reaction
PEG	PolyEthylene Glycol
Pen-Strep	Penicillin-Streptomycin
PIC	Protease Inhibitor Cocktail
PIDD	p53-Induced protein with a Death Domain
PRR	Pattern-Recognition Receptors
PYD	PYrin Domain
RAIDD	RIP-Associated ICH-1/CED-3 homologous protein with a Death Domain
RFP	Red Fluorescent Protein
RIG-I	Retinoic acid-Inducible Gene I
RIP	Receptor-Interacting Protein
RIPA	RadioImmunoPrecipitation Assay buffer
RLR	RIG-I-Like Receptors
RNA	RiboNucleic Acid
SDM	Site-Directed Mutagenesis
SDS	Sodium Dodecyl Sulfate
seFRET	Sensitized Emission FRET
SMFS	Single-Molecule Force Spectroscopy
SMOC	SupraMolecular Organizing Centers
TAE	Tris-Acetate-EDTA
TEMED	TEtraMethylEthyleneDiamine
TLR	Toll-Like Receptors
UV	UltraViolet
YFP	Yellow Fluorescent Protein
wt	Wildtype

1. INTRODUCTION

1.1. Immune System

The immune system consists of a vast network of cellular and sub-cellular processes that create a defense mechanism against potentially pathogenic microorganisms that are introduced to the human body. The immune system is divided into two parts depending on the type and speed of the reaction. [7] Innate immunity consists of physical, chemical and microbiological barriers, as well as elements of the immune system - including neutrophils, monocytes, macrophages, complement system and cytokines - that make up the first defense line against pathogens, providing immediate host defense. [8] Adaptive immunity consists of antigen-specific reactions through T and B lymphocytes that provide a slower but highly specific immune response, which is additionally stored in memory cells for faster response in subsequent pathogen exposure. [9]

1.1.1. Innate Immunity

Immune cells associated with innate immune responses naturally reside within many tissues, and more immune cells migrate to the stimuli region in response to invading organisms or tissue damage. [10] Initiation and regulation of innate immune responses are done mainly through the sensing of pathogen-associated molecular patterns (PAMPs) - that are common to many types of bacteria, fungi and/or viruses, like lipopolysaccharides, lipotechoic acid, mannans - or danger-associated molecular patterns (DAMPs) - formed or released by host cells under stress, homeostasis disruption or metabolic imbalance - by germline-encoded pattern-recognition receptors (PRRs) in myeloid cells. In addition, PRRs also recognize host-derived molecules that are only present when host cells have died or are injured. PRRs consist of Toll-like receptors (TLRs), RIG-I-like receptors (RLRs), Nod-like receptors (NLRs), AIM2-like receptors (ALRs), C-type lectin receptors (CLRs) and other DNA sensors. [11] Activation of PRRs initiate signaling cascades that result in pro-inflammatory gene expression, as well as proteolytical activation of inflammatory caspases. [1]

1.1.2. Nod-Like Receptors

Among these PRRs, NLRs maintain a large protein family of intracellular sensors sharing a conserved central nucleotide-binding oligomerization domain (NOD or NACHT), a C-terminal leucine-rich repeat (LRR) region, and a variable N-terminal effector domain. [12] NLRs contain receptor, regulator and adaptor proteins depending on their functions. The effector domain may consist of a pyrin domain (PYD), a caspase recruitment domain (CARD) or a baculovirus inhibitor of apoptosis protein repeat (BIR) domain. NLR receptors Nod1 and Nod2 have been shown to sense PAMPs and activate NF-κB signaling, while several NLRP (NLR subfamily with N-terminal PYD) proteins form an inflammasome upon stimulation with respective activators, regulating IL-1β and IL-18 secretion. [13]

1.2. Inflammasome

Supramolecular organizing centers (SMOCs) are large, heterogeneous assemblies that form in many immune signaling pathways as part of signal transduction or amplification. Inflammasomes are multimolecular complexes that promote the cleavage of pro-caspase-1 and the maturation of pro-inflammatory cytokines IL-1β and IL-18. Canonical inflammasomes consist of three classes of molecules: sensors in the ALR and NLR family, adapters such as ASC, and effectors such as caspase-1. [14]

1.2.1. Inflammasome Structure and Formation

In the resting state, sensor molecules appear to exist in autoinhibited conformations. Upon encountering PAMPs and DAMPs - such as flagellin, lipoproteins, viral dsDNA, extracellular ATP etc. - sensor molecules undergo conformational changes that overcome the autoinhibition. Sensor proteins with a PYD such as AIM2 and NLRP3 cluster to form a base for ASC recruitment. [14] Recruited ASC is induced to form long filaments through oligomerization with other ASC proteins via homotypic interactions of the PYD domain. Pro-caspase-1 contains a CARD that functions as a pro-domain, and allows for the recruitment of pro-caspase-1 to the ASC filament, as

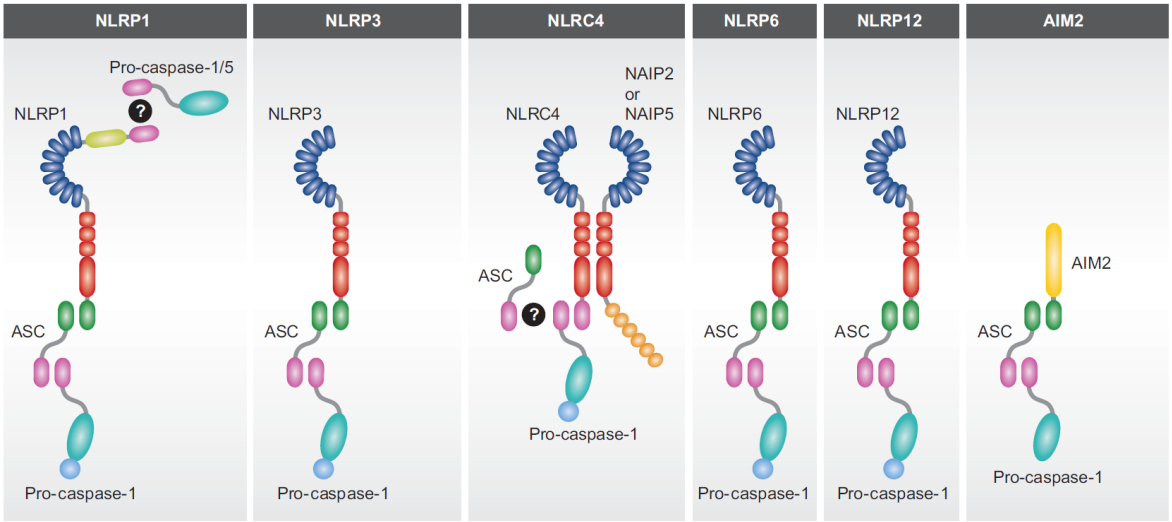

Figure 1.1. Assembled inflammasomes. ASC always acts as the adaptor between the sensor and the effector molecules. (Adopted from Bauernfeind, 2013.) [1]

well as oligomerization of pro-caspase-1 with other pro-caspase-1 molecules. Several units of pro-caspase-1 can be recruited to the ASC structure and auto-catalyze their cleavage. Active caspase-1 cleaves pro-IL-1β and pro-IL-18, and induces the release of their mature forms. [4]

1.3. Death-Fold Superfamily

Signal transduction pathways in immunity, inflammation and cell death depend on proteins containing homotypic interaction motifs called death domains (DD) belonging to the death-fold superfamily. CARDs and PYDs are two of the subfamilies of this superfamily. Despite divergence in sequence among its members, this superfamily is known by its globular structure wherein six amphipathic α-helices are arranged in an antiparallel α-helical bundle. Structural differences between individual domains are result of alterations in length and orientation of the α-helices, as well as the distribution of charged and hydrophobic residues along the surface. [2]

1.3.1. Multimeric Formations of Molecules Including a Death Domain

Most members of the death-fold superfamily propagate cell death signals via the formation of multimeric compounds. Fas-associated death domain protein (FADD) is an adaptor protein in death receptor-induced apoptosis pathway, initiated by the death-inducing signaling complex (DISC). FADD is recruited to DISC through direct interactions of the death domains present on both proteins, exposing the FADD death effector domain (DED). Exposed DED promotes recruitment of DED-only proteins including pro-caspase-8, and once recruited, starts creating a DED chain-based pro-caspase-8 activation platform via interaction of tandem DEDs. [15]

Another protein, p53-induced protein with a death domain (PIDD) is known to be a binding partner of receptor-interacting protein-associated ICH-1/CED-3 homologous protein with a death domain (RAIDD). Upon activation, PIDD recruits both RAIDD and caspase-2, forming a large complex called the PIDDosome. Crystal structure of the PIDDosome reveals a core ring of five PIDD-DD on top of a ring of seven RAIDD-DD. Disruption of this oligomeric compound results in defective caspase-2 processing. [16] Combined with the structural properties of the inflammasome, it can be said that death domains are capable of forming multimeric compounds, through which the cell response propagates.

1.3.2. Molecular Interactions In Death-Fold Superfamily Members

The ability of death-fold domains to mediate the formation of higher order complexes resides in their ability to engage in three distinct types of interactions. A type I interaction is formed when residues from helices 1 and 4 (patch Ia) of one domain interact with residues from helices 2 and 3 (patch Ib) of another. A type II interaction is formed when residues from helix 4 and the loop between helices 4 and 5 (patch IIa) of one domain interact with residues of the loop between helices 5 and 6 (patch IIb) of another. A type III interaction is formed when residues from helix 3 (patch IIIa) of one death-fold domain interact with residues located on the loops between helices 1 and 2 (patch IIIa) and between helices 3 and 4 (patch IIIb). Because these six interaction

patches do not overlap, each domain can potentially engage up to six binding partners by using each of the three types of pairwise interactions twice. While the three interaction types are conserved in the death-fold superfamily, there are differences between death domains in utilization of non-covalent binding modes as well as in surface complementarity. [2]

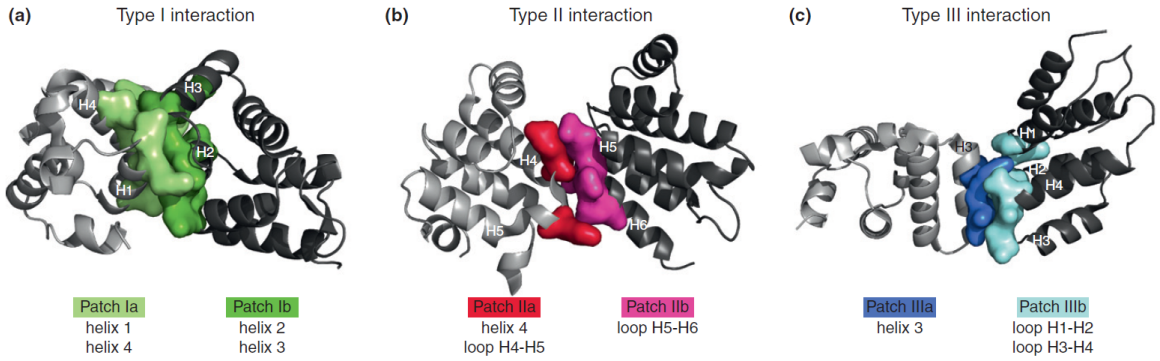

Figure 1.2. A death domain mediates three interaction types through six interaction patches. The three asymmetric interaction types - (a) type I, (b) type II and (c) type III - shown here are between the DDs of RAIDD (light gray) and PIDD (dark gray). (Adopted from Kersse, 2011.) [2]

1.4. Apoptosis-Associates Speck-Like Protein Containing a CARD

Apoptosis-associated speck-like protein containing a CARD (ASC) is a 22kDa protein composed of 195 amino acids that primarily function as an adaptor protein during inflammasome assembly. [4] ASC is composed of two conserved death-fold domains; PYD and CARD, connected by a 23 aa unstructured and flexible linker. [17] Both domains function to promote homotypic interactions. ASC is soluble as a monomer at low pH, in solution with chaotropic agents, and at physiological potassium concentrations, but forms long and well-defined fibrils at higher pH or lower potassium concentrations. [18]

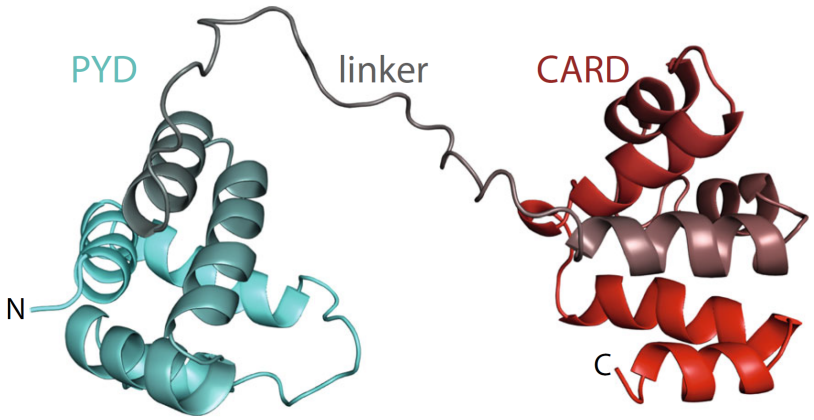

Figure 1.3. Cartoon diagram of ASC (PDB ID: 2KN6 [3]) showing the PYD, the flexible linker, and the CARD. (Adopted from Hoss, 2016.) [4]

In non-activated cells, ASC is found in its soluble form, as a high thermodynamic energy barrier prevents spontaneous oligomerization, however, inflammasome sensors are capable of forming an oligomeric PYD cluster, which acts as a base for ASC molecules to form a helical filament upon. This PYD base, allowing PYD self-interaction, is thought to lower the high energy barrier of ASC oligomerization, and causes unlimited polymerization by prion-like propagation. [19]

1.4.1. ASC Structure and Kinetics

ASC-PYD is highly polar, containing positive charges in the helices 2 and 3, as well as in the loop connecting these helices, and negative charges in helices 1 and 4. [20] These complementary charges form type I interface of ASC-PYD, and are thought to be the driving force in filament assembly, as studies on ASC filament showed that one side is positively charged while the opposite side is negatively charged. Type I interface is additionally the most conserved interface with the largest surface area. Type II interface has the second largest surface area with Type III interface having the smallest. Regardless, all types of interaction are crucial for stabilization during filament formation. Type III interface of ASC-PYD differs from the death-fold superfamily by being between the loop between helices 2 and 3 (forming patch IIIb) and the loop

between helices 1 and 2 (forming patch IIIa). When transformed from the monomeric to the filamentous state, ASC-PYD molecules retain their secondary structure and the position of all six helices, however, a minimal conformational change in the region of the variable loop between helices 2 and 3 occurs. [21] This variable loop is involved in all three interfaces, which might explain this conformational change. [4]

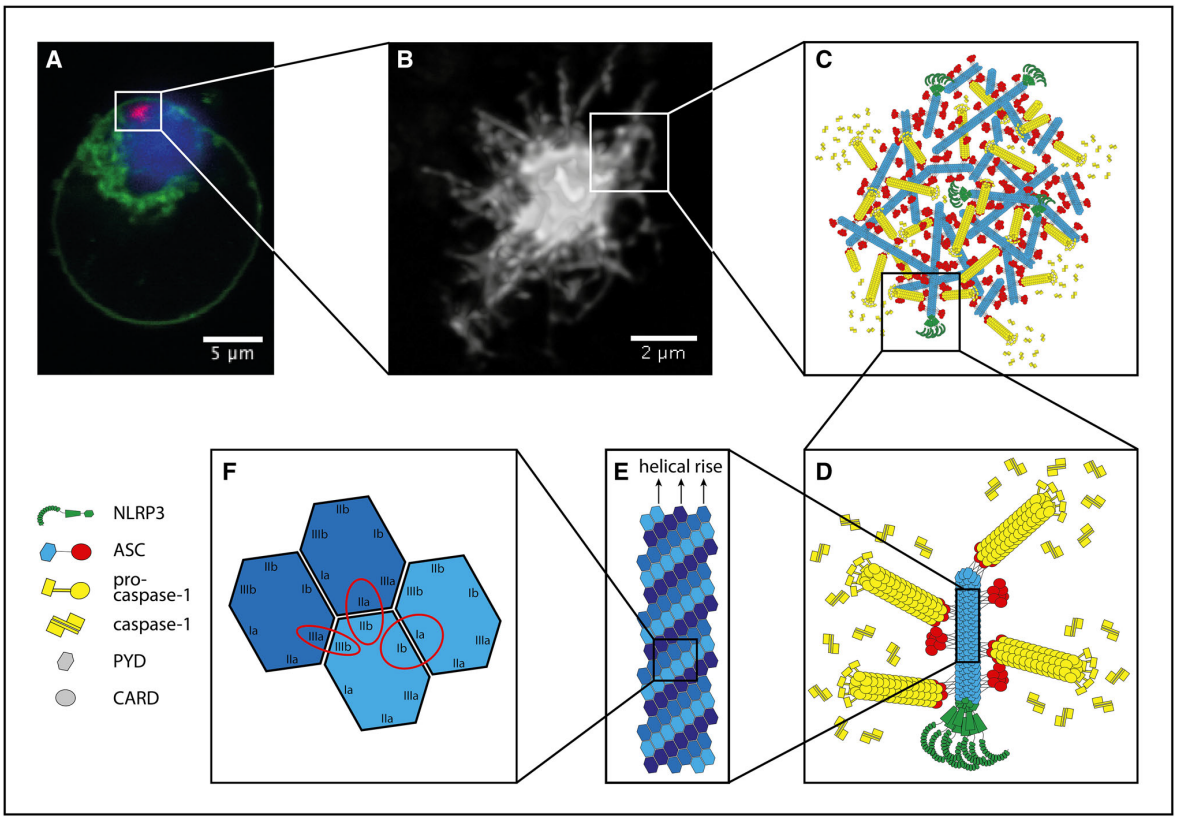

Figure 1.4. ASC speck structure at different levels of complexity. (Adopted from Hoss, 2016.) [4]

1.4.2. The ASC Speck

The ASC speck is composed of multiple filamentous structures clustered together to build up a high molecular globular complex. [22] The ASC filaments are cross-linked via CARD-CARD interactions. Homotypic ASC-CARD interactions can form bases to facilitate the formation of filaments by pro-caspase-1-CARD. [23] ASC-CARD is partially unfolded [18], preventing ASC filaments from being too densely cross-linked via CARD-CARD interactions, leaving enough free CARDs to interact with pro-caspase-

1. [4] Different levels of complexity of the ASC speck structure can be seen in Figure 1.4. In this figure, the labeled parts are as follows: (A) Confocal microscopy of an ASC speck assembled from ASC-mCherry. (B) High-resolution emission depletion image of an ASC speck. (C, D) Schematic view of an ASC speck based on the NLRP3 inflammasome. NLRP3-PYD forms a base for ASC-PYD to polymerize on and create long fibrils that are cross-linked through ASC-CARD clusters. These clusters also form a base for pro-caspase-1-CARD polymeric fibrils, and the close proximity of several caspases leads to self-cleavage into mature caspase-1. (E) Schematic view of the ASC-PYD helix, indicating the direction of polymerization as well as the three strands. (F) Schematic representation of the three interfaces that mediate ASC-PYD interactions. [4]

The process of ASC speck assembly was described to take no longer than 100 s in HeLa and THP-1 cells expressing fluorescently labeled ASC. [24] As soon as the PYDs of inflammasome sensors are clustered and form a base for filamentous polymerization of ASC, the reaction is irreversible, no longer dependent on the original initiating signal, and follows an energetic gradient until all the ASC molecules of an activated cell are recruited. [19] Consequently, cells are either activated and contain a speck, or they are inactive and ASC is in soluble form. [4]

1.4.3. Artificial Loading of ASC Specks with Cytosolic Antigens

After the ASC speck forms, cells may undergo caspase-1 dependent cell death (called pyroptosis), causing cytosolic content to leak into the extracellular environment. It's been observed that released ASC specks can be engulfed by THP-1 cells. After engulfment, tubular vesicles pinching off from the phagolysosome containing the ASC speck were also observed. These tubular vesicles are considered as responsible for MHC-II dependent presentation of extracellular antigens. Additionally, the gradual degradation of the engulfed ASC speck is similar to controlled release applications of many antigen delivery vehicles. [25] Recently it was investigated whether ASC could be used as an antigen carrying system, and experimentation with ASC fused with H5 or OVA proteins showed increase in antigen specific IgG after introduction of H5-ASC or OVA-ASC to mice. [26] This feature of ASC is currently being studied.

1.5. Förster Resonance Energy Transfer

Förster (or Fluorescence) Resonance Energy Transfer (FRET) is a phenomenon in which an excited donor fluorophore, instead of releasing energy via emission, transfers its excitation energy to an acceptor fluorophore, causing the acceptor to fluoresce. [27] This short range (1-10nm) dipole-dipole interaction between fluorophores has been used as a tool to monitor biochemical activities that cause change in molecular proximity, such as protein-protein interactions, conformational changes, enzymatic activities etc. [28]

FRET occurs between two close fluorophores with substantial overlap between the donor's emission and acceptor's absorption spectra [29], and is calculated in terms of efficiency (FRET E); the percent of energy transfer from the donor to acceptor at a given state. There are many ways of calculating FRET E, depending on the fluorescence characteristic that is being measured. This study focuses on two of the most widely used methods to calculate FRET E through fluorescence intensity: acceptor photobleaching FRET (apFRET) and sensitized emission FRET (seFRET).

1.5.1. Acceptor Photobleaching FRET

apFRET is dependent on the energy transfer from the donor to acceptor FP that quenches donor emission. [30] As the acceptor is photobleached, energy transfer cannot occur, thus the donor is de-quenched and results in a higher donor fluorescence intensity. This method is widely used in calculating FRET E, and is a straightforward method to measure FRET E without the need of reference measurements, and it is most applicable to fixed cells or tissues, however, it is an irreversible endpoint assay, as photobleaching destroys the acceptor biosensor signal and prevents multiple sampling from the same set of sensors. apFRET works under two assumptions; that photobleaching of the acceptor destroys both emission and absorption, and that the molar ratios of donor to acceptor FP is ≤ 1. Thus, it is best suited to FPs that do not have dark / weakly bright states after photobleaching (like red FPs / YFP) and to intramolecular biosensors. [5]

1.5.2. Sensitized Emission FRET

seFRET is a more practical method to measure FRET changes as it's faster and easier to use. One of the methods used to measure seFRET is called N_{FRET}, which calculates the FRET change from intensities of donor emission at donor excitation, acceptor emission at acceptor excitation and acceptor emission at donor excitation. [5] The calculation is corrected for the FRET signals and expression levels of donor and acceptor, which makes N_{FRET} to be especially useful in intermolecular biosensors; where the molar ratios of FPs are unknown. [31]

1.5.3. FRET Biosensors

FRET-based biosensors are classified into two categories: intramolecular type, where donor and acceptor fluorophores are present on the same molecule and conformational changes in the molecule cause FRET, and intermolecular type, where donor and acceptor fluorophores are fused to different molecules, and FRET occurs when these molecules come into close proximity. [28] The most commonly used type of fluorophore in FRET biosensors are fluorescent proteins (FPs). Easy introduction of FPs into molecules via genetic engineering, high cellular specificity via the use of tissue-specific promoters, quick introduction into cells in vitro or in vivo through transfection or infection, and long-term stability in living cells are a few of the reasons why FPs are preferred above other fluorophores like small organic dyes or quantum dots. [5]

There are many FP pairs used in FRET experiments. The most commonly used are the CFP-YFP pairs (starting with ECFP-EYFP), with engineered CFPs having the highest quantum yield amongst all FPs, as well as YFP derivatives that are less sensitive to environmental conditions like pH or chloride, and are more photostable. However, CFP-YFP pairs suffer from several problems, such as fast photobleaching of YFPs, spectral cross-talk, phototoxicity and others that are problematic for FRET. [32] GFP-RFP pairs overcome these disadvantages of CFP-YFP pairs by inducing less autofluorescence, less phototoxicity and greater spectra separation. Unfortunately, RFPs show low brightness, and in pairs such as the EGFP-mCherry FP pair, the FRET

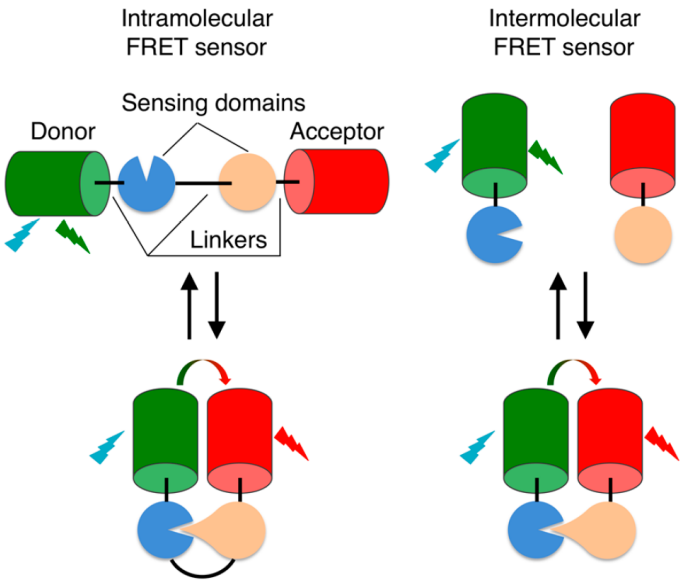

Figure 1.5. Schematic view of intramolecular and intermolecular FRET sensors. Conformational changes in the sensing domains (left) or inter-domain interactions (right) lead to change in FRET activity. (Adopted from Bajar, 2016. [5])

emission may be too weak to differentiate from the donor emission, preventing the use of this pair in ratiometric imaging. [5] Nevertheless, brighter and more photostable GFP-RFP variants have been developed, exhibiting improved dynamic range compared to CFP-YFP pairs and improved FRET E compared to EGFP-mCherry. [32]

1.6. Atomic Force Microscopy

Atomic force microscopy is a primarily scanning probe microscopy method [33], created to overcome limitations of an older method called scanning tunneling microscopy. [34] Atomic force microscope consists of components including a piezoelectric scanner, a flexible cantilever containing a sharp probe, a laser source, a photodiode detector and feedback electronics. Movements of the flexible cantilever are monitored by changes in laser deflection off of a reflective surface on the top of the cantilever. These changes are captured by the photodiode detector. Depending on the system, the piezoelectric scanner, which can move in three dimensional space by applying voltage to the piezoelectric material, can be attached to the cantilever holder or to the sample

holder, while the other stays stationary. This set-up allows for both high-resolution imaging and probing molecular interactions of samples. Samples should be prepared suitably and immobilized on a solid surface for the specific AFM application. [6]

1.6.1. Applications of Atomic Force Microscopy

AFM has many applications, with imaging and single-molecule force spectroscopy being the most common. In AFM imaging, the AFM probe is raster-scanned (row by row scanning) over the surface of a biological sample to generate a topographical image. This scanning process is done by either contact mode [33], where the AFM probe remains in constant contact with the sample surface and the deflection of the cantilever is monitored, or tapping mode [35], where the cantilever is oscillated to only touch the sample, and the amplitude of the cantilever's oscillation is monitored as it changes when the sample's height changes. The tapping mode is preferred when the sample is prone to be damaged or deformed by the forces applied in contact mode. [6] Overall, a high signal-to-noise ratio is achievable with AFM, allowing for high-resolution imaging of single molecules. [36]

1.6.2. Single-Molecule Force Spectroscopy

For probing single ligand-protein interactions, AFM can be used to perform single-molecule force spectroscopy (SMFS) [37]; the probe is used to break chemical bonds formed in molecules by applying force through the flexed cantilever. Functionalization of the AFM probe allows it to be used as bait in probing protein-ligand interactions. When the functionalized AFM probe is brought into contact with the sample surface, the ligand attached to the probe is able to bind to its partner on the surface. As the probe is pulled away from the surface, the chemical bonds stabilizing the protein-ligand pair are stretched until sufficient force is applied to overcome this interaction. This applied force is determined from the magnitude of the cantilever's flex, and the cantilever's spring constant. The process of rupturing bonds is recorded in force-distance curves, where a single peak represents a rupture event and the peak height indicates the magnitude of force required for rupture. [6] The rupture force of chemical bonds is also

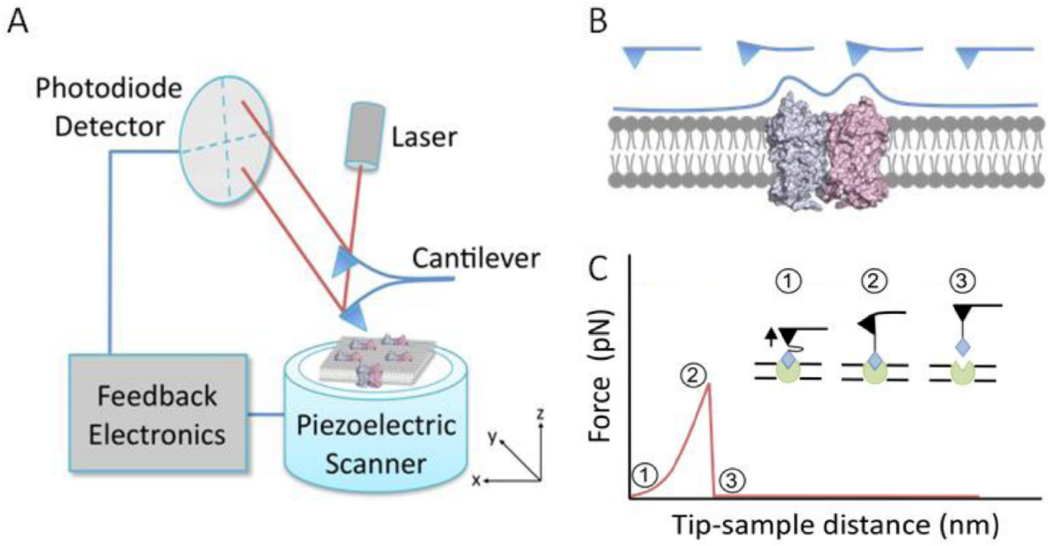

Figure 1.6. AFM overview. (A) Components of an atomic force microscope. (B) Contact mode imaging. (C) Probing single protein-ligand interactions by force spectroscopy. A force-distance curve is recorded, and the different parts of the curve corresponds to the numbered events shown. (Adopted from Whited, 2014. [6])

dependent on the loading rate - the velocity of the cantilever during rapture. [38] This dependence provides mechanistic insights into protein-ligand interactions, and SMFS conducted at different retraction velocities is often referred to as dynamic SMFS. [6]

SMFS can also be used to unfold membrane proteins and probe the molecular interactions required to stabilize protein structure. [39] In mechanical unfolding experiments, the probe is pressed into the sample to form chemical bonds with the terminal region of the membrane protein. As the probe is retracted, the protein is stretched and begins to unfold. The unfolding events are recorded in force-distance curves, where each peak represents the unfolding of a distinct region of the protein that has stability to resist unfolding. [6]

2. PURPOSE

Inflammasomes, pyroptosomes, PIDDosomes and an increasing list of multimeric supramolecular complexes have become the focus of inflammation signaling, cell death signaling and even cell survival signaling pathways. Our group has pioneered a study on the molecular assembly dynamics of pyroptosome / ASC speck structures [17]. We have previously characterized a set of residues in PYD & CARD domains and have been able to show the importance of the three types of interaction for the PYD domain. In this thesis, we aimed to study the importance of the homotypic interactions of the CARD domain and we aimed to observe effects of single amino acid mutations that are designed to disrupt the interaction surfaces of CARD. Furthermore, we aimed to measure the physical strength of interactions taking role in CARD oligomerization by using AFM. To these ends we undertook a three step approach:

The first step was to evaluate whether FRET was an applicable method on measuring homotypic protein interactions between CARD and PYD variants. For this purpose, multiple methods for FRET observation have been tested on different sets of fluorescently labeled fusion proteins.

The second step was to observe the behavior of homotypic PYD-PYD and CARD-CARD interactions. For this purpose, we have expressed mutant and wildtype variants of both domains, and measured the FRET efficiency between them.

The final step was to measure the interaction strengths of homotypic PYD-PYD and CARD-CARD interactions, as well as observing the difference - if there's any - in the binding strengths of mutant and wildtype variants. For this purpose, we have evaluated whether AFM was applicable in measuring said interactions, made His-tagged wildtype and mutant CARD variants, and used said variants in SMFS.

3. MATERIALS

3.1. Cell Lines

Table 3.1. Cell lines used in this study.

	Catalog Number	Main Source	Provider
HEK293(F)T	R700-07	Invitrogen, USA	Kindly provided by Prof. Maria Soengas

3.2. Chemicals, Plastics and Glassware

Chemicals used in this study were purchased from either Sigma-Aldrich (Germany) or Merck (Germany). Cell culture dishes and serological pipettes were purchased from VWR (USA). Microcentrifuge tubes and micropipette tips were purchased from Axygen (Corning, USA). All glassware, tips and tubes were sterilized prior to use by autoclaving at 121°C for 20 minutes.

3.3. Buffers and Solutions

3.3.1. Cell Culture

FBS was thawed at 4°C followed by heat inactivation at 56°C for 60 minutes before aliquoting to 50 ml falcon tubes. This is done to disable complement system proteins in the serum. Before use, complete DMEM was heated to 37°C via a water bath. All cell culture steps were done inside a laminar flow cabinet, sterilized via UV irradiation.

Table 3.2. Solutions and buffers used in cell culture.

Dulbecco's Modified Eagle Medium (41966-029) MEM Non-Essential Amino Acids (11140-050) Penicillin Streptomycin (Pen-Strep) (15140-122) Fetal Bovine Serum (10270-106)	Gibco, Thermo Fisher Scientific, USA
Complete DMEM	500 ml DMEM 50 ml FBS-HI 5.5 ml Pen-Strep 5.5 ml MEM NEAA
10x PBS (pH 7.4) (Diluted to 1L and filter-sterilized before use)	80 g NaCl 2 g KCl 2.4 g KH_2PO_4 14.4 g Na_2HPO_4 1 L ddH_2O
0.05% Trypsin (pH 8.0) (Filter-sterilized and aliquoted to 50 ml falcon tubes prior to use)	0.154 g EDTA 0.5 g Trypsin 8 g NaCl 0.4 g KCl 0.06 g KH_2PO_4 1 g Glucose 0.048 g Na_2HPO_4 0.35 g $NaHCO_3$ 1 L ddH_2O
VectaShield Mounting Medium H-1000	Vector Laboratories, UK

3.3.2. Calcium Phosphate Transfection

Table 3.3. Solutions used in calcium phosphate transfection. All solutions were filter-sterilized using a 0.22 μm filter prior to use.

2x HBS Buffer (pH 7.0)	50 mM HEPES 280 mM NaCl 1.5 mM Na_2HPO_4
10 mM Chloroquine	0.051 g Chloroquine Diphosphate 10 ml ddH_2O
2 M $CaCl_2$	2,22 g $CaCl_2$ 10 ml ddH_2O

3.3.3. Cloning and Analytical Digestion

Table 3.4. Enzymes and reagents used for cloning and PCR applications.

Restriction Enzymes (BglII, DpnI, EcoRI) T4 DNA Ligase Q5 High-Fidelity 2x Master Mix	New England Biolabs, USA
PCR MasterMix 5x	Gene and Cell Technologies, USA

3.3.4. Agarose Gel Electrophoresis

Table 3.5. Buffers and reagents used for agarose gel electrophoresis.

50x Tris-Acetate-EDTA (TAE) Buffer	242 g Tris-base 57.1 ml Acetate (Abs. Acetic Acid) 14.62 g EDTA 942.9 ml ddH_2O
GreenView Plus DNA Gel Stain	Applied BioProbes, USA
Gel Loading Dye Purple (6x)	New England Biolabs, USA
SYBR Green I Nucleic Acid Gel Stain	Roche, Switzerland
GeneRuler 100 bp Plus DNA Ladder	Thermo Fisher Scientific, USA

3.3.5. Bacterial Culture

Table 3.6. Solutions used in bacterial culture. Liquid and solid culture solutions were autoclaved at 121°C for 15 minutes prior to use. Antibiotics are filter-sterilized using a 0.22 μm filter and stored in aliquots at -20°C.

LB Agar Solid Culture (per 1 L ddH_2O)	15 g Agar 5 g NaCl 10 g Tryptone 5 g Yeast Extract
LB Medium Liquid Culture (per 1 L ddH_2O)	5 g NaCl 10 g Tryptone 5 g Yeast Extract
Kanamycin (1000x)	0.5 g Kanamycin Sulfate 10 ml ddH_2O
Chloramphenicol (1000x)	0.34 g Chloramphenicol 10 ml Ethanol (Abs.)

3.3.6. SDS-PAGE

Table 3.7. Solutions used in SDS-PAGE.

30% Acrylamide	30 g acrylamide 0.8 g bisacrylamide 100 ml ddH_2O
15% Resolving Gel Stock	50 ml 30% Acrylamide 1 ml 10% SDS 20 ml 1.875 M Tris pH 8.8 29 ml ddH_2O
4% Stacking Gel Stock	3.3 ml 30% Acrylamide 250 μl 10% SDS 6.3 ml 0.5 M Tris pH 6.8 15 ml ddH_2O

Table 3.7. Solutions used in SDS-PAGE (cont.).

15% Resolving Gel (for 1.5 mm gel thickness)	8 ml Resolving Gel Stock 80 μl 10% APS 8 μl TEMED
4% Stacking Gel (for 1.5 mm gel thickness)	4 ml Stacking Gel Stock 40 μl 10% APS 4 μl TEMED
10x Running Buffer (Diluted to 1x prior to use)	10 g SDS 30.3 g Tris Base 144.1 g Glycine 1 L ddH_2O
Laemmli Sample Buffer (5x)	500 μl 1.25 M Tris-HCl (pH 6.8) 5.9 ml Glycerol 500 μl 1% Bromophenol Blue 0.5 g SDS 500 μl β-Mercaptoethanol 2.6 ml ddH_2O
Coomassie G-250 Stain	0.2 g Coomassie Brilliant Blue G-250 25 g Aluminum Potassium Sulfate Dodecahydrate 50 ml Ethanol (Abs.) 11.75 ml Orthophosphoric Acid (85%) 438.25 ml ddH_2O
PageRuler Prestained Protein Ladder	Thermo Fisher Scientific, USA

3.4. Kits

Table 3.8. Kits used in this study.

NucleoBond® Xtra Midi EF NucleoSpin® Plasmid NucleoSpin® Gel and PCR Clean-up	Macherey-Nagel, Germany
HisTrap™ HP Column	GE Healthcare, UK
Pierce™ BCA Protein Assay Kit Pierce™ Coomassie Plus Assay Kit	Thermo Fisher Scientific, USA

3.5. Equipment

Table 3.9. Equipment used in this study.

Agarose Imaging	Mini LED Transilluminator, IO Rodeo, USA
Atomic Force Microscope	Dimension Edge, Bruker, USA
Autoclaves	AMA260BT, Astell Scientific, UK ASB270N, Astell Scientific, UK
Centrifuges	Allegra X-22R, Beckman Coulter, USA himac CT15E, Hitachi Koki, Japan J2-21, Beckman Coulter, USA MiniStar, VWR, USA
Data Acquisition and Control	PXI-based System, National Instruments, USA
Dialysis Tubing	Spectra/Por 7®132103, Spectrum Labs, USA
Electronic Scales	BJ 4100D, Precisa, Switzerland XT 4200C, Precisa, Switzerland
Freezers	UFR370 SD, Uğur, Turkey 2020 ND, Arçelik, Turkey TS 368, Thermo Fisher Scientific, USA
Incubator	Forma Series II 3111, Thermo Fisher Scientific, USA
Heat Block	myBlock Mini, Benchmark Scientific, USA

Table 3.9. Equipment used in this study. (cont.)

Horizontal Electrophoresis	Mini gel electrophoresis kit, IO Rodeo, USA MP-1015, IBI Scientific, USA
Laminar Flow Cabinet	Class II A, Tezsan, Turkey
Magnetic Stirrer	Topolino, IKA, Germany
Microscopes	Eclipse TS100, Nikon Corporation, Japan TCS SP5 II, Leica Microsystems, Germany
Microwave Oven	MD-555 S, Arçelik, Turkey
Oscilloscope	TBS1000B, Tektronix, USA
Peristaltic Pump	LabN1, Baoding Shenchen, China
pH Meter	pH2700, Oakton Instruments, USA
Pipettes	Acura 826 Electro Series, Socorex, Switzerland Axygen Axypet Series, Corning, USA Finnpipette F2, Thermo Fisher Scientific, USA Accurpette, VWR, USA
Refrigerators	USS 374 DTKY, Uğur, Turkey S1150A, Vestel, Turkey
Power Supplies	Electrophoresis PSU Kit, IO Rodeo, USA PowerPac Basic, Bio Rad, USA
Thermal Cyclers	C1000, Bio Rad, USA OpenPCR, Chai Biotechnologies, USA
Thermal Shakers	Forma 420, Thermo Fisher Scientific, USA CTS-1, Inovia Teknoloji, Turkey
Shakers	PSU-10i, Grant, UK
Spectrofluorometer	Cary Eclipse, Agilent Technologies, USA
Spectrophotometer	NanoDrop ND-100, Thermo Fisher Scientific, USA
Vortex Shaker	Vortexer, Heathrow Scientific, USA
Vertical Electrophoresis	Mini PROTEAN Tetracell, Bio-Rad, USA
Water Baths	1002, GFL, Germany WB 14, Memmert, Germany

3.5.1. Plasmids

Table 3.10. Plasmids used in this study.

pcDNA3-hASC	Nuñez Lab, University of Michigan, USA
pET30a-hASC	AKİL, Boğaziçi University, Turkey
pEGFP-C3	AKİL, Boğaziçi University, Turkey
pEGFP-C3-PYD	AKİL, Boğaziçi University, Turkey
pEGFP-C3-PYD-E13A	AKİL, Boğaziçi University, Turkey
pEGFP-C3-PYD-E19A	AKİL, Boğaziçi University, Turkey
pEGFP-C3-PYD-K21A	AKİL, Boğaziçi University, Turkey
pEGFP-C3-PYD-L25A	AKİL, Boğaziçi University, Turkey
pEGFP-C3-PYD-K26A	AKİL, Boğaziçi University, Turkey
pEGFP-C3-PYD-D51A	AKİL, Boğaziçi University, Turkey
pEGFP-C3-PYD-L68A	AKİL, Boğaziçi University, Turkey
pEGFP-C3-PYD-L73A	AKİL, Boğaziçi University, Turkey
pEGFP-C3-CARD	AKİL, Boğaziçi University, Turkey
pmCherry-C3-PYD	AKİL, Boğaziçi University, Turkey
pmCherry-C3-CARD	AKİL, Boğaziçi University, Turkey

Table 3.11. Plasmids cloned for this study.

pEGFP-C3-PYD-S29A	pEGFP-C3-CARD-E130A
pEGFP-C3-PYD-T53A	pEGFP-C3-CARD-D134A
pEGFP-C3-PYD-Y60A	pEGFP-C3-CARD-L141A
pEGFP-C3-PYD-L85A	pEGFP-C3-CARD-Y146A
	pEGFP-C3-CARD-P156A
pET30a-CARD	pEGFP-C3-CARD-M159A
pET30a-CARD-E130A	pEGFP-C3-CARD-R160A

3.5.2. Primers

Table 3.12. Primers used in this study.

Primer Name	**Sequence**
P2P-CARD F	AATTTAGATCTAGGCCTGCACTTTATAGAC
P2P-CARD R	TTATAGAATTCTCAGCTCCGCTCCAG
R160A FWD	CCACCAACCCAAGCAAGATGGCGAAGCTCTTCAG TTTCAC
R160A REV	GTGAAACTGAAGAGCTTCGCCATCTTGCTTGGGT TGGTGG
M159A FWD	CCACCAACCCAAGCAAGGCGCGGAAGCTCTTCAG
M159A REV	CTGAAGAGCTTCCGCGCCTTGCTTGGGTTGGTGG
P156A FWD	GCCGAGCCCACCAACGCAAGCAAGATGCGGAAG
P156A REV	CTTCCGCATCTTGCTTGCGTTGGTGGGCTCGGC
Y146A FWD	GACGGATGAGCAGGCCCAGGCAGTGCGGG
Y146A REV	CCCGCACTGCCTGGGCCTGCTCATCCGTC
L141A FWD	CTGTACGGGAAGGTCGCGACGGATGAGCAGTACC
L141A REV	GGTACTGCTCATCCGTCGCGACCTTCCCGTACAG
D134A FWD	CGTTGAGTGGCTGCTGGCTGCTCTGTACGGGAAG
D134A REV	CTTCCCGTACAGAGCAGCCAGCAGCCACTCAACG
E130A FWD	GAGGGTCACAAACGTTGCGTGGCTGCTGGATGCTC
E130A REV	GAGCATCCAGCAGCCACGCAACGTTTGTGACCCTC
L85A FWD	GGCCGGGCAGGCGCAGGCGGCCAC
L85A REV	GTGGCCGCCTGCGCCTGCCCGGCC
Y60A FWD	GCTGGTCAGCTTCGCCCTGGAGACCTACGGC
Y60A REV	GCCGTAGGTCTCCAGGGCGAAGCTGACCAGC
T53A FWD	GACGCCTTGGACCTCGCGGACAAGCTGGTCAG
T53A REV	CTGACCAGCTTGTCCGCGAGGTCCAAGGCGTC

Table 3.12. Primers used in this study (cont.).

Primer Name	**Sequence**
S29A FWD	GCTGAAGCTGCTGGCGGTGCCGCTGCGC
S29A REV	GCGCAGCGGCACCGCCAGCAGCTTCAGC
pET30a FWD	AGCGGATAACAATTCCCCTCT
pET30a REV	AAGACCCGTTTAGAGGCCC
T7promoter	TAATACGACTCACTATAGGG
EGFP-CF	AGCACCCAGTCCGCCCTGAGC

4. METHODS

4.1. Molecular Cloning

4.1.1. Plasmid DNA Isolation

Plasmid DNA isolation was done according to manufacturer's instructions. 5 ml and 200 ml of bacterial liquid culture was used for mini-scale (miniprep) and midi-scale (midiprep) plasmid isolation respectively. Before plasmid isolation, a bacterial stock was taken by mixing 500 μl of liquid culture with 500 μl filter-sterilized 50% glycerol. The bacterial stock was stored in a -80°C freezer. NucleoSpin® Plasmid and NucleoBond® Xtra Midi EF kits (Macherey-Nagel, Germany) were used for miniprep and midiprep respectively.

Elution step was done with 50 μl elution buffer for miniprep, or with 200 μl EF-H_2O for midiprep. Plasmid concentration and purity was checked via Nanodrop (Thermo Fisher Scientific, USA). Plasmids obtained through midiprep were later diluted to have a concentration of 1000 $ng/\mu l$ if it had a higher concentration.

4.1.2. High-Fidelity PCR Reaction

DNA fragments to be cloned into vectors were amplified using Q5 High-Fidelity 2x Master Mix (New England Biolabs, USA). PCR reaction conditions and protocol are summarized in Table 4.1 and Table 4.2. Primer mixes were made to contain 10 $pmoles/\mu l$ of both forward and reverse primers.

4.1.3. Site-Directed Mutagenesis

Site-directed mutagenesis (SDM) was done using the protocol of QuikChange II Site-Directed Mutagenesis Kit (Agilent, USA) modified by insights of Xia et al. [40] In this method, the template plasmid is put through whole-plasmid PCR using semi-

complementary oligonucleotide primers containing the mutation. PCR is done using high-fidelity DNA polymerase preferentially with proof-reading capabilities, creating nicked circular strands including mutagenic primers. Methylated template DNA is digested with DpnI, and the remaining circular, nicked, mutagenic dsDNA is transformed into competent *E.coli* strains. After transformation, the nicks are repaired within the cell.

Table 4.1. PCR program using the Q5 master mix.

Step #	**Description**	**Temperature (°C)**	**Duration**
1	Initial denaturation	95	60 secs
2	Denaturation	95	20 secs
3	Annealing	58	30 secs
4	Elongation	72	30 secs
5	Return to step 2 (34x)		
6	Final Elongation	72	3 mins

Table 4.2. PCR mixture for cloning and site-directed mutagenesis.

Reagent	**Concentration**	**Volume (μl)**
Q5 High-Fidelity 2x Master Mix	2X	25
Primer Mix	10 $pmoles/\mu l$	4
Template	100 $ng/\mu l$	1
ddH_2O		20
Total		50

SDM primers were designed to be in between 25 and 45 bases in length, containing the desired mutation in the center of the primer, with a melting temperature of $\geqslant$78°C, with a minimum GC content of 40% and ending with one or more C or G bases. Primers were designed to have 10-12 bases of complementary region, the desired missense mutation, another 10-12 bases of complementary region, and 10-15 primer specific region, in this order. Reverse and forward primers containing the same mutation were designed to have at most 24 bases of complementarity. Possible hairpin

formation or self-annealing was prevented as much as possible, but in most cases, it is inevitable due to the nature of SDM primers.

PCR was done using Q5 High-Fidelity 2x Master Mix (New England Biolabs, USA), with the final solution described in Table 4.2, and thermal cycling was carried out as described in Table 4.3. Digestion was carried out as described in Section 4.1.4 and transformation into competent *E.coli* strains was done as described in Section 4.1.8. After transformation, 4 random colonies were selected from the culture agar plate and were sent for sequencing.

Table 4.3. PCR program using the Q5 master mix for site-directed mutagenesis.

Step #	**Description**	**Temperature (°C)**	**Duration**
1	Initial denaturation	95	30 secs
2	Denaturation	95	15 secs
3	Annealing	60	30 secs
4	Elongation	72	3 mins
5	Return to step 2 (24x)		
6	Final Elongation	72	2 mins

4.1.4. Restriction Enzyme Digestion

Plasmid DNA or purified PCR products were digested with suitable restriction enzymes for molecular cloning purposes. Restriction enzymes from New England Biolabs, USA were used and digestion reaction was carried out in a 50 μl reaction mix containing 5 μl of appropriate digestion buffer, 1.5 μl restriction enzyme, and the sample to be digested. The digestion was done by incubation at 37°C for an hour.

4.1.5. Agarose Gel Electrophoresis

Digested DNA or PCR products were run on 1% agarose gels for diagnostic purposes or for purification via gel extraction. Agarose gel solution was made according to the system to be used. For gels run on Mini Gel Electrophoresis Kit (IO Rodeo,

USA), 600 mg of agarose was dissolved in 60 ml 1x TAE buffer. For gels run on MP-1015 (IBI Scientific, USA), 1.3 g of agarose was dissolved in 130 ml 1x TAE buffer. The solution was heated in a microwave, with care to not boil the solution. The solution was swirled and reheated until all agarose dissolved. SYBR Green I Nucleic Acid Gel Stain (Roche, Switzerland) was added in 1:10000 ratio, with 6 μl for 60 ml gels and 13 μl for 130 ml gels, and the solution was swirled until it was homogeneous. The solution was then poured onto the casting tray, and combs were placed. The gel was left for cooling until it's hardened. DNA samples to be run on gel were mixed with 6x Purple Gel Loading Dye (New England Biolabs, USA) to have a final dye concentration of 1x. The gels were run at 100 V in tanks containing 1x TAE buffer until the loading dye reached but not passed the bottom of the gel. After the gels were run, images of the gels were observed using a mini LED blue light transilluminator.

4.1.6. PCR Purification and Agarose Gel Extraction

PCR and digestion products were purified using the NucleoSpin® Gel and PCR Clean-up (Macherey-Nagel, Germany) kit according to the manufacturer's instructions. To remove short oligonucleotides - remnants from restriction enzyme digestion - from the solution, the sample to be purified was increased to 200 μl in volume by addition of endotoxin free H_2O, and was mixed with 100 μl NTI binding buffer, to achieve a ratio of 2:1. Short oligonucleotides do not bind to the purification column under low binding buffer concentrations. Large DNA fragments and PCR products were run on agarose gels, and fragments of interest were cut using a scalpel under blue light. DNA fragments from cut agarose pieces were purified using NucleoSpin® Gel and PCR Clean-up (Macherey-Nagel, Germany) kits according to the manufacturer's instructions. Washing step was done twice. Elution buffer was pre-heated to 70°C to ensure maximum DNA yield from the purification column. If the purified product was to be used in ligation experiments, elution was done with EF-H_2O instead.

4.1.7. Ligation of DNA Fragments

Restriction enzyme digested plasmid vectors and inserts were ligated using T4 ligase (New England Biolabs, USA). Due to the length difference between the vectors and the inserts, vector and insert concentrations were adjusted to have 1:7, 1:14 and 1:21 ratios. In each ligation reaction, 50 μg of vector and corresponding amount of insert was used. The reaction was carried out in 20 μl ligation mixes containing 2 μl 10x T4 Ligase buffer and 1 μl T4 ligase. The reaction was carried out in a thermal cycler at 24°C for 10 minutes, followed by inactivation at 65°C for 10 minutes.

4.1.8. Transformation of Plasmids into Competent *E.coli* Strains

The ligated plasmids were transformed into competent Top10 *E.coli* strain. 50 μl aliquots of competent bacteria were incubated on ice for 15 minutes after removal from -80°C freezer. 5 μl of ligation mix or 5 μl of plasmid (100 $ng/\mu l$) was added to the aliquot, and the competent cells and plasmid mix was incubated on ice for 20 minutes. Heat shock was applied to the mixture by incubation in a water bath at 42°C for 45 seconds. The mixture was then promptly removed from the water bath and incubated again on ice for 3 minutes. 300 μl of sterile LB media was added to the mixture, and the mixture was left for incubation on a thermal shaker for an hour at 37°C at 200rpm. After that, 200 μl of the mixture was spread to LB agar plates containing necessary antibiotics, and the plates were incubated at 37°C for 16 hours. Kanamycin was used for antibiotic selection of all plasmids used in this study. Chloramphenicol was used alongside kanamycin when Rosetta pLysS *E.coli* strain was used for transformation to select for Rosetta *E.coli* strain.

4.1.9. Colony PCR

Colony PCR was done to select colonies that contain the correct vector and insert. Colonies were selected at random from plates containing transformed cells. A sterile micropipette tip was used to select a colony, and the tip was then dipped once on a backup LB agar plate containing necessary antibiotics, and then dipped into a 0.2 ml

microcentrifuge tube containing reaction mixture as described in Table 4.4 including PCR MasterMix (Gene and Cell Technologies, USA). PCR was then done according to Table 4.5.

After PCR, the samples were run on an agarose gel described in Section 4.1.5. Colony samples showing desired bands were selected, and miniprep was done from the respective colonies on the backup plate. The isolated plasmids were sent for sequencing.

Table 4.4. PCR mixture for colony PCR.

Reagent	**Concentration**	**Volume (μl)**
PCR MasterMix	5X	5
Primer Mix	10 $pmoles/\mu l$	2
Template		+
ddH_2O		18
Total		25

Table 4.5. PCR program for colony PCR.

Step #	**Description**	**Temperature (°C)**	**Duration**
1	Initial denaturation	98	30 secs
2	Denaturation	98	15 secs
3	Annealing	55	30 secs
4	Elongation	72	45 secs
5	Return to step 2 (34x)		
6	Final Elongation	72	2 mins

4.1.10. Sequencing of Plasmids

Each construct made in this study was checked using Sanger sequencing. Sequencing service was purchased from Macrogen Europe, the Netherlands. EGFP-CF primer was used for sequencing EGFP plasmids, and T7promoter primer was used for sequencing pET30a plasmids.

4.2. Cloning Strategies

4.2.1. pET30a-CARD, pET30a-CARD-E130A

Multiple cloning site in pET30a is in reverse order compared to the other plasmids used in this study, so plasmid cloning via restriction enzyme digestion (subcloning) was not possible.

To make an insert suitable for cloning, forward primers were made to have a 5-base filler of A/T bases, a 6-base restriction site, a 1-base filler to ensure same frame transcription, and 16-base complementary region, in this 5' to 3' order. Reverse primers were made to have a 16-base complementary region, a 3-base stop codon, a 6-base restriction site and a 5-base filler, in this 5' to 3' order. pcDNA3-hASC was used as template for insert production. Restriction sites were chosen as BglII for forward and EcoRI for reverse primer. PCR was done using P2P-CARD forward and reverse primers. After PCR, the samples were run on agarose gels. The band corresponding to the insert was cut and purified using gel extraction.

pET30a-hASC was digested sequentially with BglII and EcoRI to remove hASC, and prepare the vector for insertion. Digestion was done with 2 μg vector. Because BglII and EcoRI do not work efficiently in each other's reaction buffers, after each digestion, the buffers were removed from the solute using NucleoSpin® Gel and PCR Clean-up (Macherey-Nagel, Germany) kit. After both digestions were complete, the sample was run on an agarose gel. Two bands, corresponding to the vector, as well as the cut hASC region, were seen, and the fragment containing the vector was cut for purification via gel extraction.

After ligation and transformation, colony PCR was done with pET30a FWD and pET30a REV primers, spanning the region containing the insert. pET30a-hASC was used as negative control. Negative control and colonies that weren't digested properly and thus closed back on its own during ligation showed bands near 1000 bp, while colonies containing the insert showed bands near 600 bp. Colonies containing the

correct insert were selected, plasmids were isolated through miniprep, and plasmids were then sent to sequencing. Sequencing was done using T7promoter forward primer.

Once pET30a-CARD was obtained, site-directed mutagenesis was done to create the E130A mutation on it. Mutagenesis reaction was done as described in Section 4.1.3 using site-specific primers listed in Table 3.12. After mutagenesis, the mix was transformed into a competent Top10 *E.coli* aliquot. Random colonies were selected from the LB agar plate, and plasmids obtained through miniprep were sent to sequencing. Sequencing was done with T7promoter forward primer.

4.2.2. pEGFP-PYD, pEGFP-CARD Mutant Constructs

pEGFP-C3-PYD and pEGFP-C3-CARD were taken as templates for site-directed mutagenesis. Mutagenesis reaction was done as described in Section 4.1.3 using site-specific primers listed in Table 3.12. After mutagenesis, the mix was transformed into competent Top10 *E.coli* aliquots. Random colonies were selected from the LB agar plate, and plasmids obtained through miniprep were sent to sequencing. Sequencing was done with EGFP-CF forward primer.

4.3. Cell Culture

4.3.1. Maintenance of HEK293 Cells

HEK293 cells were cultured with complete DMEM, modified as listed in Table 3.2, to have a final concentration of 10% FBS, 1x Pen-Strep and 1x MEM-NEAA.

For cell passaging, the culture media was removed by aspiration, the plate was washed once using 6 ml 1x PBS and the cells were collected via trypsinization by adding 3 ml 0.05% Trypsin on 100 mm cell culture dishes. Cells were then centrifuged at 1350 G for 2 minutes, the supernatant was discarded and the pellet was dissolved in 3 ml fresh complete DMEM. 20 μl of culture was taken and mixed with 20 μl Trypan Blue in a 0.5 ml microcentrifuge tube. The cells were then counted using a

hemocytometer. Confluent HEK293 cells grown on 100 mm cell culture dishes roughly consist of 10 million cells. The culture was diluted with complete DMEM to have 2 x 10^6 cells/ml concentration, and seeding was done on new 100 mm culture dishes with 1 ml culture and 9 ml complete DMEM. To ensure homogeneity, the culture plates were gently shaken in random directions after seeding. Culture plates were then stored in an incubator at 37°C with 5% CO_2.

4.3.2. Calcium Phosphate Transfection

Gene transfer by calcium phosphate nanoparticles is a widely used method of transfection for DNA or RNA introduction. Calcium phosphate nanoparticles are non-toxic, and calcium facilitates endosomal/lysosomal escape of nanoparticles as well as enhances the nuclear uptake of DNA through the nuclear pore complex. In this method, calcium chloride solution is mixed with DNA, followed by phosphate-buffered saline solution. This results in the formation of calcium phosphate + DNA precipitates. The aggregates are taken up by the cells when added to a cell culture. [41]

Table 4.6. Substrates used in calcium phosphate transfection for a 100mm cell culture dish.

Reagent	**Amount**
ddH_2O	439 μl (up to)
Plasmid DNA	4 μg
2 M $CaCl_2$	61 μl
2x HBS	500 μl

Plasmid DNA to be transfected was first added to ddH_2O. 2 M $CaCl_2$ was added in a drop-wise manner. Lastly, 2x HBS was added to the transfection mixture. The volumes of substrates used for the transfection mixture is listed in Table 4.6. After the addition of the phosphate group, the solution was mixed through violent pipetting to create bubbles in the solution. This bubbling process is vital to calcium phosphate + DNA precipitation; mixing through shaking or vortexing will result in lower transfection efficiency. After mixing the solution, the transfection mixture is incubated at

room temperature for 5-10 minutes. This incubation time affects proportionately the size of precipitates, thus affects transfection efficiency. After incubation, the transfection solution was mixed gently by pipetting to ensure solution homogeneity, and was then spread to the cell culture plate in a drop-wise manner, covering as many cells as possible. The plates were then placed back into the incubator.

To increase transfection efficiency, chloroquine - to have a final concentration of 25 μM was added to the cell culture plate before transfection. Chloroquine prevents lysosomal degradation of DNA, but is toxic to the cell. Cell culture medium was freshened 8 hours after the addition of chloroquine.

4.3.3. Fluorescence Microscopy

24 hours after transfection images of the cell culture dish were taken with a fluorescence microscope using 5x objective per plate and 40x objective per group. Images were taken once using brightfield, once using B-2A blue excitation filter (Nikon, Japan) and once using G-2A green (Nikon, Japan) excitation filter on automatic exposure.

4.4. Spectrofluorometry

4.4.1. Collection of Transfected Cells

24 hours after transfection, cells were collected in 15 ml falcon tubes via trypsinization. Cells were centrifuged at 1350 G for 2 minutes. The supernatant was removed, and 10 ml 1x PBS was added to the falcon tube. The pellet was dissolved through gentle pipetting, and the cells were again centrifuged at 1350 G for 2 minutes. The supernatant was removed, the pellet was dissolved in 1.5 ml 1x PBS, and was transferred to a 2 ml microcentrifuge tube. Long exposure to ambient lighting partly bleaches the fluorophores for spectrofluorometry measurements, so these steps were done in low ambient lighting.

If the samples weren't to be measured immediately, 30 μl of 50x cOmplete Protease Inhibitor Cocktail (PIC) (Roche, Switzerland) was added to the samples, and samples were stored at 4°C. 100 μl of the samples (with PIC) were taken for protein quantification assays.

4.4.2. Measuring Protein Quantity

Protein quantity of samples were measured using Pierce^{TM} BCA Protein Assay Kit (Thermo Fisher Scientific, USA). For cell lysis, 100 μl 2x RIPA Buffer was added to the samples, followed by incubation on ice for 30 minutes. RIPA Buffer was prepared according to Thermo Scientific's RIPA Buffer contents, as shown in Table 4.7. This buffer is compatible with Pierce^{TM} BCA Protein Assay Kit, but gives false positive results with Pierce^{TM} Coomassie Plus (Bradford) Assay Kit. The samples were then centrifuged at 14000 G for 15 minutes to pellet the cell debris, and 25 μl of the supernatant was pipetted into a 96-well microplate well. 200 μl of working reagent was added to each cell, and the plate was incubated at room temperature for 90 minutes. Absorbance of all samples was measured at 562 nm. RIPA + PBS was used as blank, and albumin standards were used to make the standard concentration curve. Samples were prepared in duplicate.

Table 4.7. Ingredients of RIPA Buffer.

Reagent	**2x RIPA Buffer**
4 M NaCl	3.75 ml
1 M Tris HCl pH 7.4	2.5 ml
Sodium Deoxycholate	1 g
10% SDS Solution	0.1 ml
ddH_2O	(up to) 50 ml

4.4.3. Measuring Samples

Samples were carried to the spectrofluorometer using a closed box. No refrigeration was necessary during carrying. Samples were transferred to a 4 ml quartz cuvette

for measurement and the cuvette was rinsed once with 70% ethanol and once with ddH_2O between each measurement. The cuvette was placed in such a way that the bottom of the cuvette was at the same line as the bottom side of the laser orifice in the spectrofluorometer.

Measurements were taken by exciting the sample at a given wavelength and then measuring the emission spectrum using the provided software. The samples were measured once by excitation at 488 nm and spectrum recording between 488-700 nm, and once by excitation at 588 nm and spectrum recording between 588-700 nm. Sampling rate was set at 1 per nm. Blank measurements were taken using untransfected samples.

4.4.4. Calculating FRET Efficiency

After the total protein quantity of measured samples were collected, each reading was modified to show the measurements for the same concentration. Blank measurements were deducted from each sample reading.

$$IR_n = \frac{(I_n - B_n) * 1000}{Q} \tag{4.1}$$

N_{FRET} calculations were done as described by Hoppe et al. [31] Parameters α and β were calculated using samples expressing only mCherry or only EGFP respectively. Emission spectrum containing I_A, I_D and I_F were collected in triplicate for both samples. From the emission spectra, α (mCherry) and β (EGFP) were calculated as

$$\alpha = \frac{I_F}{I_A} \tag{4.2}$$

$$\beta = \frac{I_F}{I_D} \tag{4.3}$$

In our calculations, we found $\beta = 0,0326$ and $\alpha = 0,0624$. These values are used to deduct basal EGFP and mCherry fluorescence from the emission spectra. N_{FRET} was

calculated as follows:

$$N_{FRET} = \frac{I_F - \alpha I_A - \beta I_D}{\sqrt{I_A * I_D}} \tag{4.4}$$

I_F and I_D were taken from the arbitrary unit readings at 607 nm and 508 nm respectively when the sample was excited at donor excitation wavelength. I_A was taken from the arbitrary unit readings at 608 nm when the sample was excited at acceptor excitation wavelength. Maximum peaks were observed at these wavelengths. Calculations were done for each replicate in a group.

After N_{FRET} of all samples were calculated, the values were put through 1-way ANOVA, and statistical significance was calculated using Dunnett's Test.

4.5. Confocal Analysis

4.5.1. Seeding of Cells on Cover Slips

Two 20 mm x 20 mm cover slips were placed in 100 mm cell culture dishes, and were sterilized by UV light irradiation for at least an hour. HEK293 cells were added to the dishes, maintenance was done as described in Section 4.3.1, and transfection was carried out as described in Section 4.3.2.

4.5.2. Fixation and Preparation of Samples

24 hours after transfection the cell culture dishes containing the cover slips were washed twice with 1x PBS. For fixation, 500 μl 4% PFA was added directly on top of the cover slips, and cover slips were incubated at room temperature for 5 minutes. Cover slips were washed again with 1x PBS. Cover slips were then grabbed from the cell culture dish using forceps, flipped and placed upside down on microscope slides with 20 μl mounting medium in between. Sample slides were stored in a closed box at 4°C.

4.5.3. Visualization by Confocal Microscope

Fluorophores were excited and emission images were taken using the settings given in Table 4.8. Images were taken using 5x and 40x objectives. A few drops of ddH_2O were placed between the objective and the sample to prevent light refraction.

Table 4.8. Settings used in confocal microscopy. Argon laser was used at 13% laser power.

Fluorophore	**Laser**	**Intensity**	**Excitation**	**Emission Range**
EGFP	Ar, 65mW	21%	488 nm	493 nm - 578 nm
mCherry	HeNe, 1mW	23%	543 nm	601 nm - 748 nm
FRET	Ar, 65mW	20%	488 nm	601 nm - 748 nm

4.5.4. Photobleaching

Samples were excited by 543 nm laser at 13% laser power and 100% intensity using 40x objective and additional 20x or 40x masked zooming. Samples showed near no fluorescent activity after 30 minutes for 20x masked zooming, and after 10 minutes for 40x masked zooming. Images of the target area were taken before and after bleaching at 5x masked zooming using the settings described in Table 4.8. Pixel intensities of the bleached area were measured by Leica Advanced Fluorescence Application Suite (Leica Microsystems, Germany), and compared.

4.6. Protein Expression

4.6.1. Liquid Culture

pET30a plasmids containing CARD were transformed into competent Rosetta pLysS *E.coli* strain cells according to Section 4.1.8. A colony was picked at random and added to a starter culture of 25 ml LB broth containing 25 μl kanamycin (1000x) and 25 μl chloramphenicol (1000x). Starter culture was incubated at 37°C for 16 hours.

The main culture was made according to Table 4.9. All ingredients, with the exception of antibiotics, were prepared and autoclave-sterilized separately. 20% glucose was stored at 4°C while 20x M9 salts was stored in room temperature. 1 L LB broth was incubated, preferably overnight, at 37°C prior to use.

Table 4.9. Main culture ingredients.

Reagent	**Volume (ml)**
LB Broth	1000
20% Glucose	20
20x M9 Salts	50
Kanamycin (1000x)	1
Chloramphenicol (1000x)	1

10 ml of 25 ml starter culture was added to the 1 L main culture, diluting it 1:100. 1 ml samples from the culture were taken every half hour to measure OD_{600} of the culture. 1 ml of 1 M IPTG was added to the main culture when a reading between 0.6 - 0.8 was observed at OD_{600}. A 1 ml sample was taken before the addition of IPTG, then 1 ml samples were taken every hour after the addition, for 4 hours. Generally it has taken 150 minutes for the main culture to reach $OD_{600} = 0.6$ and 2 hours of induction to obtain the best results. After induction, the main culture was centrifuged using two 250 ml centrifuge bottles at 6000 G for 10 minutes, and the supernatant was discarded. This centrifugation step was repeated with the same bottles until the entire culture was processed. At the last centrifugation step, 35 ml of supernatant was kept, and the pellet was dissolved through vortexing. Due to the high concentration of cells, it may take a while for the pellet to dissolve completely. Two 50 ml falcon tubes were weighed, recorded and then the samples were transferred to the falcon tubes. Centrifugation was done at 6000 G for 10 minutes, and the supernatant was completely discarded. The weight of the bacterial pellets were recorded, and the pellets were stored at -80°C until further use.

4.6.2. Rough Purification of Samples

Sample pellet was dissolved in modified binding buffer to have 50 mg pellet per ml. The samples were sonicated thrice for 5 seconds at 5x10% and at 50% power. After each sonication the samples were shaken rigorously to ensure homogeneity. The samples were then centrifuged for 10 minutes at 6000 G. The supernatant was transferred to a 50 ml centrifuge tube.

4.6.3. Protein Purification Through Affinity Columns

Protein purification was done with 5 ml HisTrap^{TM} High Performance Columns (GE Healthcare, UK) according to the manufacturer's instructions.

Because of the nature of ASC and its domains, the protein can self-polymerize, and can block the column. It was observed that in presence of KCl, ASC is able to stay in monomeric form [24]. It was assumed that the same properties would apply to domains of ASC as well, so all solutions used in the purification process were modified to have a final concentration of 300 mM KCl, as shown in Table 4.11. All solutions have been adjusted to have a pH of 7.4 as per manufacturer's instructions.

Table 4.10. Solutions used in HisTrap^{TM} HP column chromatography.

Reagent	**2x Binding Buffer**	**Blank Run EB**	**2x Imid-Free Buffer**
Na_2HPO_4	2.84 g (40 mM)	1.42 g (20 mM)	2.84 g (40 mM)
NaCl	29.22 g (1 M)	14.61 g (0.5 M)	29.22 g (1 M)
Imidazole	1.36 g (40 mM)	8.51 g (0.5 M)	-
ddH_2O	500 ml		

Before each purification, a blank run was done to equilibrate the column. A peristaltic pump was used to ensure persistent flow through the column. 2.4 x 0.8 mm tubing was used with a rate of 60 rpm for blank run, and 24 rpm for all steps following sample introduction. These speeds are roughly equal to a flow rate of two and a half columns per minute and one column per minute respectively. A 0.22 μm filter was

attached to the column and was used to filter all solutions passing through the column. In some cases, the sample collected from the bacterial culture was too concentrated to pass through the filter. In that case, the sample was diluted with binding buffer in a ratio of 1:5 or 1:10 and the sample was applied again to the column. This way, the majority of the sample were able to pass through the filter before clogging it. Elution was done semi-gradient using one column volume of each of the elution buffers listed in Table 4.12.

Table 4.11. Modified binding buffer used in HisTrap™ HP column chromatography.

Reagent	**1x Binding Buffer**
2x Binding Buffer	250 ml
3 M KCl	50 ml (300mM)
ddH_2O	200 ml

Table 4.12. Elution buffers used in HisTrap™ HP column chromatography.

Elution Buffer	**50 mM**	**100 mM**	**150 mM**	**200 mM**	**250 mM**
2x Imid-Free Buffer	25 ml				
3 M KCl	5 ml				
Imidazole	0.17 g	0.34 g	0.51 g	0.68 g	0.85 g
ddH_2O	20 ml				
Elution Buffer	**300 mM**	**350 mM**	**400 mM**	**450 mM**	**500 mM**
2x Imid-Free Buffer	25 ml				
3 M KCl	5 ml				
Imidazole	1.02 g	1.19 g	1.36 g	1.53 g	1.70 g
ddH_2O	20 ml				

4.6.4. Analysis of Purified Protein

SDS-PAGE was carried out to analyze samples eluted from the affinity column. Samples were mixed with 5x Laemmli Buffer to a total of 40 μl (final concentration of 1x) and were incubated at 95°C for 10 minutes. 4%-15% 1.5 mm gels were used for

SDS-PAGE. First, 1.5 mm glass plates were cleaned with 70% ethanol and were then clamped together and the bottom was sealed using the casting apparatus. The 15% gel solution was put in between the plates and the top of the solution was covered with isopropanol immediately afterwards to ensure a straight surface. After the resolving gel polymerized, isopropanol was drained off, the 4% gel solution was added on top of the resolving gel, and the desired 10- or 15-well comb was placed. The gels were used immediately after polymerization of the stacking gel. Gels were placed in a vertical electrophoresis tank filled with 1x running buffer. Samples were run at 90 V until the bands passed the stacking gel and at 140 V afterwards until the loading dye reached but not passed the bottom of the gel. After the run was complete, the gels were taken out and washed twice with ddH_2O for 10 minutes, and then were stained overnight using Coomassie G-250 staining solution.

4.6.5. Concentration Adjustment of Purified Protein

Concentrating the protein was attempted via the use of centrifugal concentrators, however, concentrators with MWCOs of 5K and 10K failed to properly concentrate the sample. So, to concentrate the desired protein, the eluted samples were diluted using modified binding buffer (to decrease imidazole concentration), put through a 1 ml HisTrap^{TM} column and the purification was done as described in Section 4.6.3. The protein concentration was then checked using Pierce^{TM} Coomassie Plus Assay Kit (Thermo Fisher Scientific, USA) with BSA standards in the 0-25 $\mu g/ml$ range, using 300 mM elution buffer as blank, following the manufacturer's instructions. The final concentration of the protein solution was diluted to be 10 $\mu g/ml$.

4.6.6. Dialysis

The purified protein samples were put through dialysis to remove imidazole from the solution. A small part of Spectra/Por 7® 1K MWCO dialysis tubing was cut, and one end was closed using a small clip. The sample was put in the tubing, and the open end was closed using another clip. The tubing was then put in a 1L beaker containing 1x PBS + 300 mM KCl, and was incubated overnight at 4°C with gentle stirring. After

dialysis, one end of the tubing was opened and the sample was collected carefully using a micropipette. To ensure that the protein was not lost, a small quantity of the sample was taken for SDS-PAGE analysis.

4.7. Atomic Force Microscopy

MLCT model probes (Bruker, USA) functionalized with PEG and Ni^{2+}-NTA groups and mica 20 mm x 20 mm surfaces functionalized with Ni^{2+}-NTA groups were purchased from Novascan, USA. Prior to experimentation, the probe holder, a pair of extra fine-tipped tweezers and a cover slip were washed once with 70% ethanol and once with ddH_2O. The items were all dried by dabbing gently with lint-free tissue. The probe holder was then attached to a working station, and the probe was slid in using tweezers. The probe holder was then attached to the AFM head. Before calibration, it was checked whether the camera of the probe holder could see cantilevers C and E. If not, the probe holder was removed from the head, and the probe was gently moved a bit to ensure observance of both cantilevers, and the probe holder was attached back to the head. The laser was pointed to the top of the desired cantilever using adjustment screws. After ensuring the laser was being reflected from the desired cantilever, the mirrors directing the reflected signal to the sensor were adjusted to make sure the laser is reflected to the center of the sensor. The mirrors were adjusted to allow almost no signal intensity difference between the left side and the right side of the sensor. The mirrors were adjusted to reflect the laser slightly to the bottom side of the sensor, but the signal difference between the top and bottom sides of the sensor was always kept lower than signal sum.

To calibrate the cantilevers, the probe was engaged and lowered on to a clean cover slip. The AFM was prone to false engage every now and then, meaning that the cantilever would not actually touch the surface, despite the program telling so, so the probe was manually lowered further using 1-5 μm steps, and a reading of tapping between 0 μm and -5 μm was taken at each step. Once the probe touched the surface, readings from single tapping events were taken and two points on the force-distance graph that are closest to but above the baseline were selected to calculate slope of the

force curve and thus sensitivity of the cantilever. Sensitivity of the cantilever was taken as an average of five separate slope measurements. The probe was then disengaged and lifted to a height of 1 mm from the surface for thermal tuning. Using the calculated sensitivity, and the nominal spring constant listed in the manufacturer's manual, the actual spring constant of the cantilever at resonant frequency was obtained.

After calibration, the probe was dipped onto a cover slip with 100 μl solution containing 10 $\mu g/ml$ sample protein, and was incubated at room temperature for 80 minutes. After incubation, the probe was lifted up from the solution, and was dipped on 100 μl ddH_2O. This washing step was done twice. The surface was covered with 200 μl solution containing 10 $\mu g/ml$ sample protein, and was incubated at room temperature for 60 minutes. After incubation, the cover slip was washed twice with 200 μl ddH_2O with pipetting from the side of the surface. After washing, the surface was incubated with 200 μl 20 $\mu g/ml$ BSA for 20 minutes at room temperature. After incubation, the surface was washed again twice with ddH_2O. Finally, the surface was covered with 100 μl PBS, and the probe was engaged and lowered to the surface. After contact was ensured, calibration was repeated as described previously to calculate sensitivity of the cantilever in PBS. Using the newly calculated sensitivity, and the previously calculated spring constant, the relation between voltage (what the sensor reads) and force (in pN) was calculated. The calculated spring constants and sensitivities can be found in Table 4.13.

For each loading rate, more than 200 readings were collected. After all rates for a cantilever was done, the probe was disengaged, the position of the surface was changed slightly, and the probe was engaged again.

In tapping experiments, the probe was pressed to the surface to reach a maximum force of 1000 pN before lifted. In most cases, the baseline slightly moved across the graph during the experiment, so the maximum force was adjusted back to 1000 pN whenever possible.

Table 4.13. Calculated sensitivity (in PBS) and spring constant of cantilevers.

Probe	**Sensitivity** ($\mu m/V$)	**Spring Constant (N/m)**	**Used in Exp. #**
1C	0,1166	0,0124	1
1E	0,077	0,189	1
4C	0,1066	0,0148	2
4E	0,0439	0,184	2
5C	0,1145	0,0153	3
5E	0,0447	0,175	3
7C	0,115	0,0169	4
7E	0,0641	0,175	4
8C	0,115	0,0141	5
8E	0,039	0,202	5
9C	0,1135	0,0146	6
9E	0,0628	0,175	6

Table 4.14. Settings used in atomic force microscopy. "Cycle Hold": Duration of time where the probe is kept away from the surface. "1/2 Cycle Hold": Duration of time where the probe is held in contact with the surface.

Rate ($\mu m/sec$)	**Cantilever**	**Cycle Hold (sec)**	**1/2 Cycle Hold (sec)**
100	E	0,5	1
50	E	0,5	1
20	C	0,5	0,5
10	C	0,5	0,5
5	C	0,5	0,5
2,5	C	0,5	0,5
1	C	0,5	0,5
0,5	C	0	0
0,1	C	0	0

The controller of the atomic force microscope was connected to a data acquisition and control unit for saving measurements, as well as to an oscilloscope for continuous observation of the signals. The settings used for data acquisition can be seen in Table 4.15.

Table 4.15. Settings used for data acquisition.

Rate ($\mu m/sec$)	**# of Samples**	**Sample Rate (ms)**	**Chart Length (sec)**
100	80000	0,02	1,6
50	50000	0,05	2,5
20	25000	0,1	2,5
10	25000	0,1	2,5
5	25000	0,2	5
2,5	30000	0,2	6
1	50000	0,2	10
0,5	50000	0,2	10
0,1	20000	2,5	50

After the data was collected, a MATLAB script written by Kate Crawford and Fidan Sümbül, Ph.D. was used for rough data analysis. This script takes the folder where the recorded data is located, and given the spring constant and the sensitivity of the cantilever, posts the data as a line graph one after another. At each graph, the number of peaks in the graph is entered, and if there are any, perfect and imperfect events are identified before moving on to the next graph.

Perfect events are events with a clear, noiseless force curve, and a direct, single-step break, as shown in Figure 4.1. Events are considered as imperfect when they more or less resemble perfect events, but have features that make them different from perfect events, for example, step-wise increase in force instead of gradual, break showing noise instead of being clear-cut, the peak of the event being rounded instead of being a peak point etc. The figure is explained as follows: (A, H) Resting state of the probe inside buffer with no contact to the surface, considered baseline signal in the experiment. (B) Force increase as the probe contacts the surface. A maximum of 1000 pN is applied

after contact, making the peak. (C) Force release as the probe is retracted from the surface. (D) Adhesion force; the cantilever sticks a bit to the surface with every touching experiment. (E) Start of an event. The observed force gradually increases as the cantilever bends. (F) Peak of an event. At this point the applied force is enough to break the attraction between the molecule on the surface and the molecule on the probe. (G) Instant break of interaction, returning to baseline signal in this instance.

At each peak, the number of events within said peak are counted, and three key spots are marked for every event. These key spots are: (1) a spot close to the peak, on the force curve, (2) the peak, and (3) the end of the break. The first two spots are used to calculate the slope of the curve, while the latter two are used to calculate the measured force.

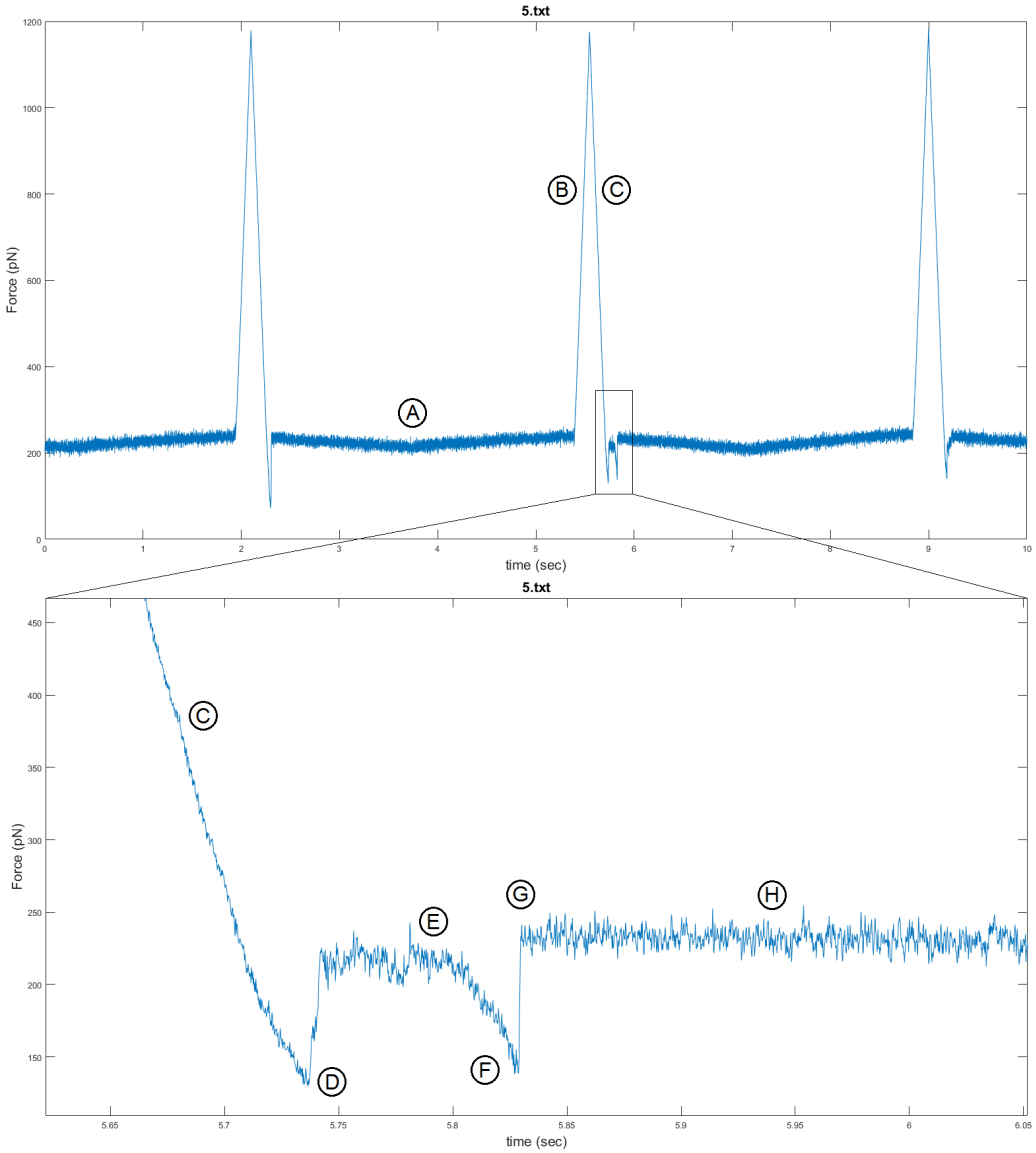

Figure 4.1. A typical AFM recording showing a perfect event.

5. EXPERIMENTS AND RESULTS

5.1. PYD and CARD Fusion Proteins Show Structural Formations and Co-Localization When Expressed

To characterize the ability of fluorescently labeled subdomains of ASC to form oligomeric structures, we have performed a set of overexpression studies in HEK293 cells using the wildtype variant of PYD and CARD. HEK293 seeded in 100 mm plates were co-transfected with mCherry-PYD and either empty EGFP vector or EGFP-PYD. In cells expressing mCherry-PYD and only EGFP, EGFP was found to be equally distributed in cells while in cells expressing both fusion proteins, mCherry-PYD and EGFP-PYD were able to form filamentous structures. EGFP-PYD and mCherry-PYD fusion proteins also showed co-localization inside cell. (Figure 5.1)

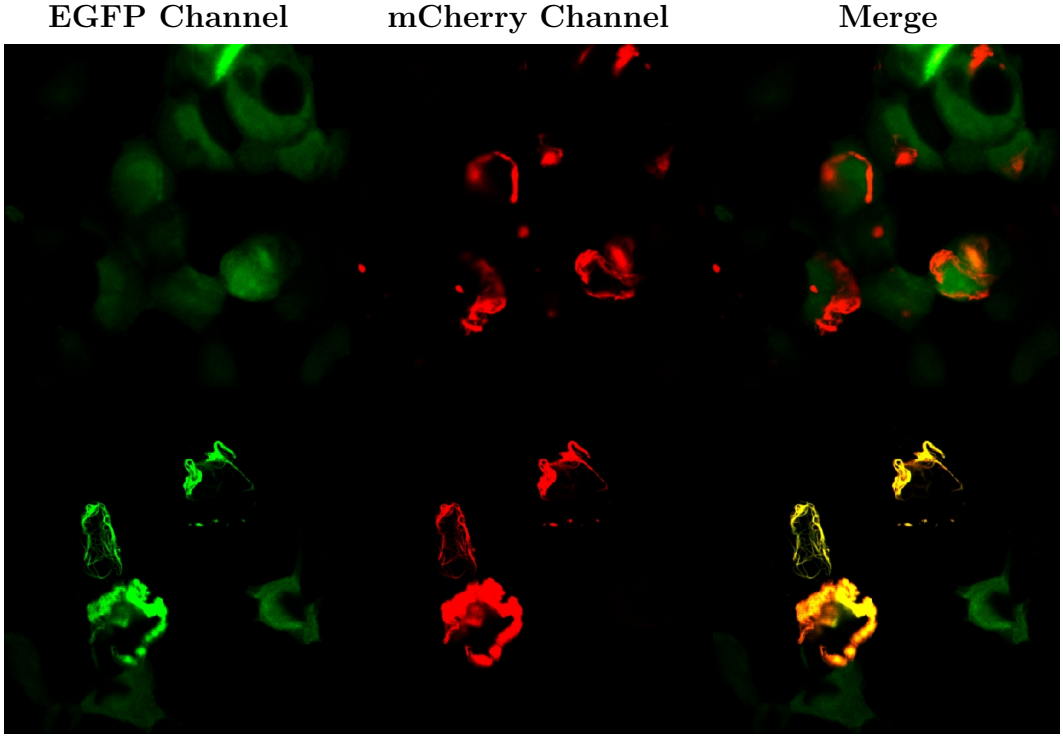

Figure 5.1. Confocal images of cells co-transfected with empty EGFP plasmid and mCherry-PYD (above) and EGFP-PYD and mCherry-PYD (below).

Another co-transfection experiment was done with mCherry-CARD and either empty EGFP vector or EGFP-CARD. Similar to PYD fusion proteins, EGFP-CARD and mCherry-CARD fusion proteins were able to form filamentous structures, and showed co-localization inside cell, while EGFP alone was found to be homogeneously soluble inside cells. (Figure 5.2)

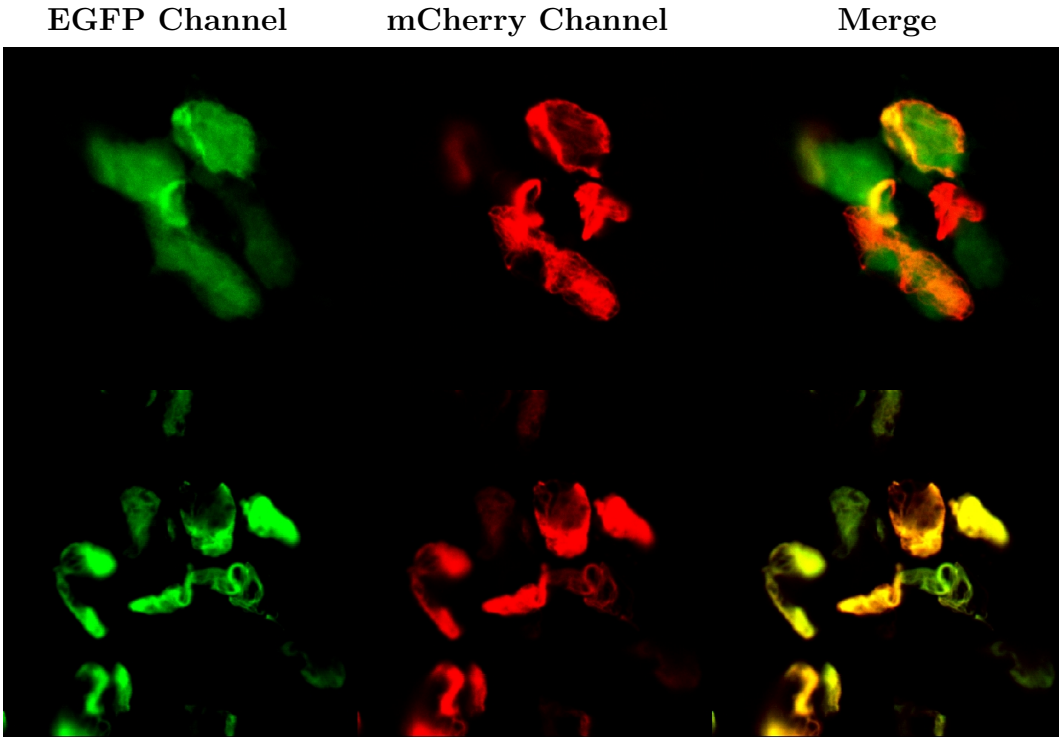

Figure 5.2. Confocal images of cells co-transfected with empty EGFP plasmid and mCherry-CARD (above) and EGFP-CARD and mCherry-CARD (below).

5.2. mCherry Photobleaching Results in Increased EGFP Fluorescence

To establish whether fluorescently tagged PYD or CARD domains are in the range to allow energy transfer, a preparatory experiment was conducted where the effect of photobleaching the acceptor fluorophore was analyzed. HEK293 cells seeded on microscope cover slips were co-transfected with mCherry-CARD/PYD and EGFP-CARD/PYD plasmids respectively. After fixation, cells expressing both fusion proteins were selected, and photobleaching was done as described in Section 4.5.4. The cell was selected as a region of interest in images, and fluorescence intensity was measured

through calculating the intensity average of all pixels inside the region of interest. In all photobleaching experiments, an increase in fluorescence intensity for EGFP could be observed (Figure 5.3), ranging from 1.7-fold to 1.3-fold. This experiment was repeated five times for both CARD and PYD fusion proteins, and obtained intensity ratios between images before and after photobleaching was put through t-test for significance (Figure 5.4).

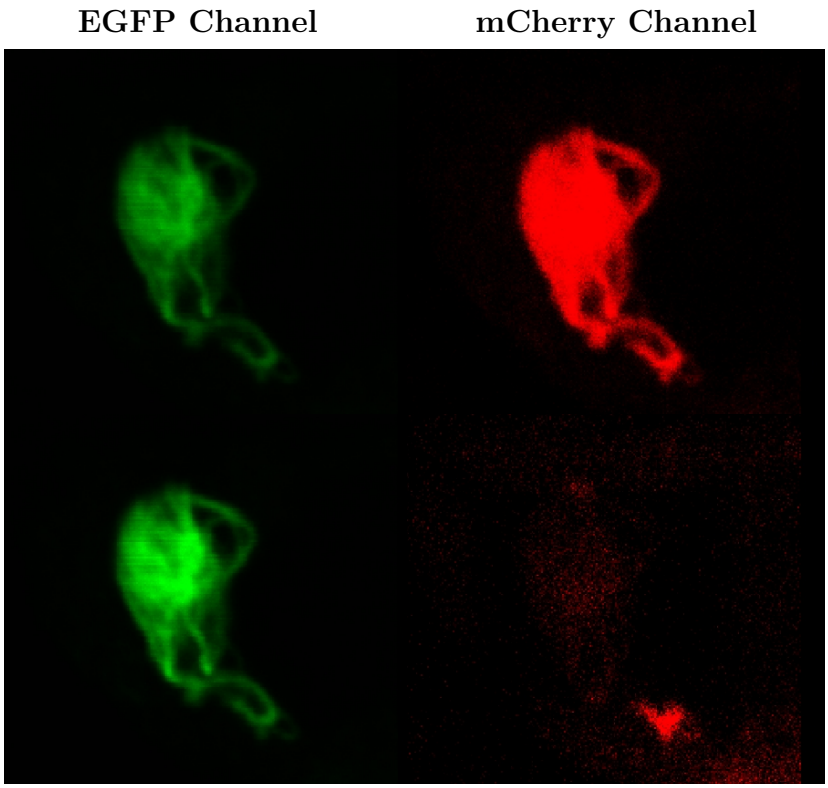

Figure 5.3. Confocal images of cells expressing EGFP-PYD and mCherry-PYD before (above) and after (below) photobleaching.

These results indicate that PYD and CARD fusion proteins are able to show FRET activity between fluorophores. The wide range of increase in fluorescence intensity is most probably due to inequal expression of fusion proteins. Regardless, apFRET results show that FRET is a possible indicator of homotypic PYD-PYD or CARD-CARD interactions.

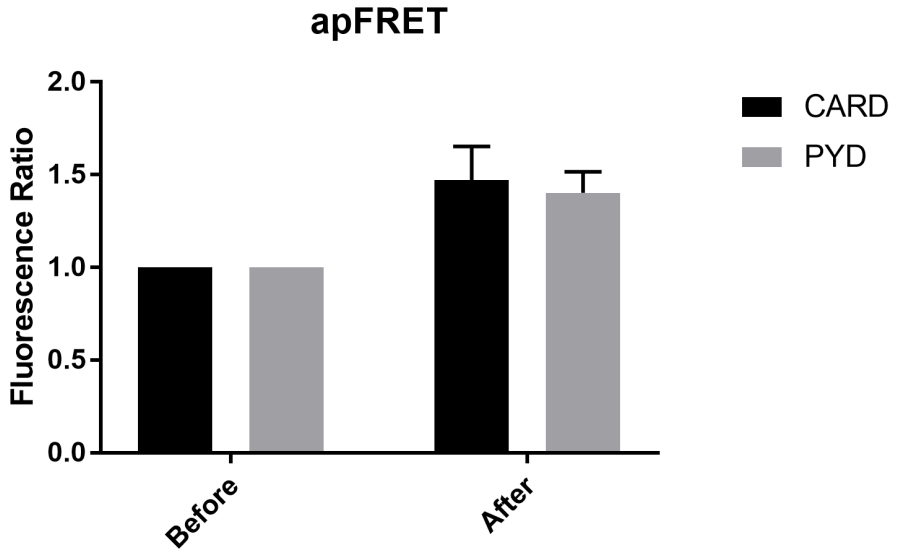

Figure 5.4. Fluorescence intensity of EGFP fusion proteins before and after photobleaching, showing significant ($p \leq 0.05$) increase after bleaching.

5.3. seFRET Measurements Show Secondary Peak In Emission Spectra

Before initiating seFRET measurements of mutant PYD or CARD constructs, conditions for collection of samples and sample preparation were optimized and possible calculation models for achieving maximum benefit from the data were tested. HEK293 cells seeded on 100 mm plates were co-transfected with mCherry-CARD/PYD and EGFP-CARD/PYD plasmids respectively. Cells were collected as described in Section 4.4.1 and fluorescence intensity of samples were measured as described in Section 4.4.3. EGFP and mCherry have their emission maxima at 508 and 607 nm respectively. Normally, cells expressing only EGFP would show a single peak in emission spectrum; at 508 nm, when excited at 488 nm. Since mCherry and EGFP fusion proteins co-localize, considering apFRET results, it was expected that another peak in emission spectrum, at 608 nm would be observed, as the energy transfer from EGFP to mCherry would allow for slight mCherry fluorescence. It was also expected that there would be a decrease in EGFP intensity in cells expressing fusion proteins compared to cells expressing single EGFP, as apFRET results showed that in case of FRET, donor fluorescence is quenched.

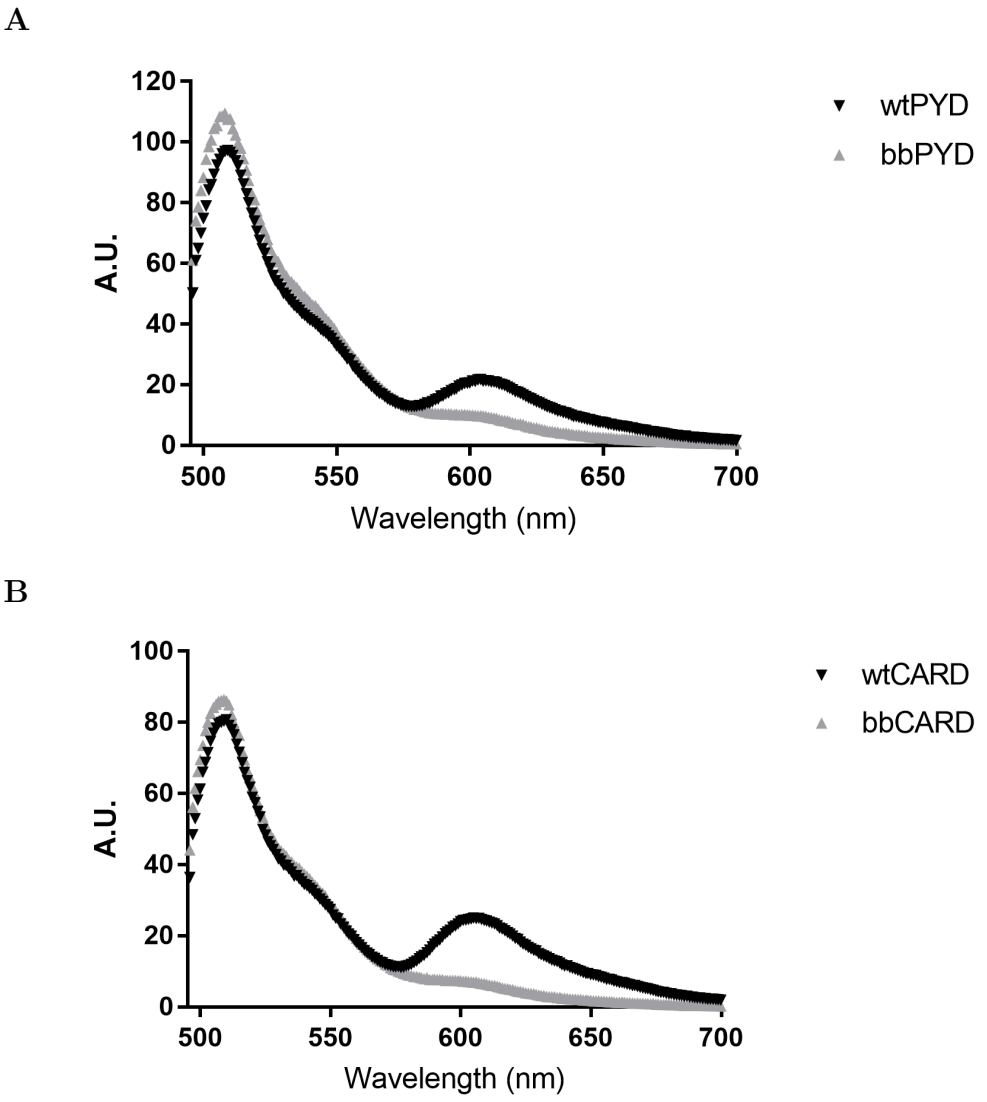

Figure 5.5. Emission spectra of cells expressing (A) PYD fusion proteins and (B) CARD fusion proteins when excited at 488 nm. "bb" indicates cells expressing mCherry fusion protein and only EGFP while "wt" indicates cells expressing both fusion proteins. Raw data.

As expected, cells expressing both fusion proteins showed a secondary peak in their emission spectra when excited at 488 nm, corresponding to mCherry's emission maximum (Figure 5.5). This secondary peak at 607 nm shows that EGFP fusion proteins are able to stimulate mCherry fusion proteins. This is not to be confused with the basal fluorescence of mCherry when excited at 488 nm, as the basal fluorescence is present in both "wt" and "bb" conditions. This complements the results of apFRET and shows that FRET is an applicable tool in displaying the efficiency of homotypic interactions between PYD or CARD molecules. The slight decrease in EGFP emission maxima in "wt" cells compared to "bb" may be attested to the quenching of EGFP due to FRET activity, however, the difference between fluorescence intensities was not found significant.

5.4. Mutational Screen of PYD and CARD Constructs

In previous studies it was found that certain amino acid mutations on ASC or its domains prevent complete homooligomerization. [17, 42–44] In one particular study, it was additionally mentioned that some mutant variants are still able to contribute to the structure in the presence of a wildtype variant. [17] Another study showed that this event may happen in a dose dependent manner. [42] In order to have a broader understanding of this property, mutations that either show unique phenotypes or are at important interaction sites were selected for co-expression experiments. Alanine-scanning was preferred as a method for the identification of functional epitopes. The role of sidechain functional groups at specific positions can be inferred from alanine mutations. The methyl sidechain of alanine lacks unusual backbone dihedral angle preferences while not introducing conformational flexibility to the protein backbone, and alanine substitutions are generally easier, requiring only one or two bases to be substituted to create alanine codons. [45] The created alanine mutations, as well as their properties and locations on the respective ASC domains are listed in Table 5.1 and Table 5.2. While revisiting PYD mutants previously studied, we have investigated the significance of four amino acids (S29, T53, Y60 and L85) that were not studied before. Residues S29 and Y60 were considered to be hinge residues while residues T53

and L85 were found to be highly conserved. [17] With the exception of M159A and R160A, all CARD mutants investigated in this study are first of their kind. E130 and D134 were investigated before, but not with alanine mutations [43].

Table 5.1. PYD mutations investigated in this study.

Mutation	**Location**	**Known Properties**
E13A	H1 outward, near H1&H2 loop, on type III surface	Mutation on full-length ASC prevents speck formation. [17, 42, 44]
E19A	H2, near H1&H2 loop	Mutation on full-length ASC prevents speck formation. [17, 44]
K21A	H2 outward, on type I surface	Mutation on full-length ASC prevents speck formation. [17, 42, 44]
L25A	H2 outward	Leads to unique ASC speck phenotype. [17, 44]
K26A	H2, on type I surface	Mutation on full-length ASC prevents speck formation. [17, 44]
S29A	H2, near H2&H3 loop	Hinge residue. [17]
D51A	H4, near H3&H4 loop, on type I surface	Mutation on full-length ASC prevents speck formation. [17, 42]
T53A	H4 inward	High conservation score. [17]
Y60A	H4&H5 loop	Hinge residue. [17]
L68A	H5	Mutation on full-length ASC prevents speck formation. [17, 44]
L73A	H5 inward	Mutation on full-length ASC prevents speck formation. [17]
L85A	H6 inward	High conservation score. [17]

Table 5.2. CARD mutations investigated in this study.

Mutation	**Location**	**Known Properties**
E130A	H2, near H1&H2 loop, caspase-1 interaction site	Different mutation on residue on full-length ASC prevents speck formation. [42, 43]
D134A	H2 outward, caspase-1 interaction site	Different mutation on residue on full-length ASC prevents speck formation. [42, 43]
L141A	H2&H3 loop	High conservation score. [17]
Y146A	H3	High conservation score. [17]
P156A	H4, near H3&H4 loop	High conservation score. [17]
M159A	H4 inward	Mutation on full-length ASC prevents speck formation. [17]
R160A	H4	Mutation on full-length ASC prevents speck formation. [17]

5.4.1. Localization of PYD or CARD Mutant Variants in Cells as Soluble Proteins or Filamentous Structures

To visualize the folding patterns of fluorescently labeled wildtype PYD or CARD as well as their mutant variants inside the cell, an extensive fluorescence microscopy analysis was conducted. Based on previous experiments, we expected mutant variants with disrupted interaction surfaces to be in monomeric soluble form, while expecting some mutants to retain their ability to form multimeric structures, even if not as much as their wildtype counterparts. HEK293 cells were grown on 100 mm cell culture dishes and were co-transfected with plasmids containing EGFP fused mutant and wildtype variants and mCherry fused wildtype PYD or CARD. Cells expressing mCherry wildtype fusion proteins and only EGFP were chosen as negative control while cells expressing both wildtype fusion proteins were selected as positive control. Images of cell culture dishes were taken using fluorescence microscopy. All taken images can be found in Appendix B.

In coherence with confocal analysis, cells expressing mCherry wildtype fusion proteins and only EGFP ("bb") showed no co-localization between fluorophores, and cells expressing both wildtype fusion proteins ("wt") showed co-localization on filamentous structures (Figure 5.6 and Figure 5.7). While most PYD mutants showed co-localization with wildtype PYD, the variant carrying Y60A mutation showed weak contribution to the filamentous structures, and was found to be mostly distributed throughout the cells. Other investigated PYD variants mostly showed distinct co-localization with their wildtype counterpart. (Figure 5.6) An especially curious result was the formation of filaments on E13A, K21A, K26A and D51A mutant variants. Despite the disruption of type I or type III interaction surfaces, these mutant variants were still able to contribute to multimeric structures.

CARD mutant variants showed a wider variety of phenotypes, ranging from co-localization (E130A and P156A) to being homogeneously distributed inside the cell (D134A and R160A) (Figure 5.7). Despite being on the same helix, and thus on the same interaction surface, D134A and E130A show drastically different phenotypes. This is especially curious considering both residues are negatively charged amino acids. Fluorescence images taken with the EGFP filter show a slightly yellow color when filamentous structures are present. It's believed that this is due to the FRET activity between the fluorophores, causing the red color of mCherry to mix with EGFP, resulting in a yellow hue.

5.4.2. Decrease in FRET Efficiency of CARD or PYD Mutant Variants

To be able to generate quantitative parameters for type I, type II and type III interactions of PYD and CARD domains, we have employed FRET efficiency measurements of PYD and CARD mutants and established a mathematical model to accurately represent the binding or interaction efficiency between the helices of mutant or wildtype PYD/CARD variants. HEK293 cells were grown on 100 mm cell culture dishes and were co-transfected with plasmids containing EGFP fused mutant variants of PYD/CARD and mCherry fused wildtype variant of PYD/CARD. Cells were collected as described in Section 4.4.1 and fluorescence intensity of samples were mea-

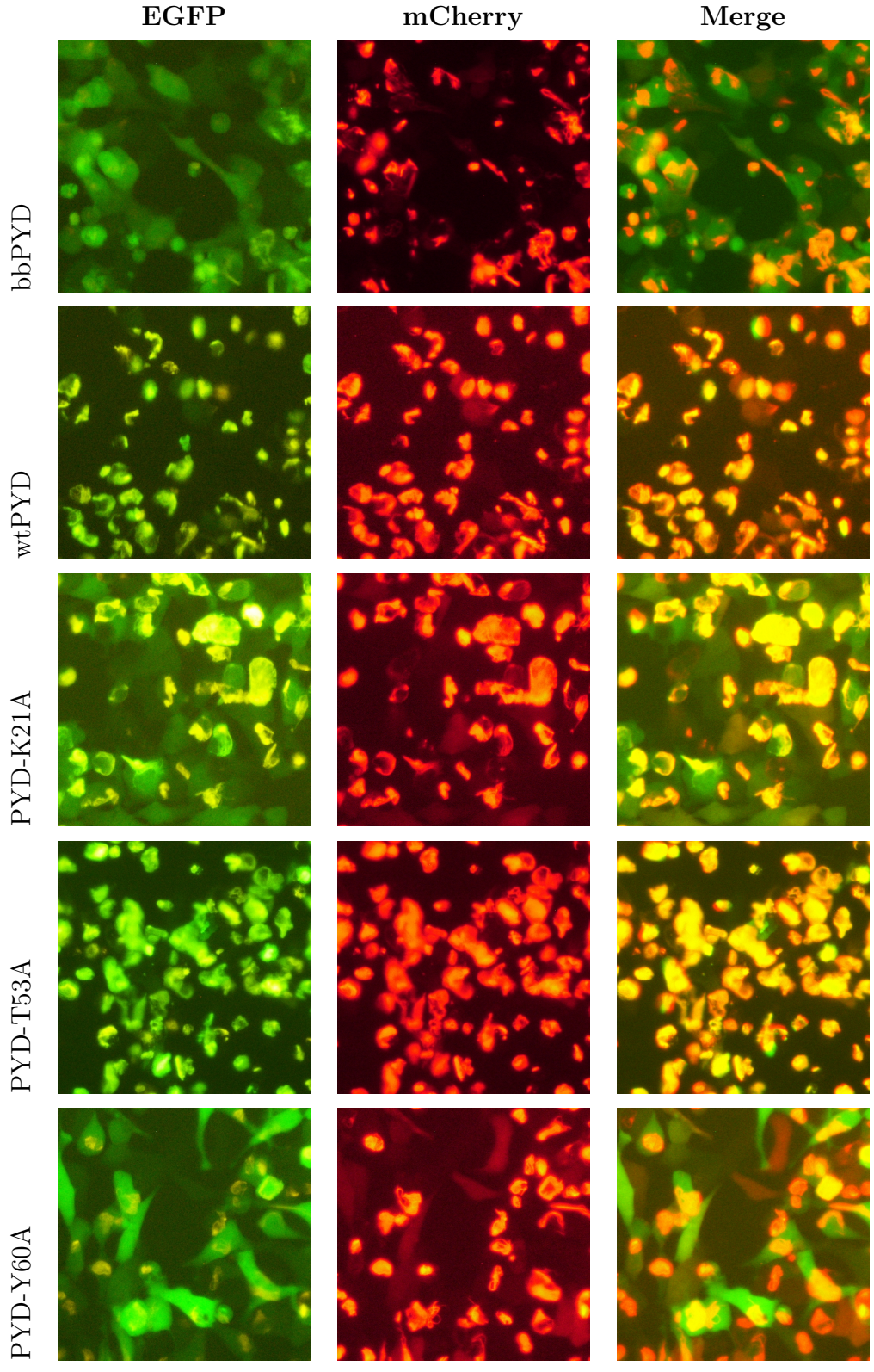

Figure 5.6. Fluorescence images of cells co-expressing mCherry-PYD and PYD variants listed at left. "bb" means EGFP only and "wt" means EGFP-PYD.

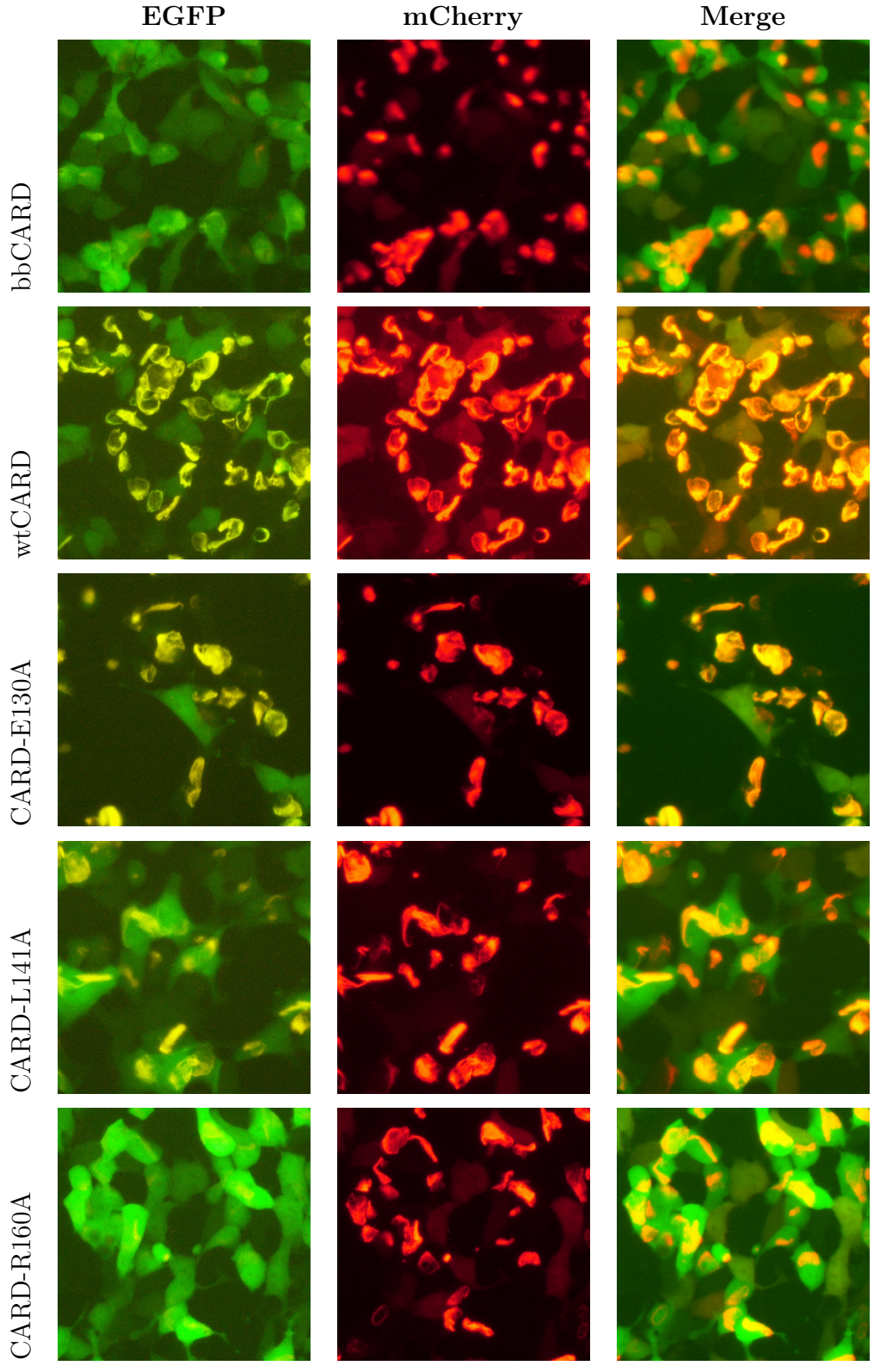

Figure 5.7. Fluorescence images of cells co-expressing with mCherry-CARD and CARD variants listed at left. "bb" means EGFP only and "wt" means EGFP-CARD.

sured as described in Section 4.4.3. This experiment was done in triplicate. Averages of emission spectra for all samples can be found in Figure A.1 and Figure A.2.

Before calculating FRET efficiency, the basal fluorescence of EGFP and mCherry should be obtained. In order to do that, HEK293 cells were grown on 100 mm cell culture dishes and were transfected with either empty EGFP plasmid or mCherry-PYD. Cells were collected and fluorescence intensity of samples were measured. This experiment was done in triplicate. Averages of collected emission spectra can be found in Figure 5.8.

In N_{FRET} calculations, first, two proportionality constants had to be calculated. These are represented by α, the basal fluorescence of mCherry at acceptor emission wavelength when excited at donor excitation wavelength, and β, the basal fluorescence of EGFP at acceptor emission wavelength when excited at donor excitation wavelength. α was calculated by dividing the fluorescence intensity of mCherry at 608 nm when excited at 488 nm to the fluorescence intensity when excited at 588 nm. β was calculated by dividing the fluorescence intensity of EGFP at 608 nm to the one at 508 nm. The calculations can be found in Section 4.4.4.

After these constants are obtained, N_{FRET} calculations allow us to divide an emission spectrum to three separate data sets: one indicating basal EGFP fluorescence, another indicating basal mCherry fluorescence, and the last one indicating fluorescence caused by FRET. An example can be seen in Figure 5.9. The obtained FRET fluorescence is then adjusted according to the total concentration of fluorophores in the system, which are obtained from the emission maximum of EGFP when excited at donor excitation wavelength, and from the emission maximum of mCherry when excited at acceptor excitation wavelength. N_{FRET} is calculated individually for each replicate, and then averaged according to the variant used in the experiment.

Calculated N_{FRET} for PYD variants and their confidence intervals can be found in Figure 5.10. Confidence intervals are obtained by taking the difference between each group means. Confidence intervals show whether two sets of data represent their unique

A

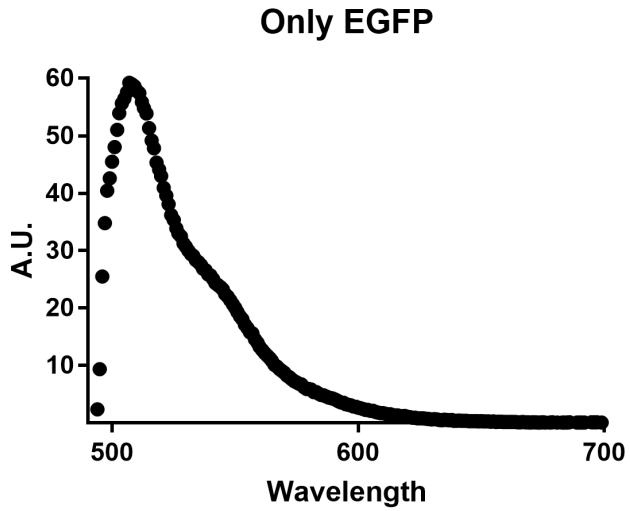

B

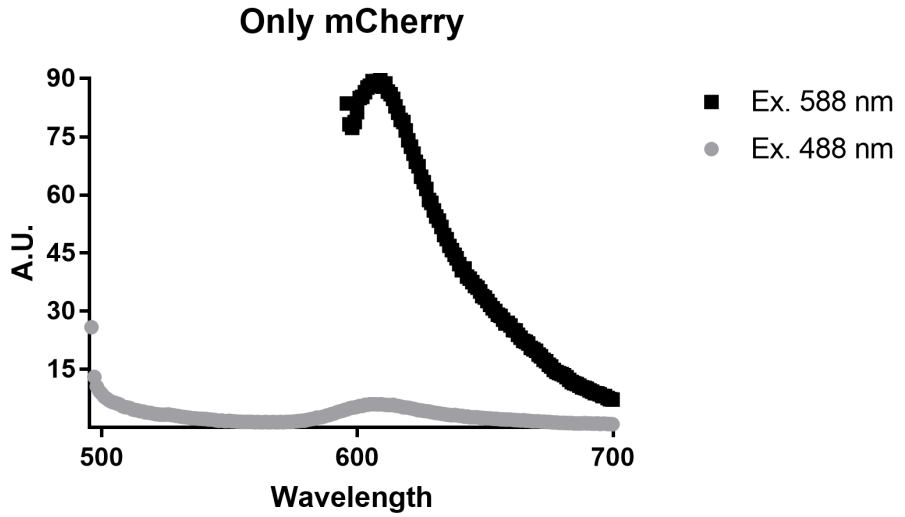

Figure 5.8. Emission spectra of cells expressing (A) EGFP only and (B) mCherry-PYD. Two data sets can be seen in (B), taken when the sample was excited at 488 nm and at 588 nm. The secondary data set for (A) was omitted as EGFP shows no fluorescence when excited at 588 nm.

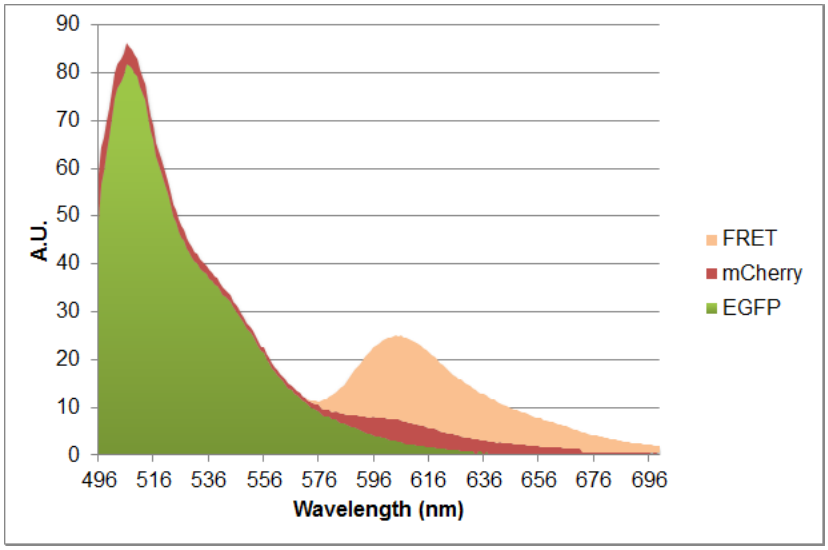

Figure 5.9. Emission spectrum of wildtype CARD fusion proteins, showing N_{FRET} calculations. The basal donor and acceptor fluorescence at donor excitation are calculated and deducted from the graph. The remaining fluorescence intensity at acceptor emission is due to FRET between fluorophores.

phenotype (as in $p \leq 0.05$). The farther away two groups are, the more statistically significant they are. Y60A and L68A mutant variants showed the least FRET activity while some mutant variants, such as L85A, E19A and S29A, showed FRET activity higher than wtPYD. In Figure 5.10, we can see that while E13A, K21A, L25A and T53A had no discernible difference than wtPYD, which is curious as E13A and K21A have been documented to prevent ASC speck formation in full-length ASC. [17] Y60A, and to some extent, L68A and K26A, showed lower FRET efficiency compared to wtPYD. Considering the position of Y60 in PYD, it's possible that it has a significant effect on the orientation of the helices. In Figure 5.6 it can be seen that the majority of PYD-Y60A is mostly in soluble form, while some is still able to contribute to filament formation, thus showing that fluorescence images and FRET results complement each other.

A

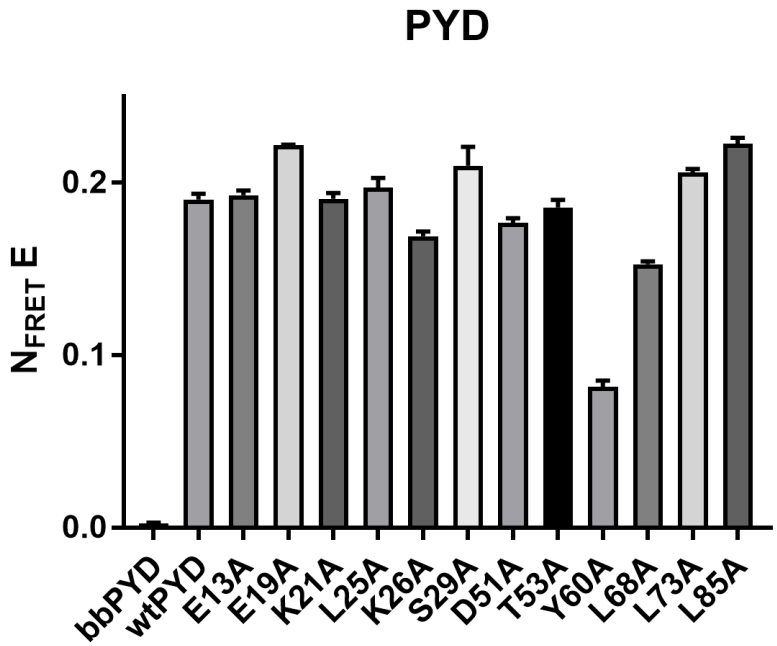

B

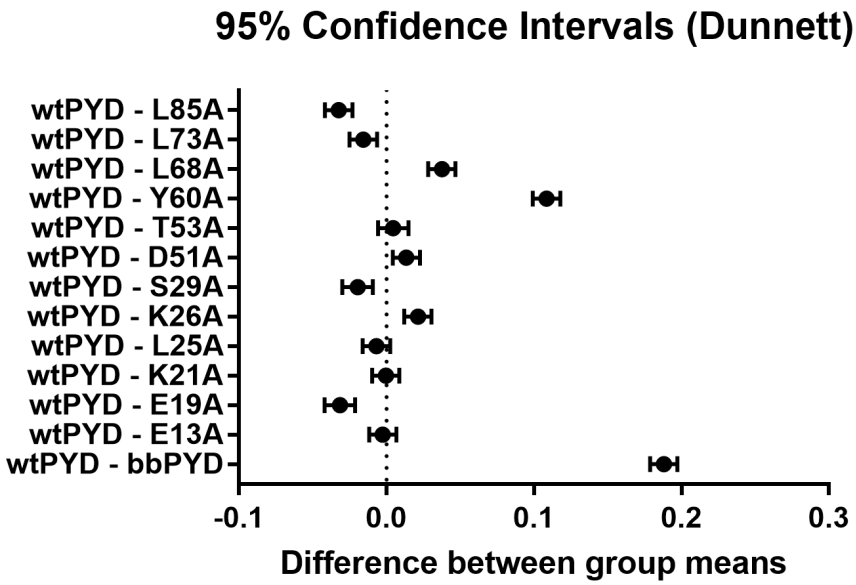

Figure 5.10. (A) N_{FRET} of PYD variants. (B) Confidence intervals of PYD variants. The dotted line represents the N_{FRET} of wildtype PYD fusion proteins. A group is considered to be significant if it the dotted line is not inside its confidence interval. wtPYD is positive control while bbPYD is negative control.

A

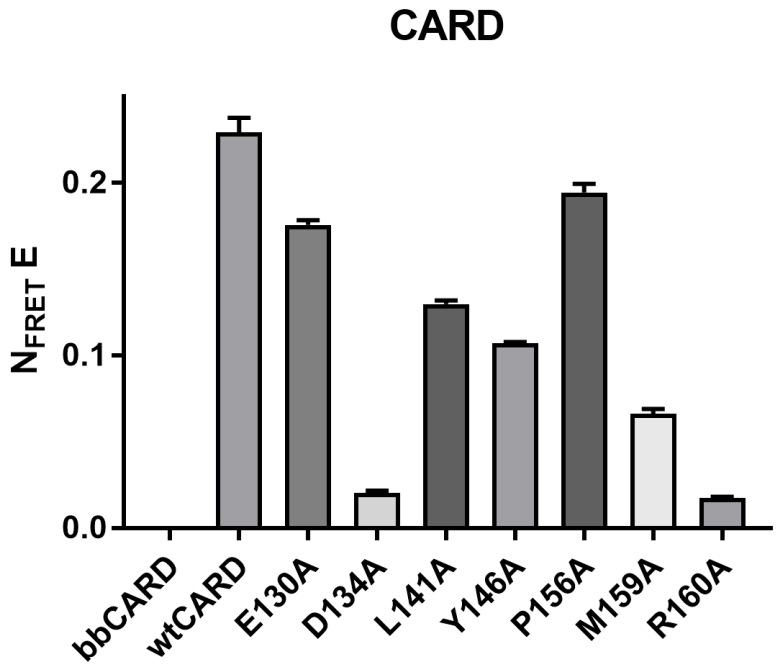

B

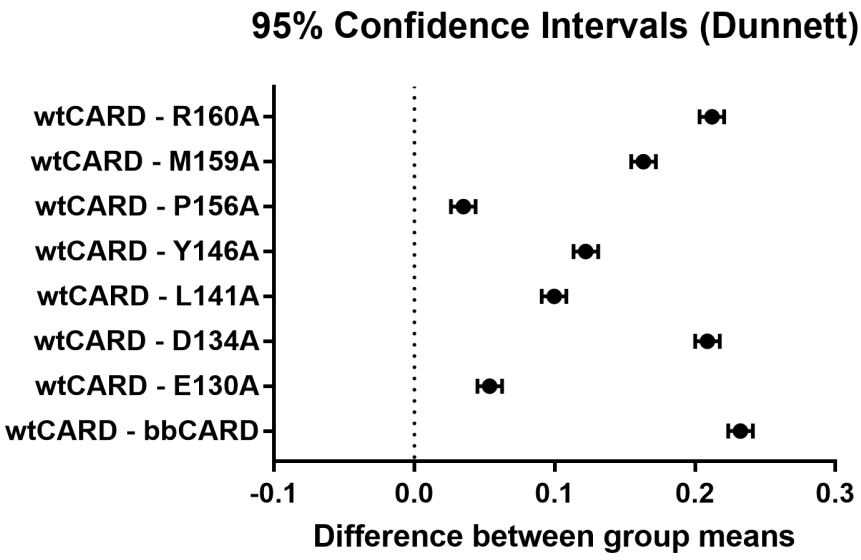

Figure 5.11. (A) N_{FRET} of CARD variants. (B) Confidence intervals of CARD variants. The dotted line represents the N_{FRET} of wildtype CARD fusion proteins. A group is considered to be significant if it the dotted line is not inside its confidence interval. wtPYD is positive control while bbPYD is negative control.

Calculated N_{FRET} for CARD variants and their confidence intervals can be found in Figure 5.11. All mutant variants showed unique N_{FRET} values. D134A and R160A mutants showed almost no FRET activity, meaning that these amino acids are crucial in homotypic CARD interactions. P156A and E130A showed FRET activity close to their wildtype counterpart. Low FRET activity of both M159A and R160A shows that this region is a core part of the interaction surface formed by these residues. Despite being in close proximity, E130A and D134A showed drastically different results, complementing fluorescence microscopy images. It's possible that the negatively charged D134 is the core of another interaction surface.

5.5. Force Spectroscopy of Mutant and Wildtype CARD

In order to understand the forces of interaction and their role in the formation of filaments as well as ASC speck formation, force spectroscopy was selected as the next step. There are many publications on PYD [4], ranging from mutation scanning to NMR imaging, thus an investigation on CARD was thought to be more fruitful. The E130A mutation was selected as the mutant variant in force spectroscopy. Since this mutant variant is still able to bind with its wildtype counterpart (Figure 5.11), it was expected that the conditions listed in Table 5.3 would yield unique results.

Table 5.3. Experiments for atomic force microscopy. The proteins attached to the probe and the surface are indicated.

Exp. #	**Probe**	**Surface**	**# of Locations**
1	His-wtCARD	His-wtCARD	2
2	His-wtCARD	His-CARD-E130A	2
3	His-CARD-E130A	His-CARD-E130A	2
4	His-wtCARD	His-wtCARD	1
5	His-CARD-E130A	His-CARD-E130A	1
6	His-wtCARD	His-CARD-E130A	1

5.5.1. Cloning of CARD into pET30a and Mutant Creation via SDM

Introduction of CARD into pET30a and creation of the E130A mutant variant was done as described in Section 4.2.1. Despite sequential digestion, there were remnants of uncut plasmids in our working solution, and after the ligation step these uncut plasmids could be seen in colony PCR done with pET30a forward and reverse primers. Regardless, this was not an issue; we were able to clone CARD into cut pET30a with a 80% cloning efficiency. Site-directed mutagenesis was then applied on pET30a-CARD to obtain the E130A mutant variant following the procedure described in Section 4.1.3. After checking through sequencing, both plasmids were found to be in working order.

5.5.2. Isolation of His-tagged Wildtype and Mutant CARD After Bacterial Expression

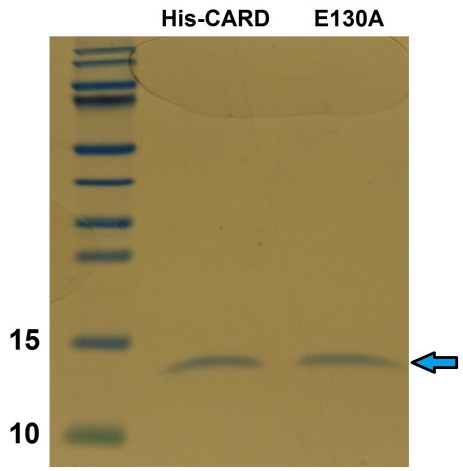

Figure 5.12. SDS-PAGE and Coomassie staining of His-CARD and His-CARD-E130A after affinity purification. The arrow indicates the bands corresponding to the desired protein, which is roughly 13.5 kDa. On the left the bands of the ladder corresponding to 15 and 10 kDa are indicated.

Rosetta pLysS *E.coli* cells were transformed using pET30a-CARD and pET30a-CARD-E130a plasmids. After IPTG induction and affinity column purification, the desired proteins were obtained with near perfect purity (Figure 5.12). The samples shown in Figure 5.12 were eluted from the affinity column using 250 mM elution buffer.

Elutes with higher concentration of imidazole did not yield in any protein while elutes with lower concentration of imidazole harbored many different bands, possibly corresponding to negatively charged bacterial proteins. After concentrating the desired protein as described in Section 4.6.5, the final solute was changed to 1x PBS + 300mM KCl through dialysis.

5.5.3. Atomic Force Microscopy Measurements of Wildtype and Mutant CARD

Purified His-CARD and His-CARD-E130A were collected and used in force spectroscopy as described in Section 4.7. The experiments were done as listed in Table 5.3. wtCARD-wtCARD was designed to be positive control and mutCARD-mutCARD was designed to be negative control. A schematic representation of the experiment can be seen in Figure 5.13. CARD domains are immobilized on the NTA covered surface and on the PEG+NTA covered tip through the 6x His-tag. Because all interaction surfaces were available in wtCARD-wtCARD experiments, the data contained forces of all interaction types. Recordings were collected and put through rough analysis using a MATLAB program. Rough analysis of the data showed a variety of events at every loading rate. The number of perfect and imperfect events observed can be seen in Table 5.4.

Table 5.4. Number of events observed in force spectroscopy. Values show total number of observations done per experiment type. Perfect events and imperfect events are defined in Section 4.7.

	wt-wt	**wt-mut**	**mut-mut**
# of Peaks	6555	8186	6394
# of Perfect Events	485	470	498
# of Imperfect Events	823	726	549
Event Probability	19.95%	14.61%	16.37%

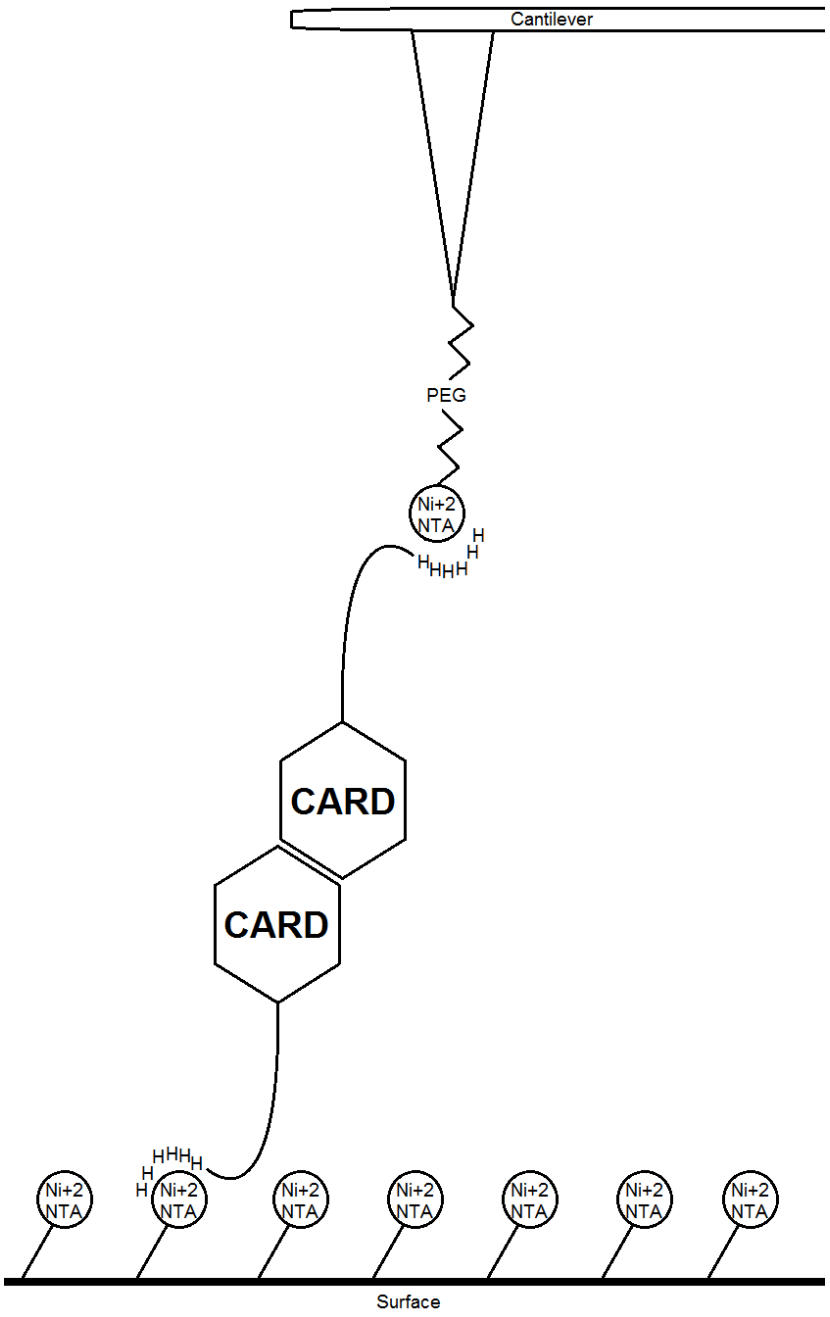

Figure 5.13. Model describing AFM. The proteins bound to the surface and to the cantilever tip will come closer as the cantilever descends. Interaction between surfaces of CARD is expected to cause the cantilever to bend upon ascension.

As expected, wt-wt experiments gave the highest number of events, while experiments involving mutCARD resulted in lower encounter of events. It was not expected for mut-mut experiments to have more events than wt-mut experiments, however, wt-mut experiments had more imperfect events than mut-mut experiments. A selection of perfect events can be seen in Figure 5.14 for wtCARD-wtCARD experiments, Figure 5.15 for wtCARD-mutCARD experiments and Figure 5.16 for mutCARD-mutCARD experiments. Recordings of wtCARD-wtCARD experiments showed a wide variety of forces at work, at different distances from adhesion break point, most likely due to the flexibility of the PEG linker attached to the cantilever tip. In mutCARD-mutCARD experiments, however, the observed events were closer to the adhesion point, and usually had lower strength compared to wtCARD-wtCARD experiments. It's possible that the E130A mutation has a weakening effect on the interaction sites.

Adhesion forces of the homotypic CARD-CARD interactions were extracted from the collected force-distance data. The probabilities of adhesion (defined as the ratio of the number of force curves showing specific unbinding events to the total number of force curves) are shown in Figure 5.17. The obtained adhesion probabilities of each experimental set is in statistically significant range.

The dissociation of wt-wt and mut-mut homotypic CARD interactions exhibits bimodal distribution in the measured loading rate window indicating more than one binding state. The difference in the probabilities of these two mean forces could be associated with relative probabilities of the occurrence of different binding modes as such that one mode has greater fraction compared to the other. This fits in with the idea that there are multiple homotypic interaction types between CARDs.

The dynamic force spectra of the measured forces are shown in Figure 5.18. The mean forces observed in the high-strength state of the bimodal distribution are same at comparable loading rates in wt-wt and mut-mut homotypic CARD interactions, however, the mean forces observed in the low-strength state of mut-mut are lower than the wt-wt CARD interactions at comparable loading rates, indicating that the E130A mutation disrupts the low-strength binding mode observed in wt-wt CARD

interactions and discloses a new binding state. wt-mut CARD interactions exhibit unimodal distribution in the measured loading rate range with two different regimes. The linear regime observed in the lower loading rates is closer to the low-strength state observed in wt-wt CARD unbinding experiments. The second linear relation observed in the higher loading rates is different than all the others, however, the lack of data in this regime makes it difficult to interpret.

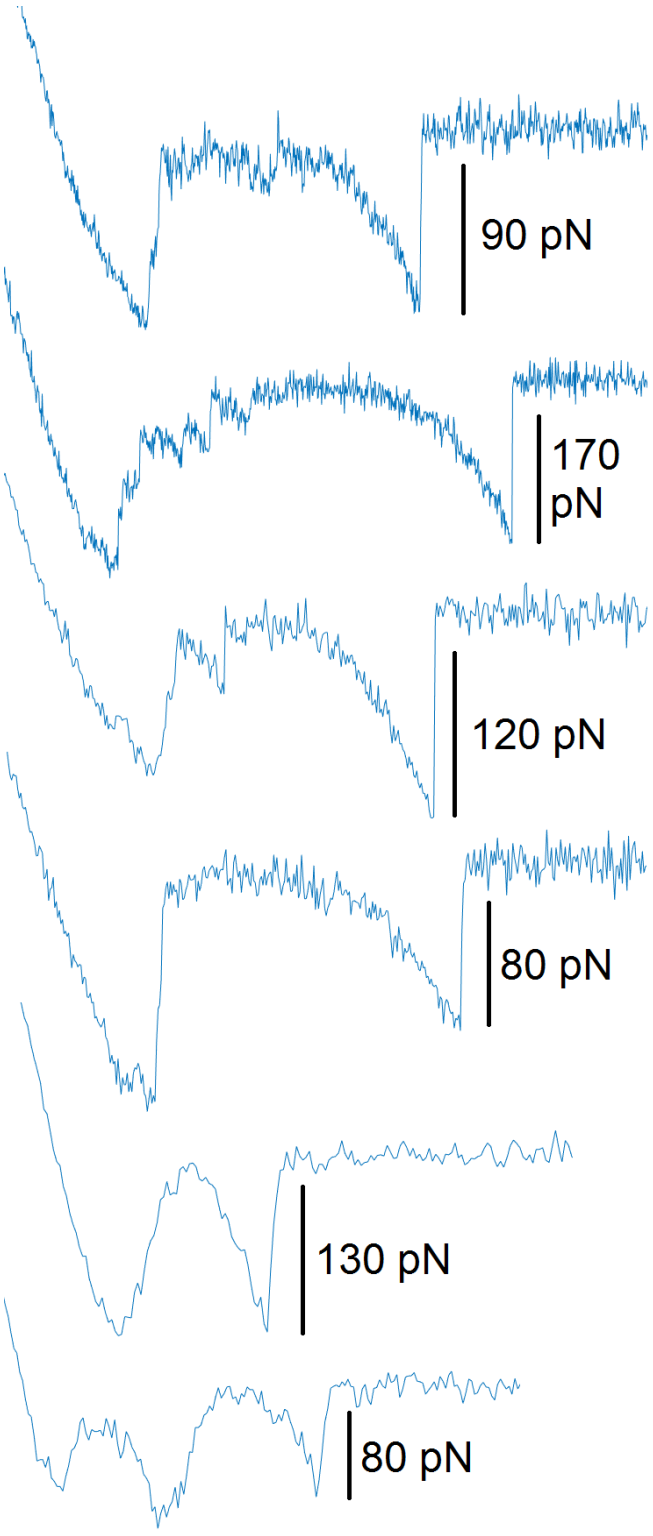

Figure 5.14. AFM data of wtCARD-wtCARD SFMS experiments. Each line graph represents a separate pulling event. Loading rates differ between graphs. Graphs are not up to scale.

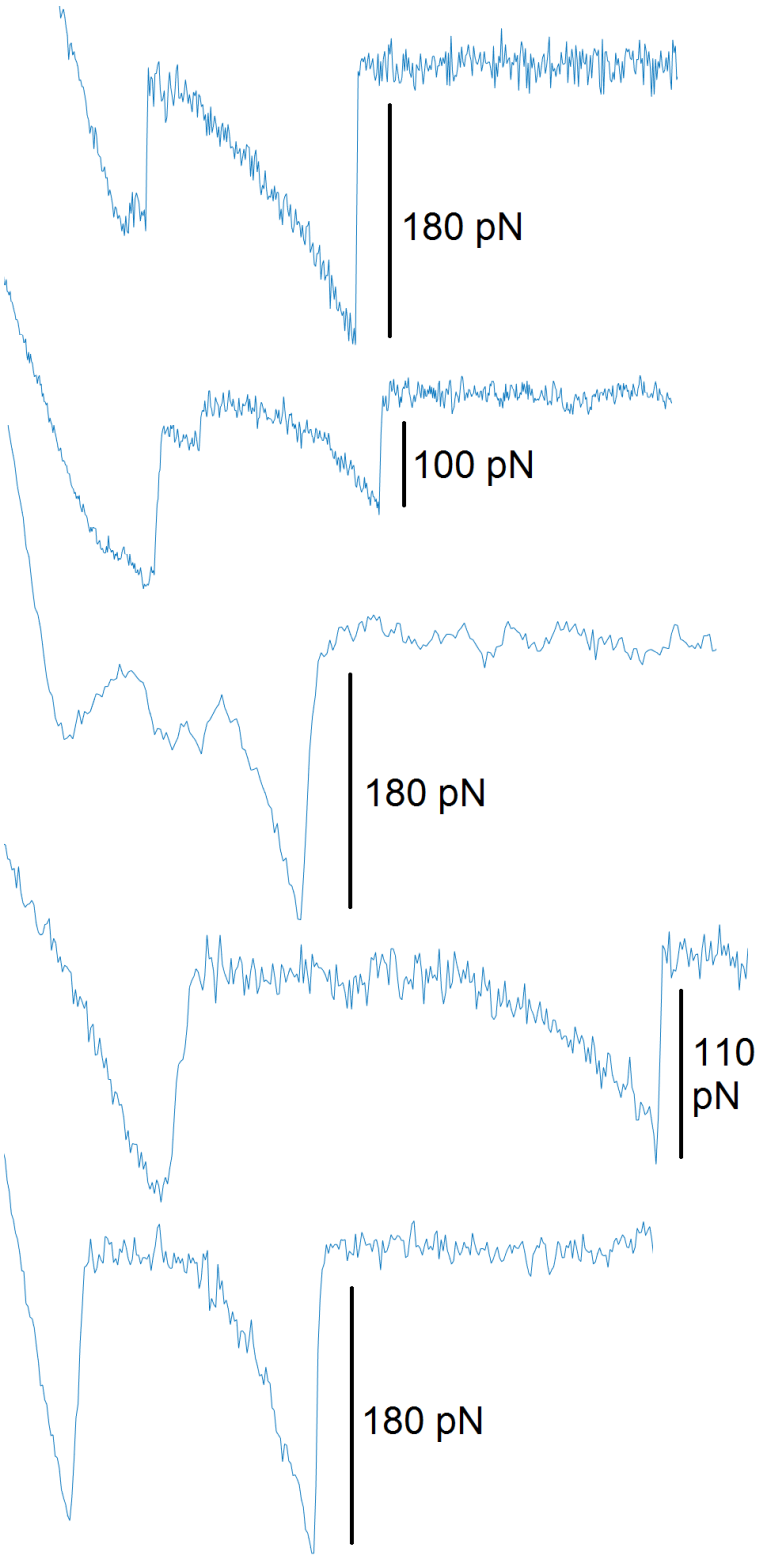

Figure 5.15. AFM data of wtCARD-mutCARD SFMS experiments. Each line graph represents a separate pulling event. Loading rates differ between graphs. Graphs are not up to scale.

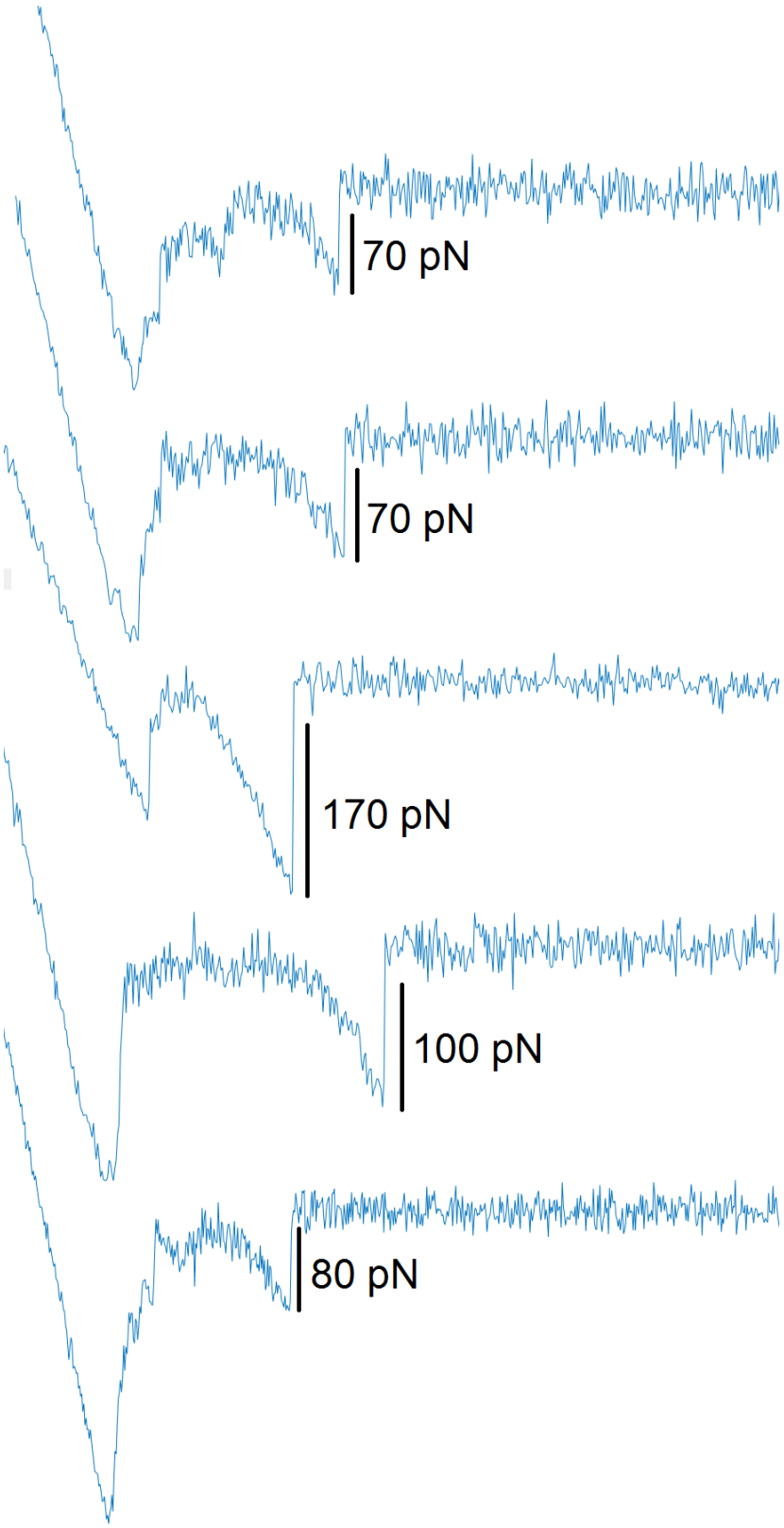

Figure 5.16. AFM data of mutCARD-mutCARD SFMS experiments. Each line graph represents a separate pulling event. Graphs are not up to scale.

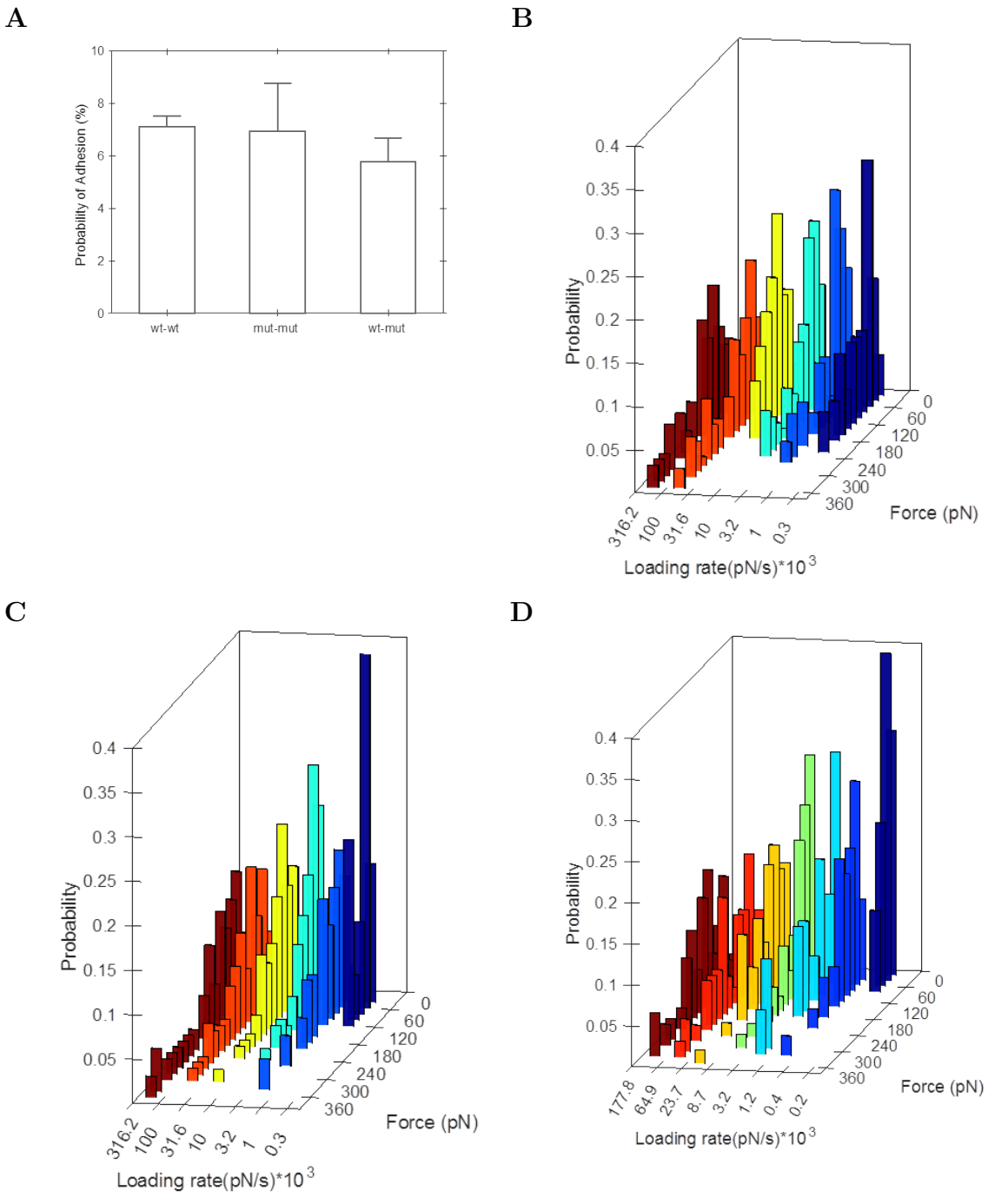

Figure 5.17. Measured probability of adhesion and adhesion forces during dynamic SMFS. (A) Probability of adhesion. (B-D) Adhesion force histograms at different loading rates obtained from pulling experiments at room temperature for (B) wt-wt, (C) mut-mut and (D) wt-mut homotypic CARD interactions.

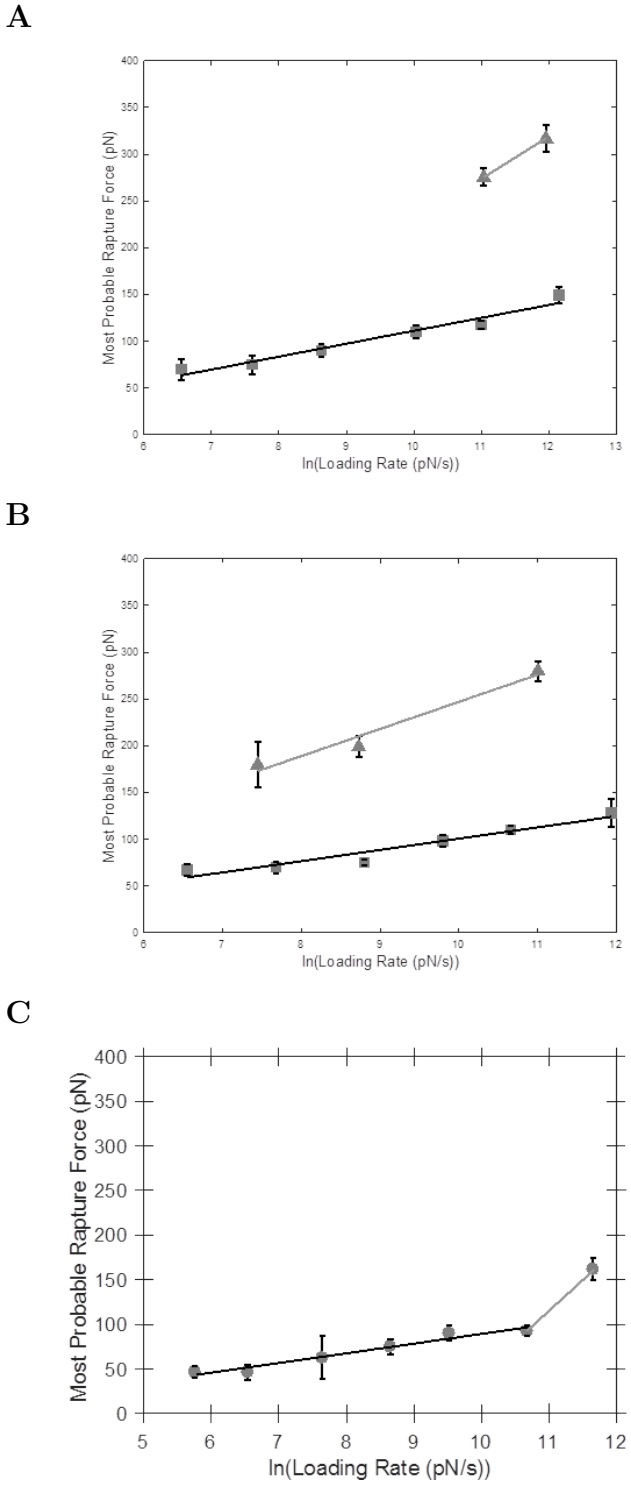

Figure 5.18. Measured most probable rupture forces along the natural logarithm of the measured loading rates for (A) wt-wt, (B) mut-mut and (C) wt-mut conditions. wt-wt and mut-mut CARD dissociation exhibits two different low and high-strength states, while wt-mut CARD dissociation shows a single state.

6. DISCUSSION

In the present study, we've tried to develop a quantitative analytical method for type I, type II and type III interactions of DDs, focusing on ASC and its PYD and CARD domains. We have demonstrated that mutations such as E13A, E19A, K21A, that are known for preventing ASC speck formation retained their ability to contribute to the formation of filaments under the presence of wildtype PYD. We have checked four novel mutations on PYD, namely S29A, T53A, Y60A and L85A, and among these Y60A showed a distinct difference in FRET efficiency compared to other variants, marking it as an important amino acid in homotypic PYD interactions. Due to the lack of CARD domain related studies, we have focused on CARD. We have designed and observed the effects of five novel mutations on CARD; E130A, D134A, L141A, Y146A and P156A, all amino acids known to be important in CARD structure. We have shown the lack of homooligomerization in mutations D134A, M159A and R160A through fluorescence microscopy and FRET analysis. Mutant CARD variants E130A and P156A showed phenotypes similar to wtCARD, yet different enough to be considered separately. From these CARD variants, we have focused on the E130A mutation, deemed as important in CARD oligomerization in other studies [43] and done force spectroscopy through atomic force microscopy to further investigate the interaction types of CARD and their importance.

6.1. FRET Results

PYD mutants such as K26A, K21A and E13A showed FRET activity similar to wildtype PYD. These mutations have been documented to prevent complete homooligomerization in ASC [17]. It is highly possible that these mutant variants are only partially able to form secondary structures, maybe a few short oligomers due to disruption at type I interaction site primarily, but along with their wildtype counterpart, they're able to contribute to the filament formation, and the weak type I surface is able to bond with other PYDs using the helical rise and other wildtype PYD molecules as a scaffold.

The lowest FRET activity was seen in the PYD Y60A mutant. This amino acid, while not described as having an integral part in the interaction surfaces of PYD, due to its placement on the loop between helices 4 and 5, might have an important effect on type II interaction. Being in patch IIa, it's possible that this residue plays an integral role in maintaining patch IIa, even if it may not be involved in the acting non-covalent bonds between patch IIa and patch IIb. It's possible that the Y60A mutation causes a conformational change in PYD, or changing the position of helices 4 and 5 or the loop between them, disrupting patch IIa and thus type II interaction surface.

Some PYD mutants such as L85A, S29A and E19A showed a higher FRET efficiency compared to their wildtype counterpart. Theoretically, it was expected that EGFP-PYD and mCherry-PYD would co-localize on the same filaments, however, it is not guaranteed that the filament will be made up of alternating EGFP-PYD and mCherry-PYD. Patches of EGFP-PYD or mCherry-PYD clumped together, thus not participating in FRET is also a distinct possibility. This means that there are three types of possible interactions between fusion proteins: among EGFP-PYD, among mCherry-PYD, or between EGFP-PYD and mCherry-PYD. Some mutant variants might have lost the ability to bind among themselves, but retain the ability to form bonds with the wildtype variant. This eliminates the interaction among EGFP-PYD mutant variants, being able to form bonds only with the wildtype variant, thus wholly contributing to FRET. It was stated that the filament formation uses all available PYD molecules within the cell, meaning that if all mutant EGFP-PYD binds with wildtype mCherry-PYD, it'll result in a higher FRET signal. It's possible that this happens in a dose dependent manner, and when all the wildtype PYD is in the formed filaments, the remaining mutant PYD (if not wholly used already) can't propagate the filament further, since it can't bind to other mutant PYDs, and it remains in the cell as a soluble protein. A schematic representation of this feature can be seen in Figure 6.1. In this figure, the representative figures are explained as follows: (A) When the wildtype variant is present, the three-step helical rise begins to form. Mutant variants are able to contribute to the filament, as the wildtype variant can still bind to mutant variant through the remaining 5 unmodified patches. (B) When only the mutant variant is present, the presence of the mutation disables an entire interaction type, thus the he-

lical structure cannot form. (C) Mutation may cause a conformational change in the structure of the death domain, changing the interaction surfaces and preventing the molecule from contributing to the helical rise.

CARD mutants showed a wider variety of FRET E compared to PYD mutants. It's been shown that homotypic interactions between CARD groups are weaker compared to PYD groups [4], which might explain why mutations affect CARD more than PYD, and contribute to the fact that the main force in ASC polymerization is the formation of PYD filaments. It is possible that the mutations investigated here were coincidentally significant amino acids, but some amino acids investigated in this thesis were studied before [17, 43], and were shown to disrupt ASC speck formation. Nevertheless, it should be noted that there are no documented studies on the effect of these single amino acid mutations on ASC-CARD alone. These findings not only show that domains belonging to the death-fold superfamily different bonds at work in the formation of higher order structures, but are also considered novel as there are only limited studies on the dynamics of CARD.

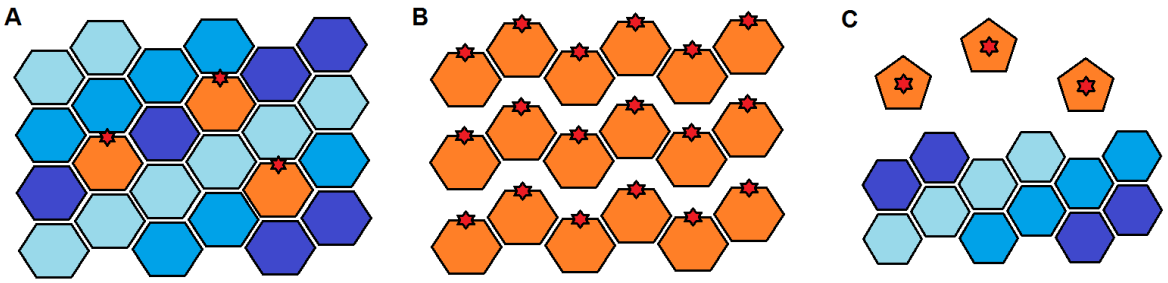

Figure 6.1. Possible structural formations based on the results of this study. Each hexagon represents an individual PYD/CARD molecule.

N_{FRET} results for CARD mutant variants D134A and R160A are very close to bbCARD. These mutations are found to be significant, and considering the position of these amino acids in the structure of CARD, it might be said that these amino acids are the primary contributors of type I interaction in CARD. Most likely, R160 fits into the groove of D134, making up type I interaction. R160A and M159A showed similar FRET E, meaning that this region is highly important in maintaining homotypic interactions

between domains. E130A and P156 CARD mutant variants showed FRET E close to their wildtype counterpart, but confidence intervals revealed that their FRET E is different enough to have their own phenotype. Indeed, while E130A could be seen to contribute to the formation of filaments, fluorescence microscopy showed cells in which it remained as a soluble monomer. Considering E130A and D134A are on the same helix and their side chain contributes to the interaction interface, it was expected that both mutations would yield a similar result. Most likely, D134 is at the core of an interaction interface while the negative charge on E130 is more like a supporting residue, that guides the interacting surfaces to be in the correct orientation, but is not necessarily required.

The filament formation occurs in an all-or-nothing fashion. Confocal and fluorescence images of wildtype fusion proteins showed almost no background fluorescence, indicating that most, if not all, of fusion proteins contributed to filament formation. Interestingly, in mutant variants, background fluorescence could be seen. Considering the cylindrical form of the filaments, it's possible that the mutant variants can only contribute to the filament once they're surrounded by the wildtype domain, as this way only one surface of the domain will be dysfunctional, however, when an interaction type is blocked completely - between opposite surfaces of mutant variants, the filament formation cannot occur. This would contribute to the fact that all interaction types are necessary in order for the filaments to form.

Observing similar FRET efficiencies between wildtype variants and certain mutant variants show that some of these mutations can be rescued if paired with a wildtype variant, meaning that any immune system deficiencies that are a result of genetic ASC mutations need to be homozygous. Of course, the effects of these mutations on the inflammation signaling pathways were not investigated in thus study, further investigation is necessary before reaching a conclusion. It's also important to say that overexpression of ASC domains - especially CARD - may have led to pyroptotic cell death, which theoretically shouldn't, but still might affect FRET results. In some experiments, floating dead cells could be seen in cell culture dishes prior to collection. If overexpression of these proteins lead to pyroptosis, time-lapse observations might need

to be done to observe how cells respond to co-transfection, as well as overexpression of ASC domains.

To obtain better results, more replicates could be used in measuring FRET efficiency, but as it can be seen in Figure 5.10 and Figure 5.11, N_{FRET} results are highly consistent. It's important to keep in mind that it wasn't always possible to get equal molar ratios of both fusion proteins even though similar plasmid amounts were used in transfection experiments, however, the measured emission spectra between the experimental replicates were highly consistent. It cannot be said that each replicate gave the exact same value as the others, but the trends of the emission spectra remained the same within each group, meaning that this method accurately represents the binding efficiency of wildtype or mutant CARD or PYD variants. To ensure further accuracy, it might be wise to make dose-dependent experiments on select mutant variants to observe how much of their capability to form filaments is tied to their wildtype counterpart.

6.2. AFM Results

To date, there is no documented force spectroscopy experiments on the binding strengths of type I, type II and type III interaction surfaces of ASC or any of the death domains. Our force spectroscopy results are novel in this field. We have selected to look at the effect of E130A mutation as a mutation on this residue was shown to prevent ASC speck formation [43], while our results showed its ability to form filamentous structures with wildtype CARD. So it was expected that the three experiments we have designed, wtCARD-wtCARD as positive control, mutCARD-mutCARD as negative control, and wtCARD-mutCARD as experimental set, would show unique force spectroscopy results due to their properties.

It was expected that the event count would be the highest for wtCARD-wtCARD, and indeed event probability was highest for wtCARD-wtCARD among the experimental groups, yet events could be observed in each experimental condition, and at most loading rates, if not all. It was not expected that mutCARD-mutCARD would yield

a considerable amount of events. It's possible that despite the change E130A puts on CARD, the interaction surfaces were still able to interact with other CARD proteins. The E130A mutation is on the second alpha helix of CARD, close to the loop between helices 1 and 2, and facing outward, as shown in figure 6.2. The E→A mutation may affect patch Ib directly, and patch IIIa due to its proximity, yet it's not at the center of both patches. Our data showed that in presence of wtCARD, CARD-E130A is able to participate in FRET, meaning that the mutation's disruptive capabilities is limited.

It's a possibility that despite the mutation, wtCARD may still form interaction bonds with CARD-E130A as if it was a wildtype protein. If this is the case, then it can be said that the reason behind the E130A mutation showing a lack of filament formation is not because of its interruption of interaction surfaces, but causing a change in protein folding, and leading to a protein that's still capable of making oligomeric structures, but not the three-strand helical filament. Regardless, the AFM data should be investigated more thoroughly by someone who's more knowledgeable and has more experience working with SMFS before reaching any conclusions. Functionalization protocol of the molecules to both tip and surfaces should be optimized and control experiments should be performed to make sure that the observed unbinding processes belong to the specific CARD-CARD interactions.

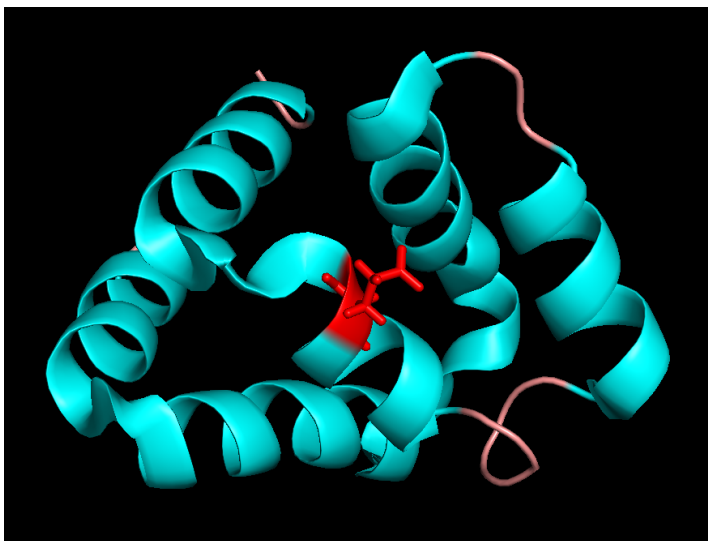

Figure 6.2. Position of the 130th amino acid on CARD (based on 2KN6 [3]).

6.3. Technical Discussion

Despite the differences in size, EGFP and mCherry fluorophores don't act as obstacles to PYD-PYD or CARD-CARD filament formation. In the most probable case, the fluorophores are oriented towards the outside of the formed filament, and due to the tight organization of the structure, the fluorophores are able to be in close proximity, as well as in correct orientation. The EGFP in the fusion proteins is able to form weak dimers through homotypic interactions, yet negative control experiments showed that this interaction is not significant enough to cause premature FRET. While EGFP and mCherry can be seen with eye through a fluorescence microscope, mCherry is one of the least bright fluorophores there are, and the equipment used to measure mCherry intensity was not always able to detect pure signals. The spectrofluorometer sometimes measured mCherry intensity considerably lower compared to EGFP intensity, despite both fluorophores theoretically being in similar molar ratios, however, seFRET could still be detected even at low intensities. Nevertheless, the EGFP-mCherry FRET pair is known for low crosstalk and bleedthrough in measurements, and as a result, FRET occurrence could be seen even during intensity measurements. For FRET experiments of this type, FP pairs with a higher acceptor brightness may be preferred, like mNeonGreen and mRuby3.

Following the protocols used in this thesis, apFRET was problematic at best. While apFRET is not recommended for experiments where molar ratios of FPs are not equal, it was attempted as apFRET is one of the most common and widely accepted methods of measuring FRET. Despite washing the cover slips and using only a small amount of mounting medium, cells were distributed in the 40 μm space between the cover slip and the microscope slide. It's unknown whether it was because of the cells floating in the medium, or the change in the deflection of light as the ddH_2O between the cover slip and the objective lens evaporated, but focusing on a single cell was more difficult than it should have been. With the closest laser source to excite mCherry being at 544 nm (which is considerably less effective at exciting mCherry than 588 nm), complete photobleaching took almost half an hour to do. During this time, the focused cell could be seen as slightly moving in the three dimensional space, almost in every

attempt. This was not significantly important for photobleaching - as the cells were still subjected to the highly focused laser beam, however, getting comparative images for EGFP fluorescence was nigh impossible. To make accurate exclamations regarding the increase in donor fluorescence, the sample should be exactly still so that the intensity between two images will be comparable. Regardless, apFRET was observable, albeit the increase of EGFP fluorescence intensity was not exactly consistent between samples, with observed intensity increase ranging from 1.3-fold to 1.7-fold.

The measured emission spectra of samples were highly consistent between experimental replicates, however, between experimental groups variations could be observed. Whether this has an impact on the N_{FRET} calculations is dubitable, as previous experiments (data not shown) showed similar trends with the data presented here. Replicates of samples were preferred instead of taking replicate measurements. Duplicate measurements were tested as well, however, the variance between obtained data sets were too insignificant to be considered, thus all measurements were taken once. This method of measuring seFRET is stable, consistent, easy and quick. It was also observed that cells collected this way are able to show fluorescence and FRET activity for up to two weeks. Different methods for sample collection and preparation were also tested, including cell scraping, sonication and fixation. It was observed that cell lysis or protein fixation were not necessary; in fact, measuring cells collected by trypsinization directly with no additional treatments gave the best results. Including fixation agents in the solution lowered total fluorescence, and disrupting cells via sonication resulted in lower FRET signals. It's possible that the filaments consisting of ASC domains instead of full-length ASC are less durable against disruptive forces, and sonication dissociates FPs from each other, resulting in a lower signal.

Protein production of His-CARD and His-CARD-E130A was straightforward, though sample purification had some pitfalls. Despite repeated sonication attempts, the protein couldn't be completely recovered from the bacterial pellet. The recovered amount was more than enough for AFM experiments, so this issue wasn't considered as important at the time, and it wasn't investigated why CARD stayed in the pellet, but it's possible to make educated guesses regarding the issue. The most likely reason

is that due to the overexpression of the protein in bacteria, CARD molecules formed filaments, aggregated and centrifugation caused them to remain in the pellet. If this is the case, the sonication step may not be long or intense enough to ensure filament disruption. There's no sure way to say whether filament formation actually occurred, since it's not known if the protein actually folded correctly as if in a mammalian cell, however, due to the compact shape and length of the protein, it should show the same properties. pET30a contains a solubility tag after His-tag to increase solubility of expressed proteins, but in this case it might have been ineffective. Using 300 mM KCl in the main liquid culture might be attempted next time to observe if the destabilizing effect of KCl on ASC helps on blocking CARD filament formation. At the very least, the addition of KCl allowed us to recover part of the protein. Another possibility is that the sonication step was not enough for disrupting bacterial membrane. Lysis buffers may be preferred in the future, though this is discouraged as the presence of lysis buffers may denature CARD or disrupt its properties in a non-recoverable manner.

It's possible that the experimental design presented in this thesis brought certain limitations. The pET30a plasmid contains a 6x His-tag followed by a solubility tag consisting of 15 amino acids. It contains a thrombin cutting site between the two tags, and an enterokinase cutting site after the solubility tag. Using BglII as the forward restriction site, the enterokinase cutting site was removed and CARD sequence began 2 amino acids after the solubility tag. If the solubility tag has a secondary structure, it might interfere with CARD's own structure, thus it would've been more feasible to clone CARD further down from the solubility tag. Additionally, while the 6x His-tag is very useful in affinity chromatography, it is not a particularly strong tag. In some AFM recordings, events with a forces larger than 150 pN were observed. This force is more or less the maximum force His-tag can bear before its bind with the NTA group breaks. [46] It's possible that the CARD on the tip made non-covalent bonds with multiple CARD molecules on the surface, and their combined strength overpowered the strength of His-tag. Another possibility is that at faster loading rates the sheer force of pulling overpowered His-tag and caused His-CARD to break away from the surface or the cantilever tip. Considering the compact shape and length of CARD, and considering that the homotypic death domain interactions do not cause a

significant conformational change, homotypic CARD interactions shouldn't be able to break His-tag from its anchor. Unfortunately it's impossible to compare results and methodology as this type of experiment was never conducted before. A stronger tag like biotin-streptavidin may be preferred in future experiments to observe if there are indeed events with higher forces.

It's important to say that there has been a documented research that used His-tag and AFM to measure homotypic interactions [47], thus AFM can still be considered as a valid tool in measuring homotypic interactions [48], however, while the experiment itself is fairly straightforward, the time and effort dedicated to analyzing the data isn't economical. Additionally, the cost of the equipment used in AFM, as well as the fact that the probes and surfaces can be used only once, makes this technique more suitable to applications that would give trustworthy results, like investigating polytopic transmembrane proteins. Maybe with more powerful tools - especially computational - and more hands-on experience in this technique, this method would be more feasible.

6.4. Conclusion

Proteins with death domains are capable of forming oligomeric structures. [15,16] In this thesis, we have investigated the polymerization dynamics of PYD and CARD, two conserved death domains of ASC. Combining with our well-defined protocols, we have enhanced the use of FRET and ensured consistent results that can be used to make solid inferences. We have studied the effects of 12 PYD and 7 CARD mutations on their homooligomerization capabilities. Through FRET and fluorescence microscopy, we have shown that mutant variants such as E13A, K21A and K26A, known for their disruption of ASC speck formation, do not entirely lose their binding capabilities, and that most likely the formation of higher order structures are due to the combined presence of all types of death domain interactions as well as due to the specific conformation of the death domain. We have observed that amino acid mutations have a bigger impact on CARD oligomerization compared to PYD, which coincide with the fact that homotypic CARD interactions are weaker compared to PYD. [4] In order to better understand the forces of interaction acting between death domains, we have

used wildtype CARD and its E130A mutant variant in force spectroscopy, and measured the acting forces between CARD molecules. Through this thesis, we hope to give an insight to the oligomerization dynamics of death domains.

REFERENCES

1. Bauernfeind, F. and V. Hornung, "Of inflammasomes and pathogens - sensing of microbes by the inflammasome", *EMBO Molecular Medicine*, Vol. 5, No. 6, pp. 814–826, June 2013.

2. Kersse, K., J. Verspurten, T. V. Berghe and P. Vandenabeele, "The death-fold superfamily of homotypic interaction motifs", *Trends in Biochemical Sciences*, Vol. 36, No. 10, pp. 541–552, October 2011.

3. de Alba, E., "Structure and Interdomain Dynamics of Apoptosis-associated Speck-like Protein Containing a CARD (ASC)", *Journal of Biological Chemistry*, Vol. 284, No. 47, pp. 32932–32941, November 2009.

4. Hoss, F., J. F. Rodriguez-Alcazar and E. Latz, "Assembly and regulation of ASC specks", *Cellular and Molecular Life Sciences*, pp. 1–19, October 2016.

5. Bajar, B., E. Wang, S. Zhang, M. Lin and J. Chu, "A Guide to Fluorescent Protein FRET Pairs", *Sensors*, Vol. 16, No. 9, p. 1488, September 2016.

6. Whited, A. M. and P. S.-H. Park, "Atomic force microscopy: A multifaceted tool to study membrane proteins and their interactions with ligands", *Biochimica et Biophysica Acta (BBA) - Biomembranes*, Vol. 1838, No. 1, pp. 56–68, January 2014.

7. Parkin, J. and B. Cohen, "An overview of the immune system", *The Lancet*, Vol. 357, No. 9270, pp. 1777–1789, June 2001.

8. Mackay, I. R., F. S. Rosen, P. J. Delves and I. M. Roitt, "The Immune System", *New England Journal of Medicine*, Vol. 343, No. 1, pp. 37–49, July 2000.

9. Mackay, I. R., F. S. Rosen, P. J. Delves and I. M. Roitt, "The Immune System", *New England Journal of Medicine*, Vol. 343, No. 2, pp. 108–117, July 2000.

10. Elliott, D. E., S. S. Siddique and J. V. Weinstock, "Innate Immunity in Disease", *Clinical Gastroenterology and Hepatology*, Vol. 12, No. 5, pp. 749–755, May 2014.

11. Cui, J., Y. Chen, H. Y. Wang and R.-F. Wang, "Mechanisms and pathways of innate immune activation and regulation in health and cancer", *Human Vaccines & Immunotherapeutics*, Vol. 10, No. 11, pp. 3270–3285, November 2014.

12. Meylan, E., J. Tschopp and M. Karin, "Intracellular pattern recognition receptors in the host response", *Nature*, Vol. 442, No. 7098, pp. 39–44, July 2006.

13. Elinav, E., T. Strowig, J. Henao-Mejia and R. A. Flavell, "Regulation of the Antimicrobial Response by NLR Proteins", *Immunity*, Vol. 34, No. 5, pp. 665–679, May 2011.

14. Hauenstein, A. V., L. Zhang and H. Wu, "The hierarchical structural architecture of inflammasomes, supramolecular inflammatory machines", *Current Opinion in Structural Biology*, Vol. 31, No. 4, pp. 75–83, April 2015.

15. Hughes, M. A., I. R. Powley, R. Jukes-Jones, S. Horn, M. Feoktistova, L. Fairall, J. W. Schwabe, M. Leverkus, K. Cain and M. MacFarlane, "Co-operative and Hierarchical Binding of c-FLIP and Caspase-8: A Unified Model Defines How c-FLIP Isoforms Differentially Control Cell Fate", *Molecular Cell*, Vol. 61, No. 6, pp. 834–849, March 2016.

16. Janssens, S. and A. Tinel, "The PIDDosome, DNA-damage-induced apoptosis and beyond", *Cell Death and Differentiation*, Vol. 19, No. 1, pp. 13–20, January 2012.

17. Sahillioglu, A. C., F. Sumbul, N. Ozoren and T. Haliloglu, "Structural and Dynamics Aspects of ASC Speck Assembly", *Structure*, Vol. 22, No. 12, pp. 1722–1734, December 2014.

18. Sborgi, L., F. Ravotti, V. P. Dandey, M. S. Dick, A. Mazur, S. Reckel, M. Chami, S. Scherer, M. Huber, A. Böckmann, E. H. Egelman, H. Stahlberg, P. Broz, B. H. Meier and S. Hiller, "Structure and assembly of the mouse ASC inflammasome by combined NMR spectroscopy and cryo-electron microscopy", *Proceedings of the National Academy of Sciences*, Vol. 112, No. 43, pp. 13237–13242, October 2015.

19. Cai, X., J. Chen, H. Xu, S. Liu, Q.-X. Jiang, R. Halfmann and Z. J. Chen, "Prion-like Polymerization Underlies Signal Transduction in Antiviral Immune Defense and Inflammasome Activation", *Cell*, Vol. 156, No. 6, pp. 1207–1222, March 2014.

20. Liepinsh, E., R. Barbals, E. Dahl, A. Sharipo, E. Staub and G. Otting, "The Death-domain Fold of the ASC PYRIN Domain, Presenting a Basis for PYRIN/PYRIN Recognition", *Journal of Molecular Biology*, Vol. 332, No. 5, pp. 1155–1163, October 2003.

21. Lu, A., V. G. Magupalli, J. Ruan, Q. Yin, M. K. Atianand, M. R. Vos, G. F. Schröder, K. A. Fitzgerald, H. Wu and E. H. Egelman, "Unified Polymerization Mechanism for the Assembly of ASC-Dependent Inflammasomes", *Cell*, Vol. 156, No. 6, pp. 1193–1206, March 2014.

22. Richards, N., P. Schaner, A. Diaz, J. Stuckey, E. Shelden, A. Wadhwa and D. L. Gumucio, "Interaction between Pyrin and the Apoptotic Speck Protein (ASC) Modulates ASC-induced Apoptosis", *Journal of Biological Chemistry*, Vol. 276, No. 42, pp. 39320–39329, October 2001.

23. Schmidt, F. I., A. Lu, J. W. Chen, J. Ruan, C. Tang, H. Wu and H. L. Ploegh, "A single domain antibody fragment that recognizes the adaptor ASC defines the role of ASC domains in inflammasome assembly", *The Journal of Experimental Medicine*, Vol. 213, No. 5, pp. 771–790, May 2016.

24. Fernandes-Alnemri, T., J. Wu, J.-W. Yu, P. Datta, B. Miller, W. Jankowski, S. Rosenberg, J. Zhang and E. S. Alnemri, "The pyroptosome: a supramolecular assembly of ASC dimers mediating inflammatory cell death via caspase-1 activation", *Cell Death and Differentiation*, Vol. 14, No. 9, pp. 1590–1604, September 2007.

25. Sahillioğlu, A. C. and N. Özören, "Artificial Loading of ASC Specks with Cytosolic Antigens", *PLOS ONE*, Vol. 10, No. 8, p. e0134912, August 2015.

26. Yaşa, S., *In Vivo Studies of ASC Specks as Antigen Delivery Vehicles*, Ms thesis, Boğaziçi University, 2017.

27. Forster, T., "Energiewanderung und Fluoreszenz", *Die Naturwissenschaften*, Vol. 33, No. 6, pp. 166–175, 1946.

28. Miyawaki, A., "Development of Probes for Cellular Functions Using Fluorescent Proteins and Fluorescence Resonance Energy Transfer", *Annual Review of Biochemistry*, Vol. 80, No. 1, pp. 357–373, July 2011.

29. Zaccolo, M., "Use of Chimeric Fluorescent Proteins and Fluorescence Resonance Energy Transfer to Monitor Cellular Responses", *Circulation Research*, Vol. 94, No. 7, pp. 866–873, April 2004.

30. Zeug, A., A. Woehler, E. Neher and E. G. Ponimaskin, "Quantitative Intensity-Based FRET Approaches—A Comparative Snapshot", *Biophysical Journal*, Vol. 103, No. 9, pp. 1821–1827, November 2012.

31. Hoppe, A., K. Christensen and J. A. Swanson, "Fluorescence Resonance Energy Transfer-Based Stoichiometry in Living Cells", *Biophysical Journal*, Vol. 83, No. 6, pp. 3652–3664, December 2002.

32. Lam, A. J., F. St-Pierre, Y. Gong, J. D. Marshall, P. J. Cranfill, M. A. Baird, M. R. McKeown, J. Wiedenmann, M. W. Davidson, M. J. Schnitzer, R. Y. Tsien and M. Z. Lin, "Improving FRET dynamic range with bright green and red fluorescent proteins", *Nature Methods*, Vol. 9, No. 10, pp. 1005–1012, September 2012.

33. Binnig, G., C. F. Quate and C. Gerber, "Atomic Force Microscope", *Physical Review Letters*, Vol. 56, No. 9, pp. 930–933, March 1986.

34. Binnig, G., H. Rohrer, C. Gerber and E. Weibel, "Tunneling through a controllable vacuum gap", *Applied Physics Letters*, Vol. 40, No. 2, pp. 178–180, January 1982.

35. Zhong, Q., D. Inniss, K. Kjoller and V. Elings, "Fractured polymer/silica fiber surface studied by tapping mode atomic force microscopy", *Surface Science*, Vol. 290, No. 1-2, pp. L688–L692, June 1993.

36. Fechner, P., T. Boudier, S. Mangenot, S. Jaroslawski, J. N. Sturgis and S. Scheuring, "Structural Information, Resolution, and Noise in High-Resolution Atomic Force Microscopy Topographs", *Biophysical Journal*, Vol. 96, No. 9, pp. 3822–3831, May 2009.

37. Noy, A., "Force spectroscopy 101: how to design, perform, and analyze an AFM-based single molecule force spectroscopy experiment", *Current Opinion in Chemical Biology*, Vol. 15, No. 5, pp. 710–718, October 2011.

38. Evans, E., "Probing the Relation Between Force—Lifetime—and Chemistry in Single Molecular Bonds", *Annual Review of Biophysics and Biomolecular Structure*, Vol. 30, No. 1, pp. 105–128, June 2001.

39. Kedrov, A., H. Janovjak, K. T. Sapra and D. J. Müller, "Deciphering Molecular Interactions of Native Membrane Proteins by Single-Molecule Force Spectroscopy", *Annual Review of Biophysics and Biomolecular Structure*, Vol. 36, No. 1, pp. 233–260, June 2007.

40. Xia, Y., W. Chu, Q. Qi and L. Xun, "New insights into the QuikChangeTM process guide the use of Phusion DNA polymerase for site-directed mutagenesis", *Nucleic Acids Research*, Vol. 43, No. 2, pp. e12–e12, January 2015.

41. Kovtun, A., R. Heumann and M. Epple, "Calcium phosphate nanoparticles for the transfection of cells.", *Bio-medical materials and engineering*, Vol. 19, No. 2-3, pp. 241–7, 2009.

42. Dick, M. S., L. Sborgi, S. Rühl, S. Hiller and P. Broz, "ASC filament formation serves as a signal amplification mechanism for inflammasomes", *Nature Communications*, Vol. 7, No. May, p. 11929, June 2016.

43. Proell, M., M. Gerlic, P. D. Mace, J. C. Reed and S. J. Riedl, "The CARD plays a critical role in ASC foci formation and inflammasome signalling", *Biochemical Journal*, Vol. 449, No. 3, pp. 613–621, February 2013.

44. Moriya, M., S. Taniguchi, P. Wu, E. Liepinsh, G. Otting and J. Sagara, "Role of Charged and Hydrophobic Residues in the Oligomerization of the PYRIN Domain of ASC †", *Biochemistry*, Vol. 44, No. 2, pp. 575–583, January 2005.

45. Morrison, K. L. and G. A. Weiss, "Combinatorial alanine-scanning", *Current Opinion in Chemical Biology*, Vol. 5, No. 3, pp. 302–307, June 2001.

46. Hinterdorfer, P., H. J. Gruber, F. Kienberger, G. Kada, C. Riener, C. Borken and H. Schindler, "Surface attachment of ligands and receptors for molecular recognition force microscopy", *Colloids and Surfaces B: Biointerfaces*, Vol. 23, No. 2-3, pp. 115–123, February 2002.

47. Verbelen, C., D. Raze, F. Dewitte, C. Locht and Y. F. Dufrene, "Single-Molecule Force Spectroscopy of Mycobacterial Adhesin-Adhesin Interactions", *Journal of Bacteriology*, Vol. 189, No. 24, pp. 8801–8806, December 2007.

48. Afrin, R. and A. Ikai, "Subunit unbinding mechanics of dimeric wheat germ agglutinin (WGA) studied by atomic force microscopy", *FEBS Letters*, Vol. 588, No. 23, pp. 4472–4477, November 2014.

APPENDIX A: EMISSION SPECTRA OF ALL VARIANTS

Graphs corresponding to the emission spectra of all variants investigated in this thesis can be found here. On the graphs two sets of data can be observed. The first data set (that begins at Y axis, colored green) corresponds to the emission spectra recorded when the sample was excited at 488 nm. The second data set (that begins around 600 nm, colored red) corresponds to the emission spectra recorded when the sample was excited at 588 nm. Graphs represent the average of all three replicates. "bb" is negative control with EGFP only expression and "wt" is positive control with EGFP labeled wildtype PYD/CARD.

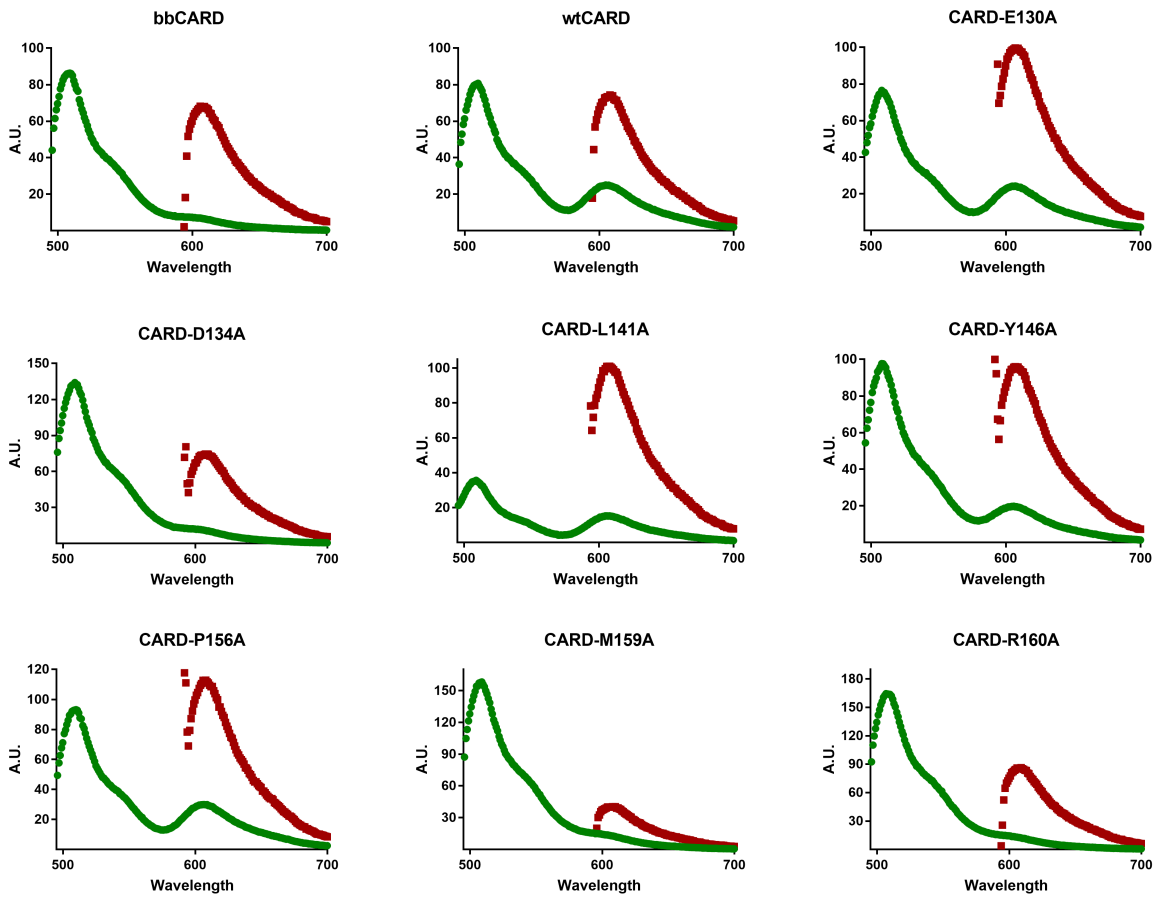

Figure A.1. Emission spectra of all CARD variants.

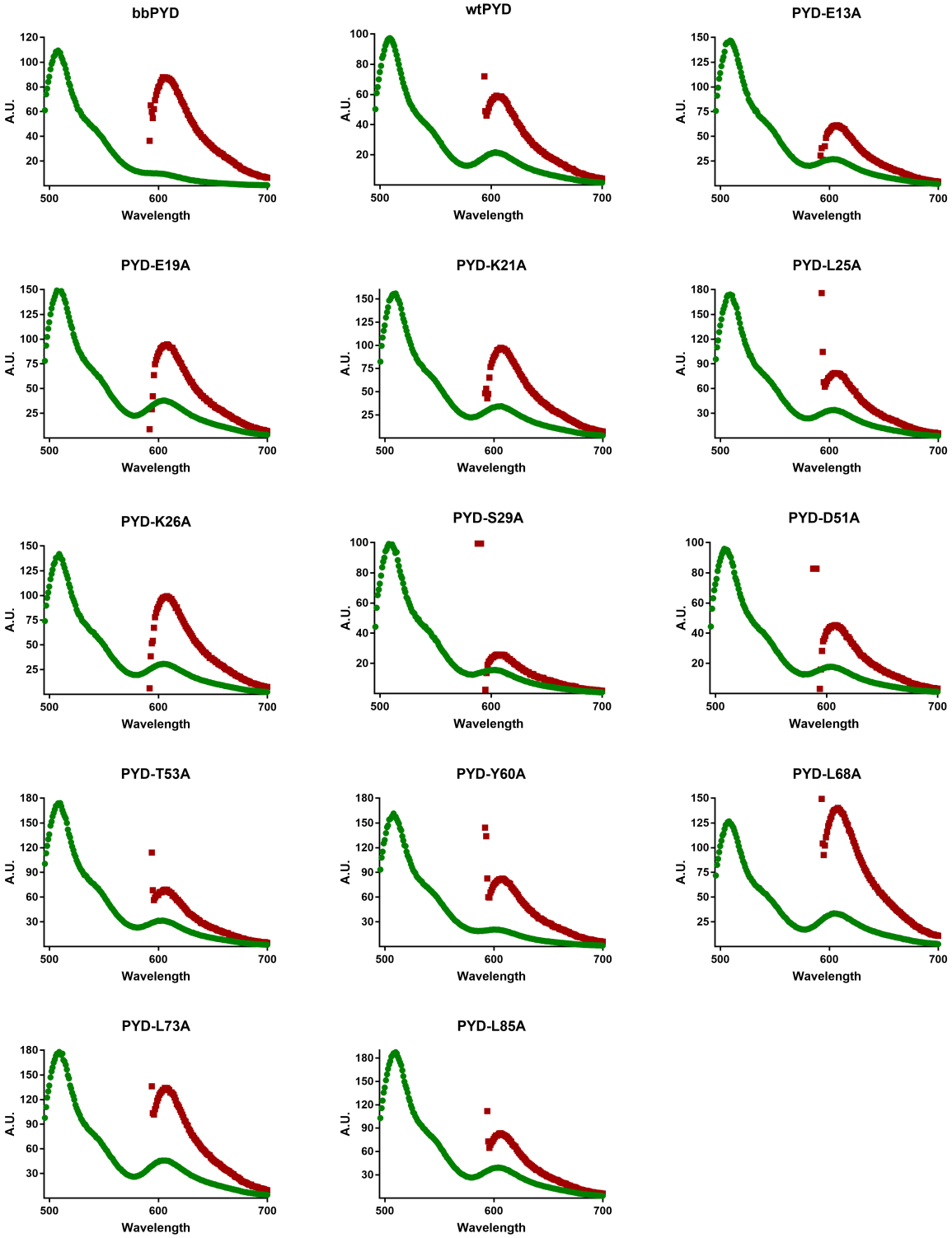

Figure A.2. Emission spectra of all PYD variants.

APPENDIX B: FLUORESCENCE MICROSCOPY IMAGES

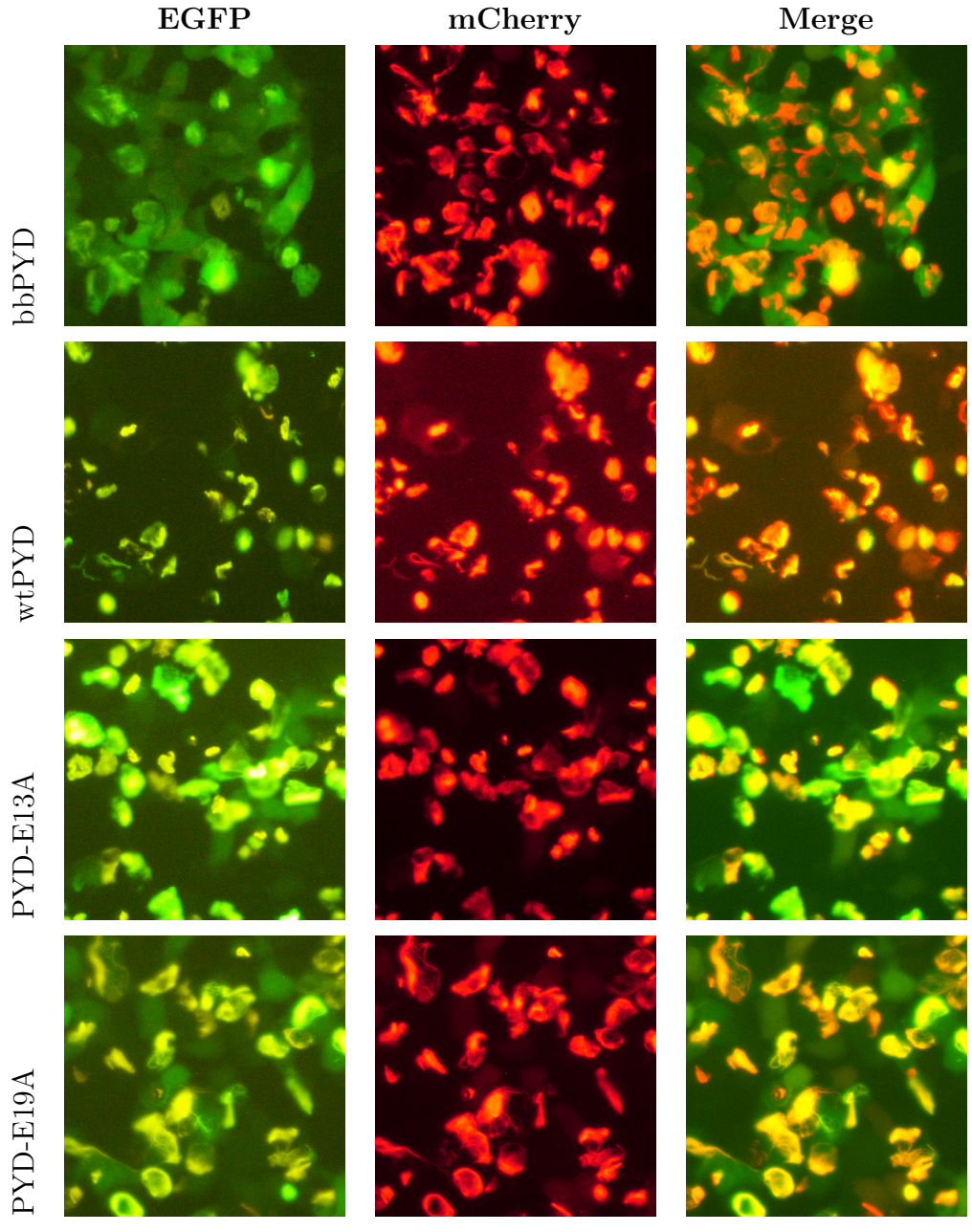

Figure B.1. Fluorescence images of all bbPYD (negative control), wtPYD (positive control) and E13A and E19A PYD variants.

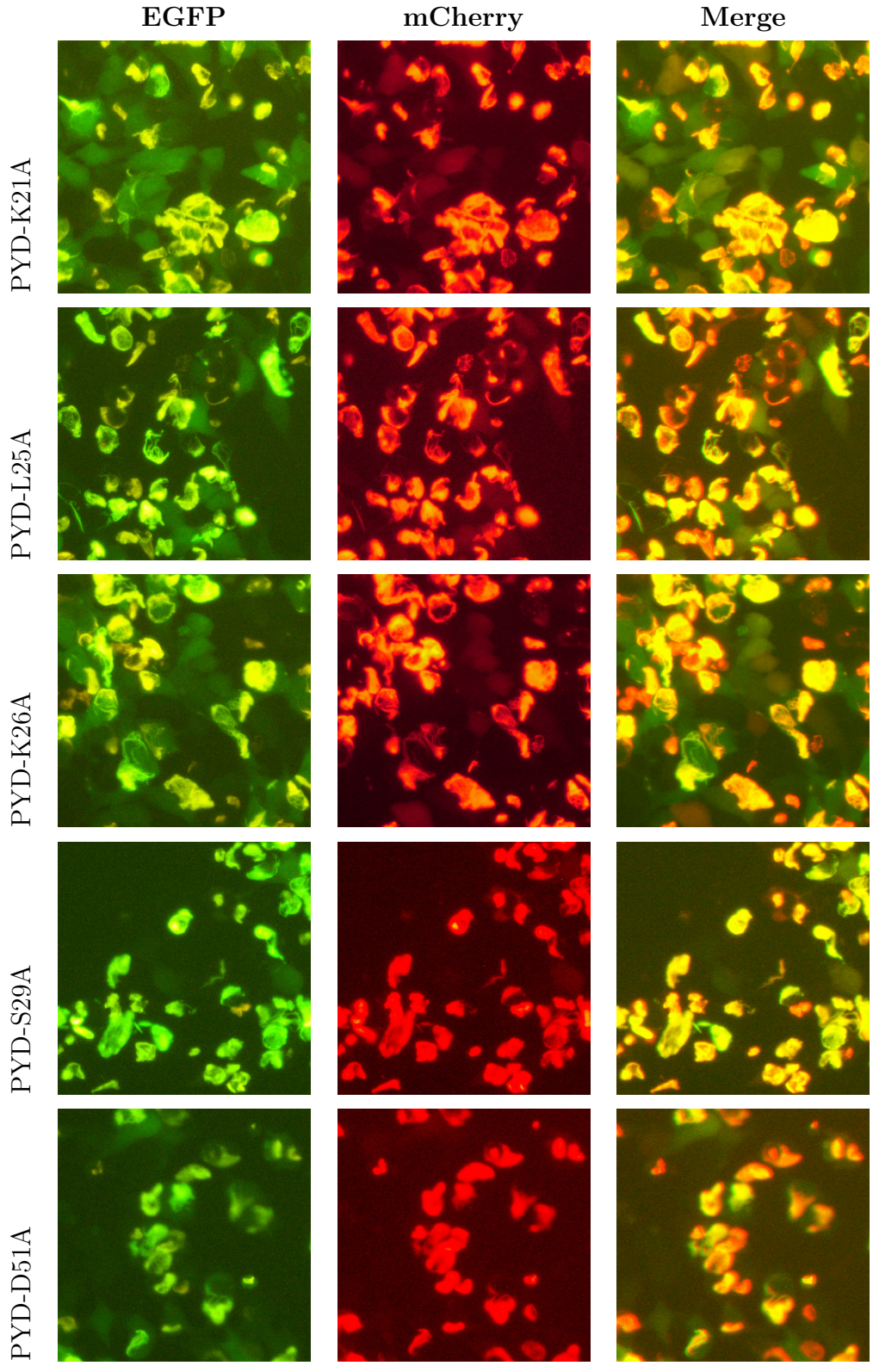

Figure B.2. Fluorescence images of K21A, L25A, K26A, S29A and D51A PYD variants.

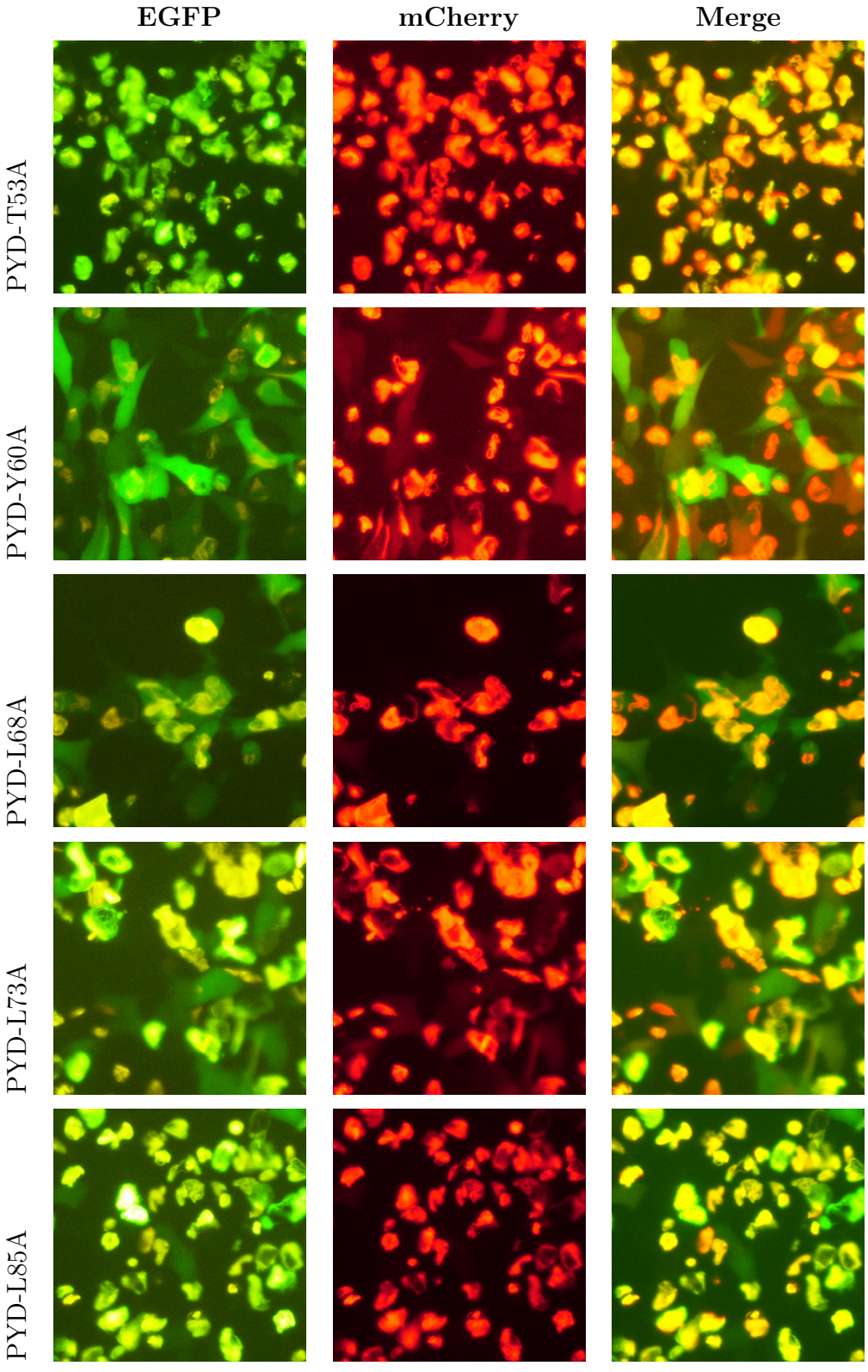

Figure B.3. Fluorescence images of T53A, Y60A, L68A, L73A and L85A PYD variants.

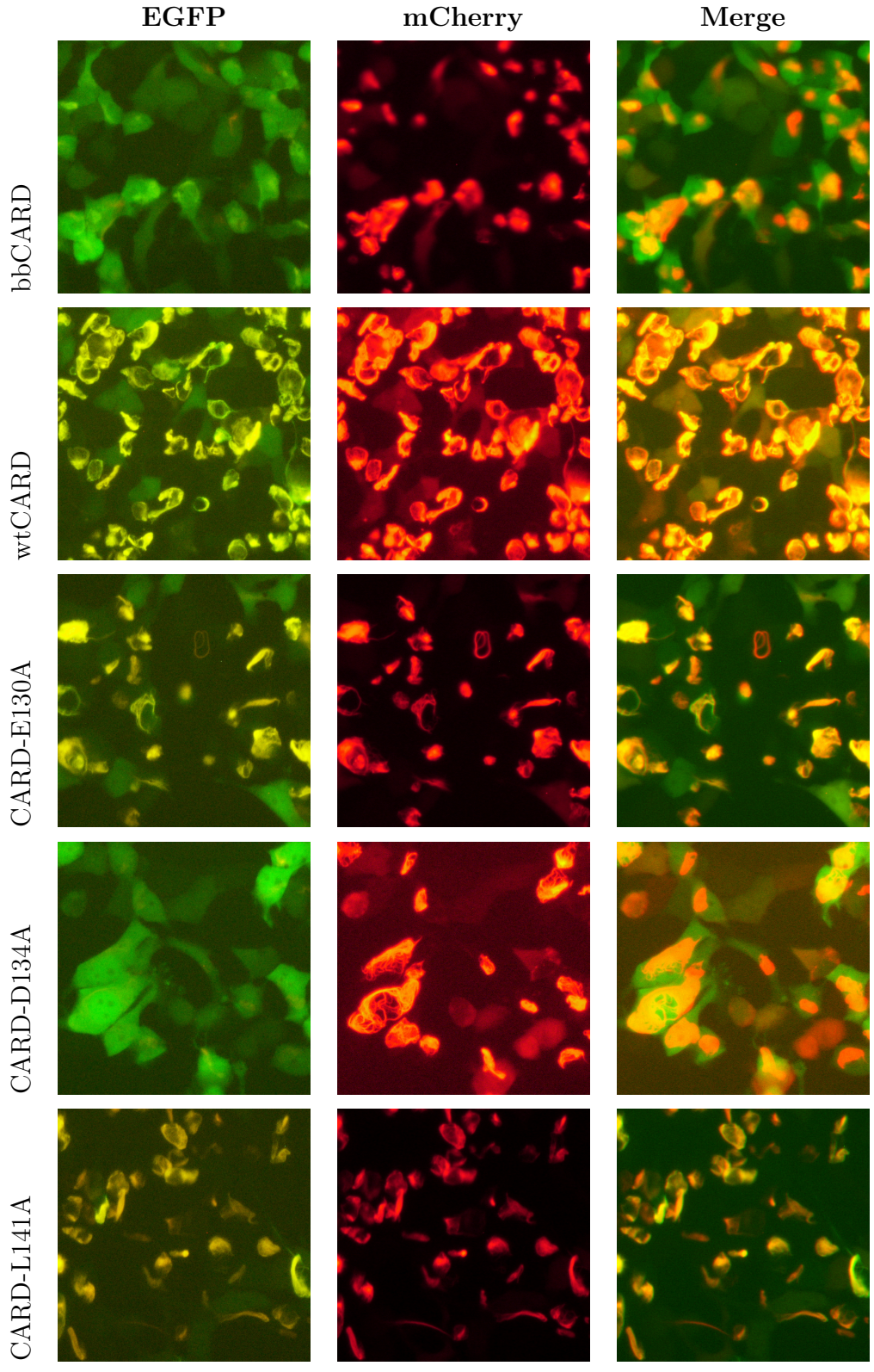

Figure B.4. Fluorescence images of bbCARD, wtCARD, and E130A, D134A and L141A CARD variants.

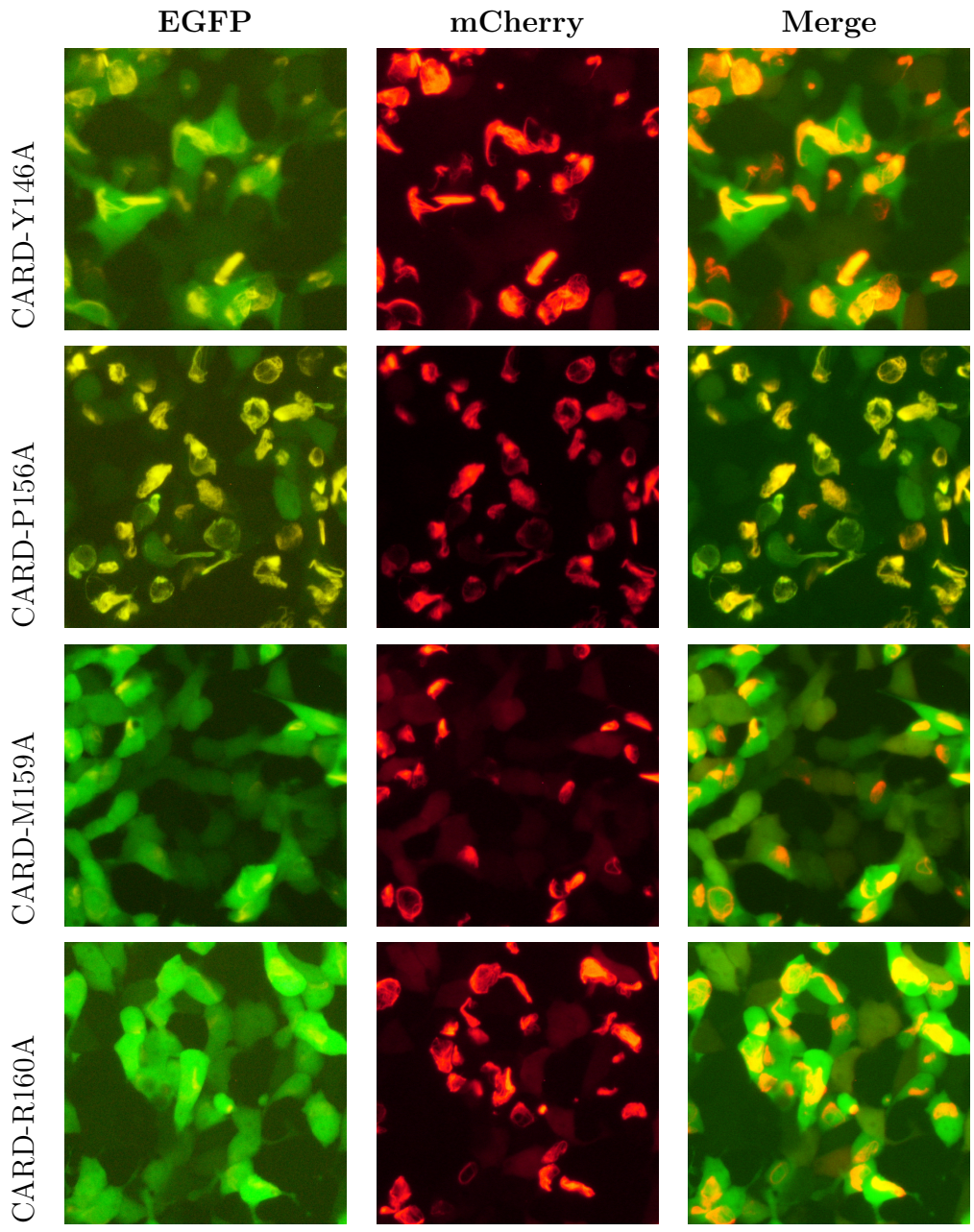

Figure B.5. Fluorescence images of Y146A, P156A, M159A and R160A CARD variants.

APPENDIX C: PLASMID MAPS

Maps of the plasmids used in this thesis. A stop codon is present after every ASC-PYD or ASC-CARD.

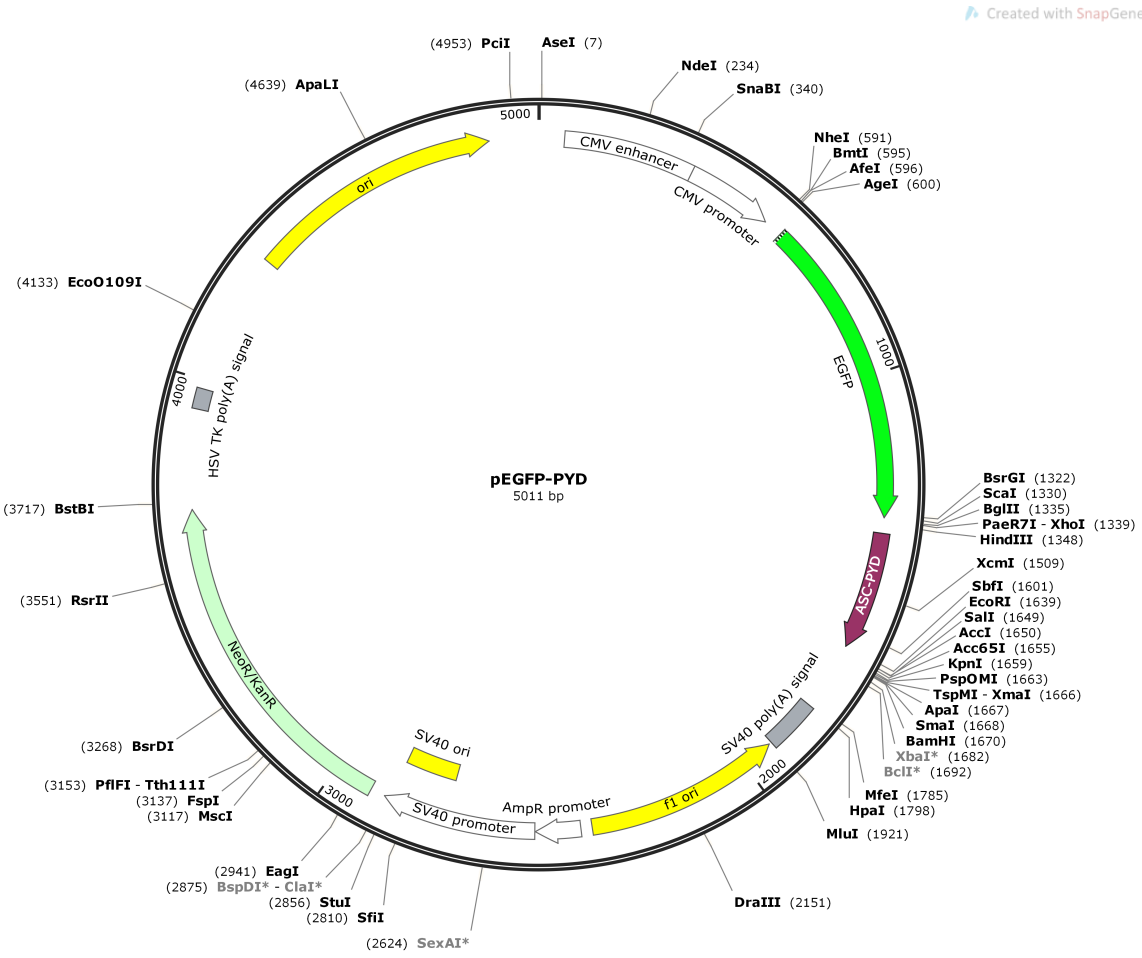

Figure C.1. Plasmid map of pEGFP-C3-PYD.

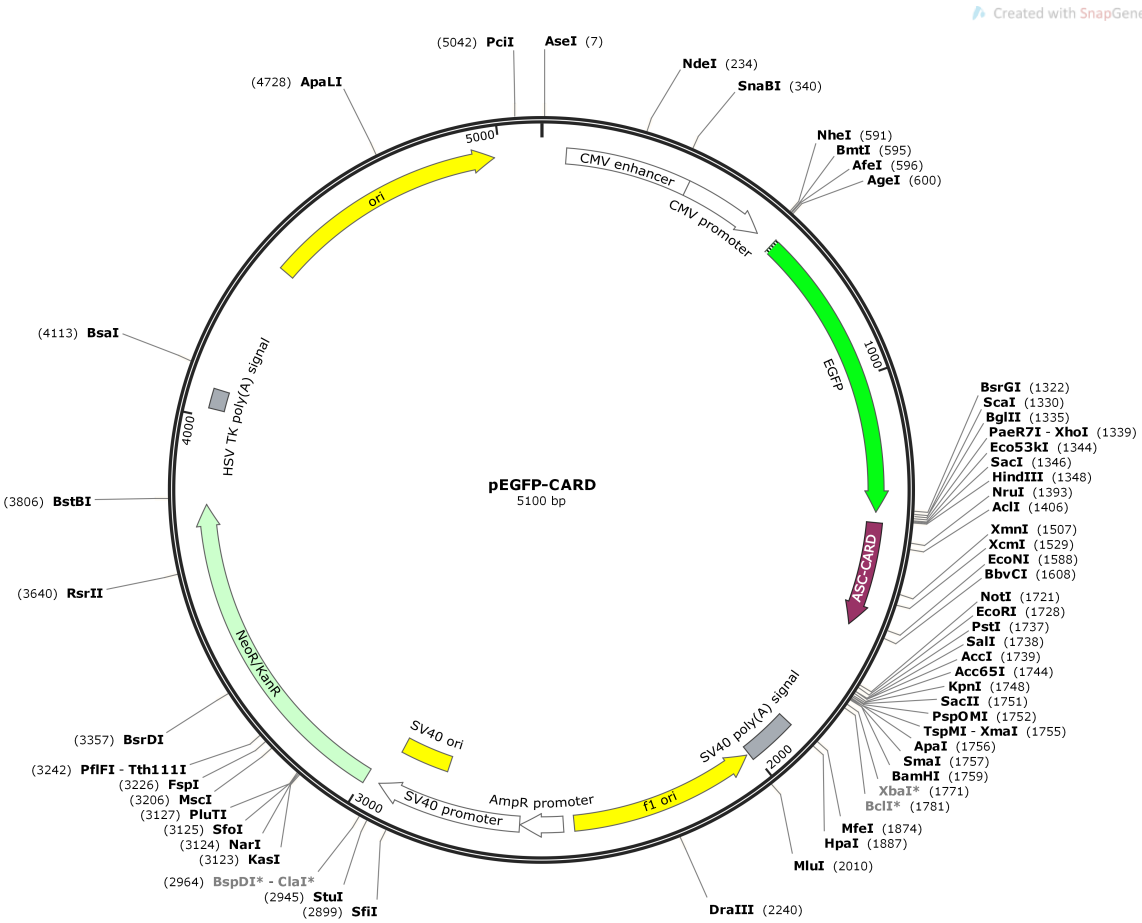

Figure C.2. Plasmid map of pEGFP-C3-CARD.

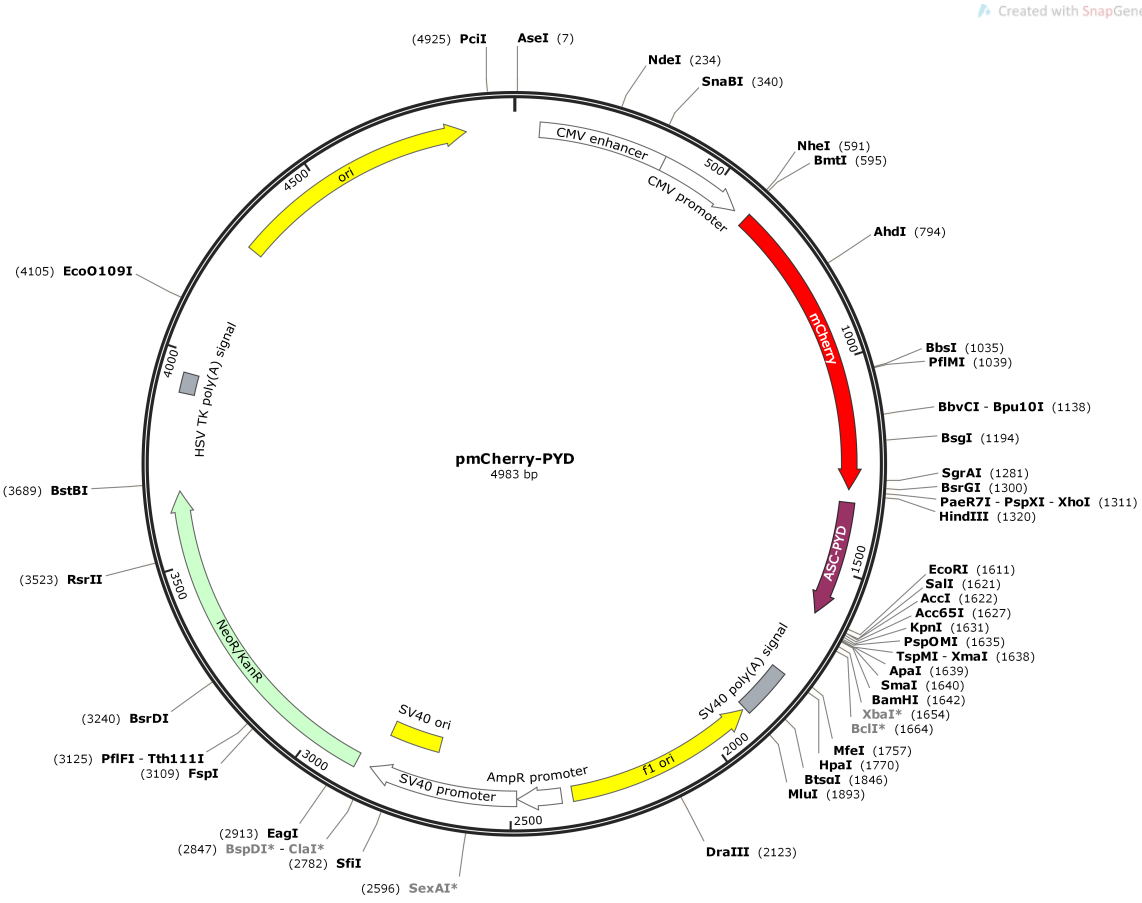

Figure C.3. Plasmid map of pmCherry-C3-PYD.

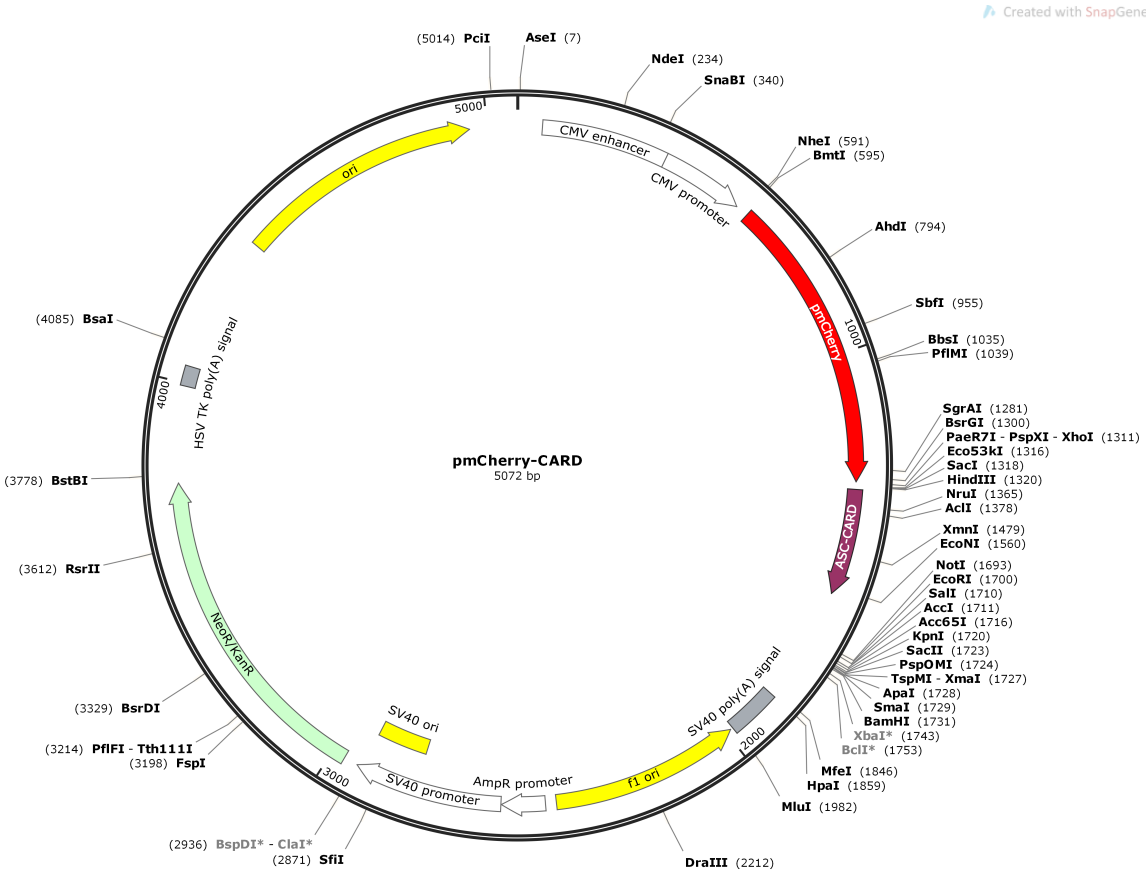

Figure C.4. Plasmid map of pmCherry-C3-CARD.

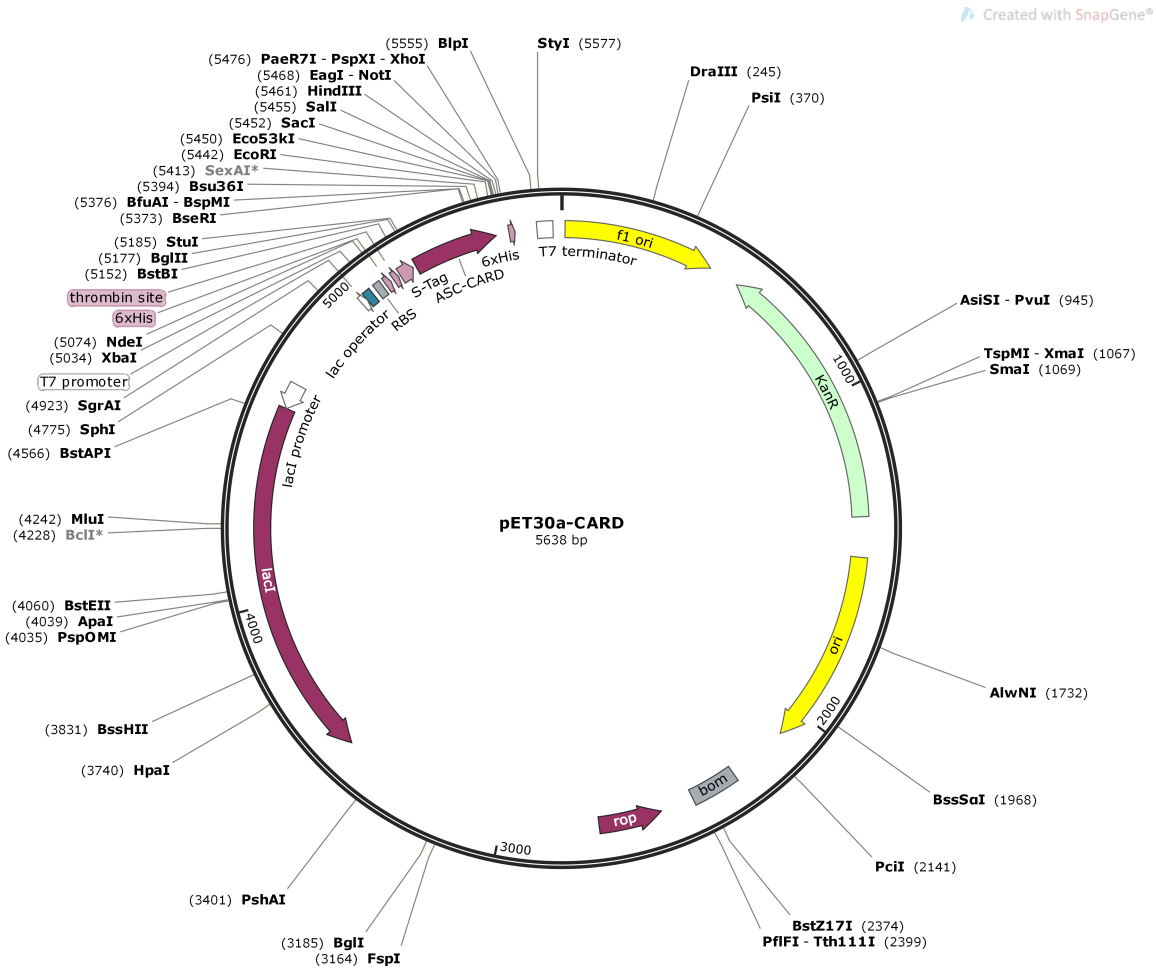

Figure C.5. Plasmid map of pET30a-CARD.